IN-PLANT APPLICATIONS OF A MICRO-TENSIOMETER WATER STRESS SENSOR

A Thesis

Presented to the Faculty of the Graduate School

of Cornell University

in Partial Fulfillment of the Requirements for the Degree of

Master of Science

by

Siyu Zhu

January 2017

ABSTRACT

Climate change has caused extreme weather conditions, and resulted in a large water stress in agriculture. Monitoring plant water stress is crucial for both the study of on plant drought responses and the improvement of the agricultural water use efficiency. However, current commercially available water stress sensors either lack of accuracy and resolution, or are too complicated to use. In this study, we developed a micro-tensiometer (μTM), which measures plant water stress in real time by monitoring the stem water potential (Ψ_{stem}) and the soil water potential (Ψ_{soil}) - the two most important plant water stress indicators - with high accuracy, high resolution, minimum sample destruction, and optimum local geometrical integration with the sample.

The μTM translates the water energy state into electronic signal by implementing traditional tensiometry in a microelectromechanical system (MEMS) with the nanoporous silicon membrane (PoSi) technique. This design significantly increased the measurement range from *>-0.1 MPa to >-10 MPa*. With the MEMS approach, the sensing area was reduced by two orders of magnitude (*from >10 cm^2 to 0.25 cm^2*).

In situ embedding strategies were developed for the μTM through testing on apple trees. In an in-plant experiment (GH2), the μTM (*~ -2.5 MPa*) showed up to *1.5 MPa* difference from the traditional Scholander pressure chamber *(~ -1.0 MPa*). This result led to the hypothesis that a vapor gap existed between the μTM and the tissue, and could result in a *7.77 MPa* error per degree Celsius of temperature difference (ΔT) between the sample and sensor at *25 ºC*. Different strategies were tried to reduce the vapor gap in the fourth experiment (GH4). The μTM with the best contact showed a linear correlation ($R^2 = 0.93$) with the Scholander. Other discoveries from the GH4, and their related hypotheses were discussed as well.

BIOGRAPHICAL SKETCH

Siyu began her undergraduate education in 2011 in Chemical Engineering at the University of Minnesota-Twin Cities. In Minnesota, Siyu studied under Dr. Wei-Shou Hu for his project on the mechanisms that inhibit the transfer of antibiotic resistance among bacteria cells. After receiving her degree in 2014, Siyu continued her research career in Cornell University under the supervision of Drs. Abraham Duncan Stroock (Chemical Engineering, Ithaca), Donald Koch (Chemical Engineering, Ithaca), and Lailiang Cheng (Horticulture, Ithaca), on the work presented in this thesis.

ACKNOWLEDGEMENTS

I would like to thank my advisor, Dr. Abraham Stroock, who has been an excellent mentor and helped me develop into a better researcher. I would also like to thank my committee members, Drs. Lailiang Cheng and Donald Koch, who have provided invaluable assistance with my research. I extend my gratitude to my collaborators, Drs Alan Lakso and Taryn Bauerle, who have given me valuable suggestions for my research.

I am also grateful to my research colleagues, Michael Santiago, Winston Black, Annika Kreye, Olivier Vincent, Hanwen Lu, I-Tzu Chen, and Erik Huber, who have worked with me every day and provided constant help throughout the course of my research. Finally, I would like to thank my family and friends for their unconditional support throughout my life.

LIST OF FIGURES

TABLE OF CONTENTS

I. INTRODUCTION

Climate change has resulted in global temperature rising, carbon dioxide concentration elevation, and increasing variability in precipitation.[1] Warmer temperature increased the water withdrawal from the earth through evapotranspiration, and reduced the water supply recharge at the same time.[2] Therefore, water supply sustainability is at risk (Figure I-1a). Water is important for agriculture. Irrigated agriculture occupies up to 80 to 90% of total water consumption of the U.S.[3] The extremes in temperature and the frequency in precipitation challenge the adaptability of crops to water stress, and have stimulated studies to quantify crop stress responses.[1,4]

To increase the water use efficiency (WUE), which measures the grain yield per unit amount of water supplied, studies have been done to understand the water stress responses of plants and to develop gene modified crops with drought tolerance.[5,6] Nevertheless, most of the plant drought response processes are understood incompletely, due in part to the lack of a tool that can monitor plant water stress accurately in real time, and with minimal destruction of the plant. Additionally, a recent study has shown that destructive sampling methods disturb the original water stress status inside the sample, and result in unreliable measurements.[7] The original model of water transport in plants as a soil-plant-atmosphere continuum (SPAC) has been proposed in 1948 by Van den Honert[8], but few direct measurements have been done to prove its reliability. Furthermore, scientists have been trying to understand the water stress distribution inside plants, more specifically, the radial distribution of water stress in plants. Without an appropriate tool, they have to combine the radial sap flow data in trees with laboratory measured hydraulic resistance of cut wood, to predict the water stress radial distribution.[9] Moreover, the mechanism of the plant regulation of stomata conductance, which is a crucial topic when it comes to plant drought responses, has been debated for decades. The

stomatal conductance regulates the rate of transpiration and photosynthesis, and therefore, directly affects the vegetative growth and reproduction of plants.[10,11] Without a reliable tool that can measure the soil and plant water stress *in situ* with high-resolution and fast response, after sixty years of debate, scientists still hold different opinions about whether the soil water stress induced chemical signaling, or the leaf water stress is the key parameter for stomatal regulation.[11] In summary, the lack of an in-situ tool with high-resolution, high-accuracy, fast response, and minimal plant destruction has been holding back the study on plant water stress for decades.

In this study, we developed a new water stress sensor called a micro-tensiometer, and tested its applications in living trees in a greenhouse. Preliminary testing showed a linear correlation between the sensor and the Scholander Pressure Chamber, the widely accepted water stress measuring equipment, on living apple trees. [12] The working mechanism of this sensor is based on the metastable vapor liquid equilibrium (MVLE). To develop this sensor, we coupled the idea of a traditional tensiometer with the MEMS technology, and built a micro-scale water stress sensor with a two orders of magnitude larger measurement range by adopting the nanoscale porous silicon membrane technique developed by the Stroock Group. With the ability to measure high resolution and high accuracy real time water stress, we aim to use this sensor to address un-answered plant physiological questions mentioned above, to screen plants with new drought tolerance genotypes, and to discover new phenomenon that cannot be observed in the past (Figure I-1b). In agriculture, the sensor can be integrated with a sophisticated water stress monitoring feedback loop computer system that controls when and how much to irrigate (Figure I-1c). Moreover, this tool can be applied to conduct further studies on metastable liquids and ecophysiological studies.

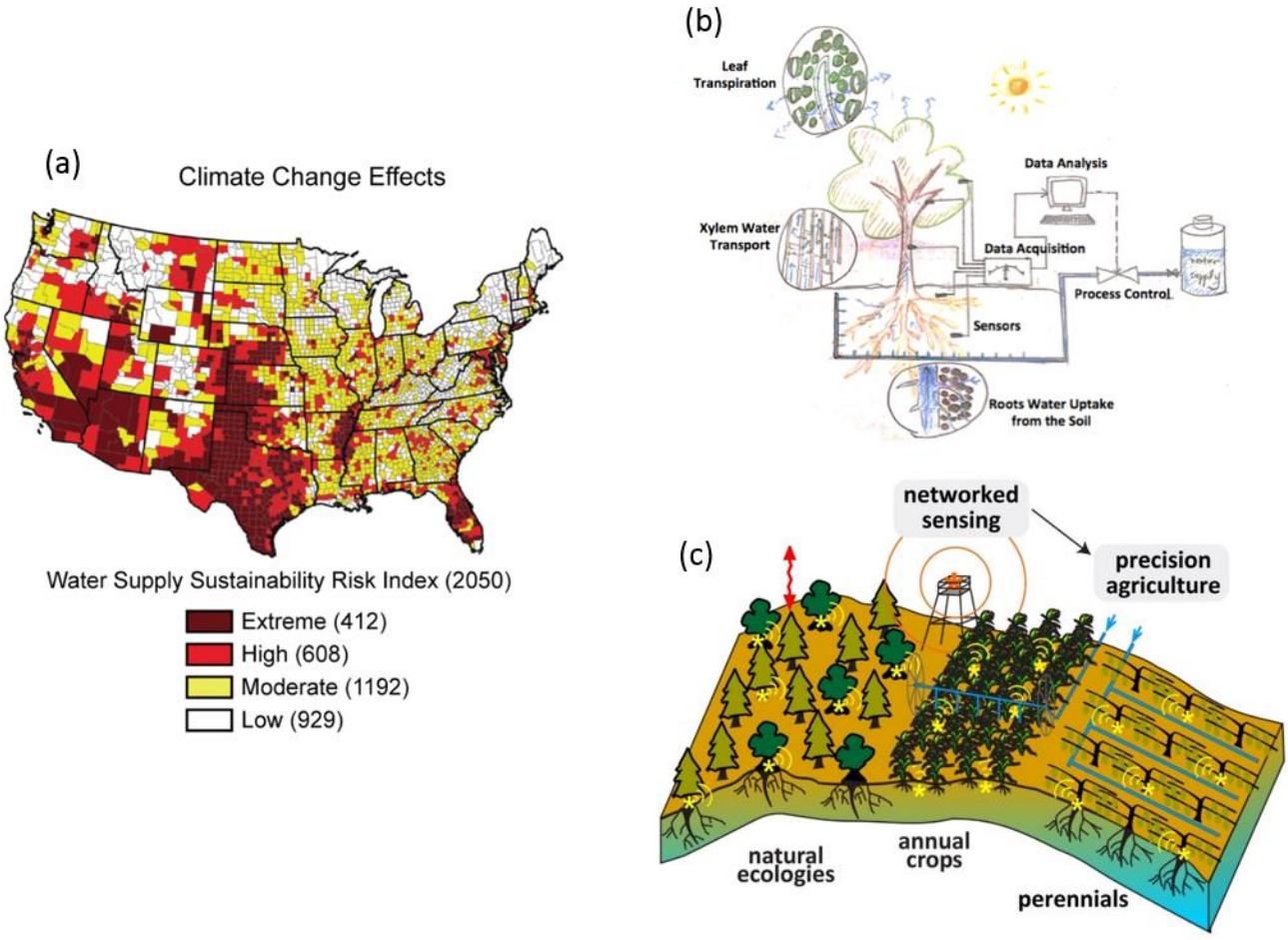

Figure I-1 Importance of Water on Agriculture

(a) Water Supply Sustainability is at Risk.[2]

(b) Expected Application of the Water Stress Sensor for Plant Drought Response Studies by monitoring the plant water stress at five different locations on one tree: soil, root, stem, branch and leaf.

(c) Expected Application of Water Stress Sensor for Irrigation Scheduling. The sensor can be integrated into an irrigation feedback loop. The correlation between the crop productivity and the water stress level could be studied as a reference for accurate water level control. The computer monitored precise irrigation could be realized.[61]

II. BACKGROUND

II.A. Metastable-Vapor-Liquid-Equilibrium (MVLE)

All liquids can sustain reduced pressure or even some tension due to their molecular interactions. This phenomenon is called cohesion. Water is more stable under tension than most liquids due to the strong hydrogen bonding between water molecules (Figure II-1a). At this condition, liquid water is in a superheated metastable phase. Cavitation occurs when the tension reaches the stability limit of liquid water, and is able to create a vapor bubble nucleation. After cavitation, the liquid and vapor phase of water will reach a saturated liquid-vapor phase equilibrium.[13]

There are a variety of methods to stretch liquid water and make it metastable.[14] In tensiometry, tension occurs due to metastable-vapor-liquid-equilibrium (MVLE), where a volume of liquid water is in metastable equilibrium with the outside sub-saturated vapor through a thin layer of nanoscale porous silicon.[13,15] As Figure II-1b&c illustrate, when changing the vapor phase from saturated to sub-saturated state, water evaporates from the air-liquid interface inside the pores and forms a curved meniscus. The capillary pressure of the meniscus balances the pressure difference between the liquid and the outside environment. Based on Young-Laplace Equation (1), the capillary force is proportional to the surface tension ($\sigma, \frac{mN}{m}$) and the cosine of the contact angle (θ) between the silicon and liquid water surface, and is inversely proportional to the radius of the pore size. By using nanoscale pores, we are able to generate a large tension inside the bulk liquid ($\geq$ *-20 MPa*).[13]

$$\Delta P_{cap} = \frac{2\sigma\, cos\theta}{r_p} \qquad (1)$$

The liquid pressure in the metastable state can be derived by assuming isothermal conditions and at the condition for phase equilibrium: the chemical potential of liquid water ($\mu_{w,liq}$) and vapor ($\mu_{w,vap}$) are the same.

$$\mu_{w,vap} - {\mu_w}^0 = \mu_{w,liq} - {\mu_w}^0 \quad (2)$$

Where ${\mu_w}^0$ is the chemical potential of pure liquid water and vapor at standard temperature (T) and pressure (P_0).

If we assume the vapor is ideal, we can use ideal gas law to generate the sub-saturated chemical potential of water vapor:

$$\mu_{w,vap} - {\mu_w}^0 = \int_{P_{sat}}^{P_{vap}} v_{w,vap} dP = \int_{P_{sat}}^{P_{vap}} \frac{RT}{P} dP = RT ln \frac{P_{vap}}{P_{sat}} = RT\, ln a_{w,vap} \quad (3)$$

Where P_{sat} is the saturated vapor pressure at standard temperature and pressure; P_{vap} is the sub-saturated vapor pressure; $v_{w,vap}$is the molar volume of the water vapor, which we replaced by ideal gas law in this equation (3); *R = 8.314 J/K-mol* is the ideal gas constant; and $a_{w,vap} = \frac{P_{vap}}{P_{sat}}$ is the activitiy of the water vapor.

For liquid chemical potential, if we assume the density of water does not change, we can approximate the chemical potential of the metastable liquid water:

$$\mu_{w,liq} - {\mu_w}^0 = \int_{P_0}^{P_l} v_w dP \cong v_w (P_l - P_0) \quad (4)$$

Where P_l is the hydrostatic pressure in liquid water; $v_w = 18.02 \times 10^{-6}\, m^3/mol$ is the molar volume of liquid water, and is assumed to have minimal variations in the µTM working temperature range.

Combining equation (3) and (4), the sub-saturated liquid pressure is expressed below:

$$P_l - P_0 = \frac{RT}{v_w} ln a_{w,vap} = -\Delta P_{cap} \quad (5)$$

In Eq. (5), we indicate that the pressure difference required by phase equilibrium must be equal to that due to capillarity.

Once the tension is large enough to reach $\Delta P_{cap} = \Delta P_{cap,max}$, the contact angle reaches the receding contact angle (θ_r) between silicon and water. Once the tension is larger than the maximum capillary pressure, the meniscus will no longer hold, and the air-liquid interface will recede into the bulk liquid. This mechanism of cavitation is called air-invasion.[16]

The application of MVLE in the micro-tensiometer will be discussed in Section II.D in detail.

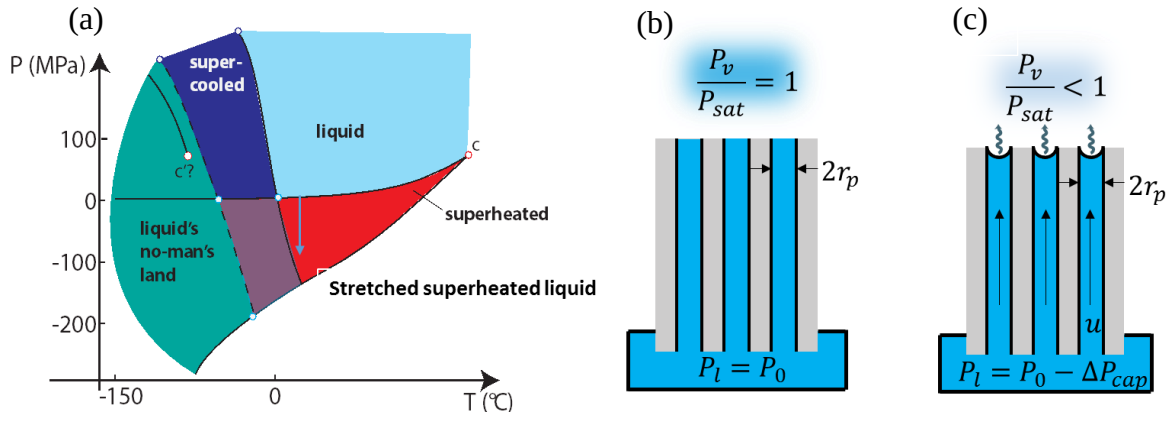

Figure II-1 Water under Metastable State

(a) The schematic representation of the P-T phase diagram of water. Water can be stretched from pure saturated liquid water to metastable liquid water by isothermally pulling on the water along the blue arrow. The liquid water can stay in a metastable state at negative pressure due to the strong attractive interactions between liquid water molecules.
(b) A schematic diagram of MVLE in true equilibrium. Liquid water is connected to the outside vapor through a porous membrane with an average pore diameter of r_p. At saturated state, the hydrostatic pressure of liquid water equals atmospheric pressure, and the vapor is in saturated vapor state. The liquid and vapor are at equilibrium.
(c) A schematic diagram of MVLE in metastable equilibrium. The same vapor-membrane-liquid system under sub-saturated state. The vapor pressure is lower than the saturated vapor pressure. The water evaporates from liquid state to vapor state until a stable curved meniscus forms. The surface tension of the meniscus pulls liquid water inside the reservoir and caused a lowered hydrostatic pressure that equals the capillary pressure.

II.B. Soil-Plant-Atmosphere Continuum (SPAC)

Water is important for plants and soils to maintain hydration, and as a reagent in the photosynthetic reaction and as a nutrient transporter. The soil-plant-atmosphere continuum describes the water movement from the soil, through the plant, to the atmosphere.[17] This movement is driven by the gradient in the energy state of water from high to low. The soil is the source of water for the continuum, and has higher chemical potential. The atmosphere is the sink of the water flow, and has the lower chemical potential. Water evaporates from the leaves to the atmosphere through transpiration. The transpiration creates a negative pressure on the water inside the plant and pulls water from the soil to the atmosphere (Figure II-2). The SPAC can be treated as a MVLE system with soil as a large reservoir of liquid water, plant as the porous membrane, and the atmosphere as the sub-saturated vapor.

II.B.1. Energy State of Water

Water potential (Ψ) is commonly used in plant science to describe the energy state of water. It is defined as the chemical potential of water (μ_w) relative to pure water ($\mu_w{}^0$) divided by the molar volume of pure water (v_w) at that temperature and pressure:[16]

$$\Psi = \frac{\mu_w - \mu_w{}^0}{v_w} \quad (6)$$

Therefore, water potential is the chemical potential of water in pressure units. It represents the free energy of water per unit volume relative to pure water. Water movement in SPAC happens spontaneously along a gradient in water potential.

Based on Eqn. (3), the vapor water potential can be expressed as

$$\Psi_v = \frac{RT}{v_w} ln a_{w,vap} \quad (7)$$

Similarly, the liquid water potential can be expressed as

$$\Psi_l = P_l - P_0 \quad (8)$$

At equilibrium (true or metastable), the liquid water potential equals the vapor water potential. This liquid-vapor relationship is the well-known Kelvin equation, as shown below:

$$\Psi_l = \frac{RT}{v_w} ln a_{w,vap} \quad (9)$$

Water potential has been an important indicator for both plant and soil drought status.[18] For example, soil water potential has been used to schedule irrigation for agriculture.[19] Plant scientists divided water potential into four terms based on its four major contributors. The four major components are osmotic potential (Ψ_s), pressure potential (Ψ_p), matric potential (Ψ_m), and gravity potential (Ψ_g):

$$\Psi = \Psi_s + \Psi_p + \Psi_m + \Psi_g \quad (10)$$

The osmotic potential is the reduction of the water potential due to the dissolved solutes, such as sugars and mineral nutrients. Pressure potential represents the hydrostatic pressure of water. It can be positive, as turgor pressure in cells, or negative, as water under tension in xylem (see Section II.B.3 for details). Matric potential represents the capillary and adsorption effect from solid phases, such as soil particles and mesophyll cells in leaves (Figure II-2 b&d). Water adsorbs onto the wettable surface of the solid particles, and forms menisci in the small pores between them through capillarity. These menisci generate negative pressure due to surface tension, as explained in Section II.A Eqn. (1). The smaller the radius of curvature of the meniscus, the more negative the matric potential will be. The plant tissue can also be treated as a polymer gel. Based on Flory-Huggins theory, the matric potential of a wet tissue can be treated approximately as the osmotic potential of a solid polymer solution.[20] Hence, the matric potential of a sample depends on the inherent surface characteristics of a sample, its moisture fraction, particle size, and particle distribution. We use water content to describe the moisture fraction of a

material. It is defined as the volumetric fraction of water in a wet matrix, $\Theta = \frac{V_w}{V_w+V_m}$, where V_w is the volume of water in the matrix, and V_m is the volume of the dry matrix. Every material has a typical water retention curve *Θ (Ψ, T)*, which shows the relationship between the water potential and the water content. Some hygrometers measure water potential by measuring the water content of a material (e.g. concrete) with a calibrated water retention curve. The last potential component is gravity potential, $\Psi_g = -\rho g h$, where $\rho = 997\ kg/m^3$ is liquid water density; $g = 9.81\ m/s^2$ is the gravitational constant; h is the height relative to the reference state. Gravity potential pulls water towards soil through gravitational force, and reduces plant water potential to a more negative value. Its value depends on the reference level, and plays a key role in soil drainage.

II.B.2. Water Movement Through SPAC

Soil is the water source for the SPAC. Different soil types have different water holding capacity. This capacity depends on the matric characteristics discussed in the previous section. For example, clay has higher water holding capacity than sand because clay has smaller particles (2 μm < 1 mm). Smaller particle size means larger surface area for water adsorption per unit volume, and smaller pores between particles for meniscus formation. The small pores trap water through capillarity and prevents water from drainage due to gravity. As shown in Figure II-2-d, at high water potential, both clay and sand have high water content. However, for a water potential decrease from *-10^{-1}* to *-1 hPa*, sand has a sharp reduction in water content, while clay has moderate decrease in water content. Therefore, clay has the highest water holding capacity than the other two soil types, and sand has the lowest water holding capacity. Water moves from more saturated soil to less saturated soil, for example, around the roots, down the gradient of water potential.[18]

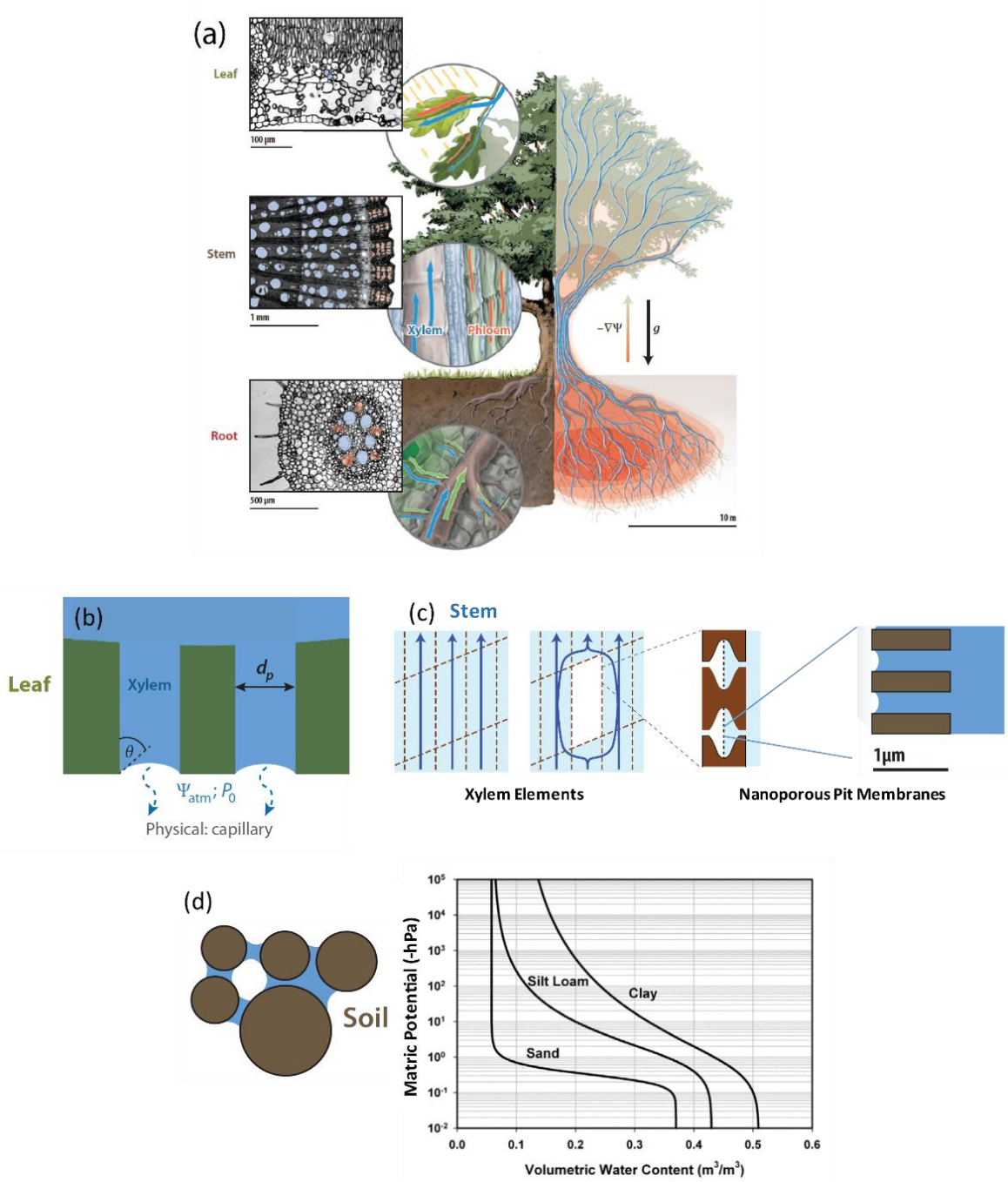

Figure II-2 Water Movement through a Plant.

(a) A schematic diagram of transpiration. Water potential gradient in the direction from soil to the atmosphere drives the transpiration.
(b) A diagram of the site of evaporation in leaf. Water evaporates from the water covered sites in the leaves to the atmosphere through stomata.
(c) A diagram of water transport in stem xylem elements. Water can bypass the cavitated elements through pit membranes. The nano-scale pores on porous pit membrane prevented air invasion from cavitated xylem elements to functioning xylem elements through capillarity.
(d) A diagram of water adsorption onto soil particles. The plot on the right shows the water retention curve of difference soil types (reproduced from Buckingham 1907[62]). (Figures Modified from Stroock 2014[24])

At the site of the root-soil interface, the ability of roots to absorb water depends on the water potential difference across the root cell membrane. This driving force is mainly contributed by pressure potential and osmotic potential.[21] As soil dries out, the water uptake from the soil to the root will cease, due to the large hydraulic resistance between the soil and the root when the soil and root water potential are lowered to a critical value.[16]

The water movement mechanism in stems from root to leaf was first proposed as Cohesion-Adhesion theory by Dixon and Joly in 1894.[22] Due to the strong molecular interaction between liquid water molecules, water is able to remain in liquid phase under negative pressure. Due to the strong intermolecular interactions between the water molecules and the hydrophilic surface of the xylem wall, which is called adhesion, water can be pulled from the root to the leaf through capillarity under negative pressure. This negative pressure is created at the evaporation site from leaves, through liquid-vapor equilibrium and capillarity as described by the Kelvin-Laplace equation (Eqn. (5) in Section II.B.1). Water transport in the stem happens mainly through the xylem (Figure II-2-c). Xylem conduits are composed of small xylem elements interconnected with each other through pit membranes. These xylem elements are elongated, hollow, dead cells with thick highly lignified secondary walls. They form longitudinal stacks to effectively transport water.[16] Compared to living cells with their intact plasma membrane, xylem allows water to be transported from root to leaf with minimum hydraulic resistance. The walls of xylem conduits prevent them from collapsing when the water in the xylem is experiencing large tension (~ *-10 MPa*). The pit membranes originated from primary walls of the dead cells. They are nano-scale to micro-scale porous membranes composed of cellulose microfibriller matrix. Cavitation happens when the tension is larger than the stability limit of the water in a xylem element[23] , or when there is air-invasion from a neighboring non-functioning gas-filled xylem

elements.[24] If one xylem element cavitates due to the negative pressure or air-seeding, the air-water interface will be trapped inside the pores of the pit membranes. This capillary force prevents air from entering the neighboring functioning xylem elements. Water can still bypass the cavitated xylem elements by going through the surrounding non-cavitated xylem elements through the pit membrane (Figure II-2-b). Although pit membranes increase the resistance of water transport in xylem, they also protect against the spreading of the cavitated (embolized) zone from spreading.[18]

The evaporation sites in the leaves could be the mesophyll cell walls, the leaf xylem conduits, or the tissue around the stomata.[25] We could assume these wetted surfaces are hydrophilic porous matrices. [24] The menisci formed in these wettable porous membranes create a large tension and pull water from the root to the leaf.

Evaporation from a leaf's interior is significantly inhibited by the cuticle.[26] Water can mostly diffuse to the atmosphere through stomata. Stomata are pores on the epidermis of leaves, and regulate the gas exchange between inside the plant and the atmosphere. Stomata open during the day in response to sunlight to start the photosynthesis. Photosynthesis produces the carbohydrates for the growth and reproduction of the plants. Stomata opening allows carbon dioxide, the carbon source of photosynthesis, to enter the plant, the oxygen produced by photosynthesis to be released into the environment, and the water vapor to diffuse out of plants. The evaporation is driven by the vapor pressure deficit ($VPD = \frac{100-RH\%}{P_{sat}}$). [27] For one carbon dioxide to enter stomata, approximately 400 water molecules are lost to the atmosphere.[18] This gas exchange ratio shows that plants need to transpire a lot of water to sustain the normal operation of photosynthesis. Under severe water stress, plants close their stomata through

physiological regulation, and slow down the rate of transpiration. The water stress affects the rate of photosynthesis at the same time.[28]

II.B.3. Soil-Root-Leaf Water Relations

The diurnal variations of soil-plant water relations are shown in Figure II-3. Figure II-3-a is a hypothetical sketch based on the theory. Figure II-3-b is an unusual set of experimental data that coincided the theoretical hypothesis; reproduction of results such as these has been hindered by the lack of appropriate tools. The rate of transpiration is not only related to plant and soil responses, but is also influenced by VPD and solar intensity. The solar energy heats up the leaves and drives their water evaporation. VPD drives the diffusion of water vapor from inside the leaves to the outside environment, as explained in the previous section. During the day, the solar

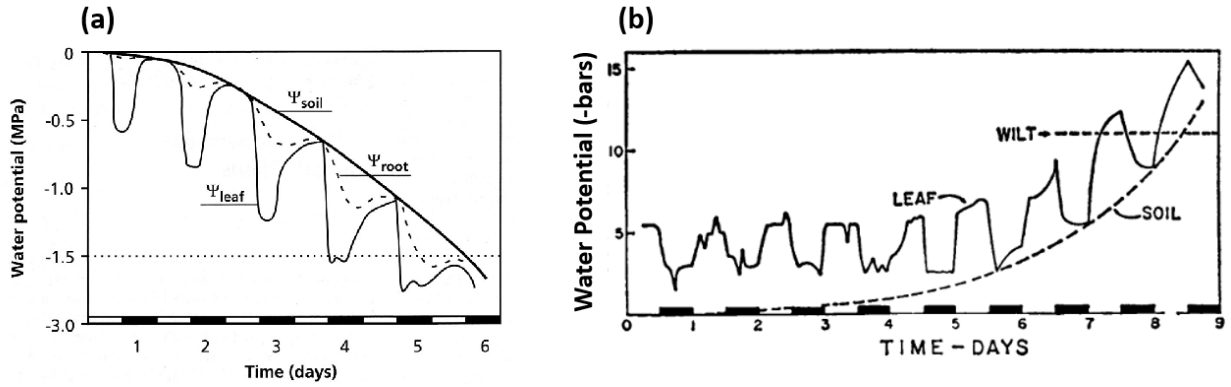

Figure II-3 Soil-Root-Leaf Water Relations

(a) Hypothetical Sketch for the Diurnal Variations of Soil-Plant Water Relations.[16]*Solid bars indicate twelve-hour dark periods. During the day, the leaf water potential decreases to a more negative value than the root water potential due to transpiration. The dashed line at -1.5 MPa represents the wilting point of the plant. As the soil gets drier, the soil water potential decreases (to more negative values), the predawn plant water potential (leaf and root) always returns to the soil water potential, until the wilting point is reached.*

(b) Experimental Results for the Diurnal Variations of Soil-Plant Water Relations.[63] *(Note that the y-axis is in negative bars) The diurnal variations of a pepper leaf water potential was compared with the soil water potential around the root. The leaf water potential was obtained by measuring the water content of a leaf through β-ray transmission. The leaf water potential can be found through a known water retention curve. The soil water potential was measured through a traditional tensiometer. At the beginning, the predawn leaf water potential does not return to the soil water potential. As the soil gets drier, the predawn leaf water potential reached soil water potential until the wilting point.*

intensity regulates the opening of stomata to start the gas exchange of water (H_2O) and carbon dioxide (CO_2) between the plant and the atmosphere. Water evaporation from the leaf generates a gradient of water potential from the root (less negative water potential) to the leaf (more negative water potential) in the plant (Figure II-3-a). The maximum water potential measured during the day is the midday water potential (Ψ_{midday}). At night, no sun light is sensed by the leaves, so the stomata are closed, which means the transpiration and photosynthesis are stopped. The plant water potential progressively relax (less negative) to the same level as the soil water potential.[16] The least negative diurnal leaf water potential is called the predawn water potential ($\Psi_{predawn}$).

II.B.4. Stem Water Potential indicates Plant Stress Level.

Both leaf water potential and stem water potential are good indicators for plant water stress level. The predawn leaf water potential indicates the effective soil water potential, which integrates the complete root-soil system. However, during the day, the leaf water potential is easily affected by the variations of the transpiration rate, and shows large variations in measurements. Furthermore, single leaf water potential measurements cannot represent the stress level of the entire tree, because different leaves experience different micro-environments. This micro-environment is affected by the shading from other leaves, wind speed around the leaves, and physiological effects from nearby organs. Different from the leaf water potential, stem water potential integrates the effects from all the leaves and organs on a tree, and is the best plant water stress indicator, as recommended by Naor 2000.[29] The stem water potential is closely correlated with the vegetative growth and the reproduction of plants (Figure II-4). The vegetative growth rate and the fruit growth rate decrease with the decreasing stem water potential (more negative).

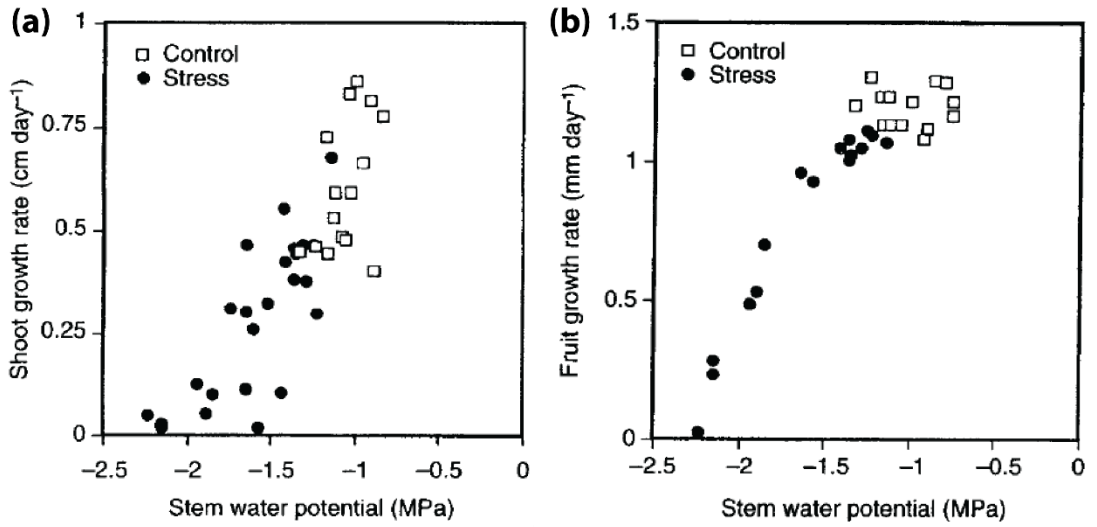

Figure II-4 Stem Water Potential is Important for the Reproduction and Vegetative Growth of Plants

(a) The vegetative growth of an apple shoot under stress conditions and controlled well-watered conditions is compared in this plot. As stem water potential becomes more negative, the shoot growth rate is reduced. (b) The fruit growth rate of apple under stress and well-watered conditions (control) are compared. Similar to the shoot growth, when stressed, the fruit growth rate decreases with increasing stem water potential.

Therefore, monitoring the stem water potential is crucial for both plant physiology studies and for agriculture.

II.C. Commercially Available Water Potential Sensors

Water potential in plants and soils has a general range from *0* to *-3 MPa*, with a high requirement of near-saturation accuracy because most irrigated soils have a water potential range of *0* to *- 0.15 MPa*.[30] The stem and leaf water potential are typically *> -10 MPa*.[12,31] There are four major types of commercially available hydrometers: the leaf Scholander pressure chamber, the thermocouple psychrometer, the electro-magnetic based sensors, and the tensiometer. Their accuracy, measurement range, response time, form factor, and ease of operation have been compared in Table II-1.[24]

The leaf Scholander pressure chamber is the most widely used *ex situ* hydrometer. It measures the leaf water potential by cutting the leaf off from the tree, sealing the entire leaf inside the pressure chamber with the cut end of the stem protruding out of the chamber, and slowly pressurizing the leaf with gas until water starts to come out from the cut end. The gas pressure inside the chamber at this point is equal and opposite to the leaf water potential. The water potential measured through this method are mainly pressure potential and osmotic potential of the leaf.[12] This method is easy to operate, but requires labor to do measurements manually. Random error happens due to individual operation and subjective end point judgement. In addition, the high pressure gas used by the pressure chamber is hazardous. The thick-wall of pressure chamber is usually cumbersome.

The thermocouple psychrometer is the most accurate *in situ* plant hygrometer. It uses the dry bulb and wet bulb temperature difference to measure the relative vapor pressure the gas in

Table II-1 Commercially Available Hygrometers

	Method	Range Ψ_w *(MPa)*	Accuracy $\pm\Psi_w$*(MPa)*	Response Time	Form Factor	Limitations
in situ	Psychrometry[32]	*-0.01 to -10.00*	*±0.10*	*1 min*	*< 5 cm²*	Temperature sensitive; expertise required
	Electro-magnetic[33]	*-0.01 to -0.50*	*±0.13*	*10 – 60 min*	*> 30 cm²*	Low accuracy; long response time
	Tensiometry[34]	*+0.100 to -0.085*	*±5.0x10⁻⁴*	*30 min*	*> 10 cm²*	Limited measurement range
ex situ	Scholander Pressure Chamber[35]	*0 to -4*				Limited measurement range; Destructive Sampling
	Chilled Mirror Hygrometer[36]	*0 to -5 (high accuracy) -5 to -480 (low accuracy)*	*0 to -5 MPa: ± 0.05 -5 to -480 MPa: ± 1%*	*< 5 min*		Destructive Sampling

equilibrium with the sample. Different from the pressure chamber, psychrometers can operate automatically. Nevertheless, the operation of most psychrometers is an intrinsic non-equilibrium process. The thermocouple junction is cooled to allow vapor condensate on it for web bulb dew point temperature measurement. The vapor condensation process is never in equilibrium due to the varying tissue temperature.[32] This temperature gradient from the tissue to the condensation point is hard to interpret and could cause significant error in measurements. Besides, the calibration and insulation required for accurate measurements are complicated. Therefore, this equipment has only been used for research purposes.

The electro-magnetic based sensors are mostly used for *in situ* soil water potential measurements for the prediction of irrigation scheduling. They measure the water content related electric resistance, capacitance, or heat dissipation of the material with known water retention curve $\Theta(\Psi, T)$. Currently, a Decagon MPS-6 is the best of this class of sensor. It measures the change of the dielectric permittivity of a porous ceramic disk due to the change of water content in the disk. The disk water status changes and equilibrates with the moisture level of the surrounding soils. The electronic response of the disk needs to be calibrated against its water content before application. The water potential of the sample can then be found from the water retention curve of the ceramic disk. A comparison was done between the MPS-6 and the sensor we developed. These sensors have short response time, small form factor, but low accuracy.[37]

Chilled mirror hydrometers are accurate *ex situ* water potential sensors. They measure the water potential of a sample with a high accuracy of ± *0.05 MPa* from *0* to *-5 MPa*, and *1%* from *-5 MPa* to *-300 MPa*. [36] After a measurement starts, the mirror temperature is lowered through a thermoelectric cooler until water vapor starts to condense on the mirror. The condensation will be detected by the photo detector due to the change in the mirror reflectance. The platinum

resistor thermocouple (PRT) on the mirror will record the dew point temperature, which can be translated into water activity. Despite its accuracy, this hygrometer cannot be used for *in situ* continuous measurements. For soil measurements, the destructive sampling will break the integrity of the soil sample. We have been using this method in laboratory to measure the water potential of osmotic solutions. We use the measured osmotic solution for micro-tensiometer calibration.

Tensiometers translate the chemical potential into measurable mechanical tension through the MVLE theory discussed in Section II.A. Conventional tensiometers are the most accurate *in situ* soil water potential sensors. The reduction in liquid pressure can be sensed through the mechanical deflection of the pressure transducer directly attached to the liquid. Commercially available tensiometers have a high accuracy of $\pm 5 \times 10^{-4}\ MPa$, but a short measurement range of *0* to *-0.085 MPa* [38] (Table II-1). The small measurement range is due to the air invasion through the micropores of the ceramic membrane, and defects and impurities that facilitate nucleation in the macroscopic internal reservoir in which the liquid is held. The limited range only allows the sensor to measure well-watered soils for moisture sensitive crops, but not for drier environment.[39] Its relatively large form factor also affects the integrity of the sample.

The high accuracy of tensiometers motivates researchers to extend the measurement range with different approaches. Peck and Rabbidge[40] introduced an osmotic tensiometer in 1966, and extended the operating range to -1.5 MPa. They filled the tensiometers with PEG 2000 solution, and use the osmotic potential of the solution to shift the reference potential of the tensiometer to a more negative value. This method has been developed further to reach a limit of -1.6 MPa.[41] Another approach was to reduce the pore size of the ceramic membrane from microscale to nanoscale; this method extended the limit to -1.5 MPa.[42] The study from our group

has shown that using the MVLE method to connect a small volume of liquid (about 0.1 nL) to the outside sub-saturated vapor through nanoscale porous membrane can reach a liquid pressure of $\Psi_l \leq -20\ MPa$.[43] This discovery initiated the idea to build a micro-scale tensiometer. The MEMS approach significantly reduced the sensing area of the tensiometer. With the first generation micro-tensiometer, our group has successfully extended the measurement range to *-10 MPa*, and significantly reduced the sensing area from >10 cm^2 to 1.2 cm^2.[15] The second-generation micro-tensiometer discussed below has a further reduced form factor of 0.25 cm^2.

II.D. Micro-Tensiometer (μTM)

A micro-tensiometer combines the tensiometry, the piezoresistive MEMS (micro-electric-mechanical systems) pressure sensing technique, and the nanoporous silicon membrane (PoSi). The PoSi increased the capillary pressure the membrane can hold; the small internal volumes (*10 nL*) lowers chance of impurities that can catalyze nucleation. In addition, the clean-room based micro-fabrication process reduced the impurities inside the liquid reservoir, minimizing the possible vapor nucleation sites, and helped extending the measurement range of the sensor.[23]

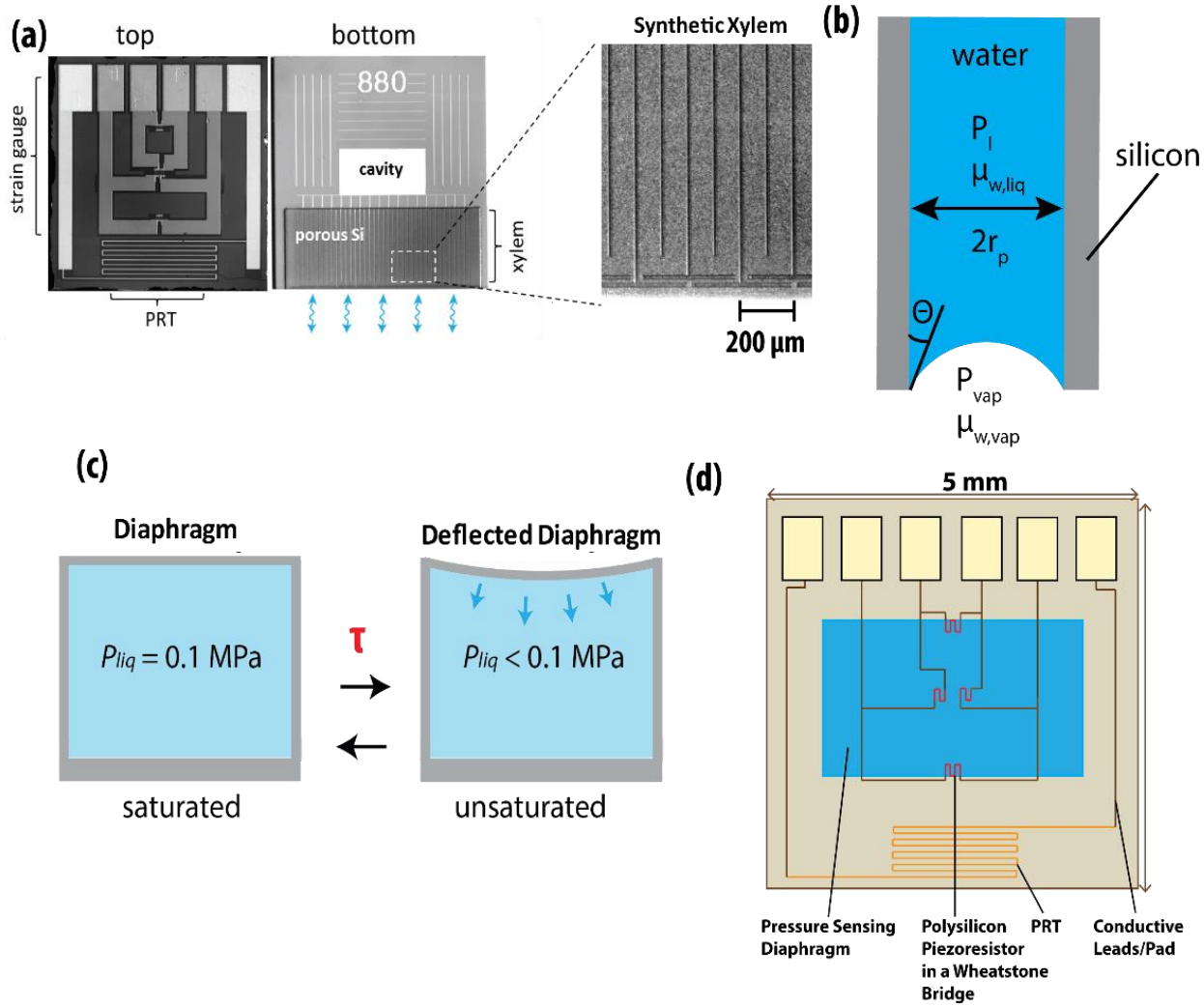

Figure II-5 The Working Mechanism of the Micro-tensiometer (µTM)

(a) Top and bottom side of the micro-tensiometer. To get a functioning µTM, the cavity needs to be filled with water using a high pressure (~3.45 MPa) cylinder. The liquid inside the cavity connects to the outside through nano-porous silicon membrane. An expanded view of the nano-porous silicon membrane with synthetic xylem veins etched was also shown. The synthetic xylem shortens the response time of the sensor. The veins are designed as a balance of immediate response and minimization of the chance of air-invasion due to random defects in the silicon membrane. (b) An enlarged view of liquid water in a nano-scale pore connect to the outside through a curved meniscus. The tension held by the nano-scale pores is determined by the pore size and the contact angle between the liquid water and silicon. The liquid water in the cavity reached metastable equilibrium state with outside sub-saturated water vapor through the capillarity of the nano-scale porous silicon membrane. (c) The cross-sectional view of the cavity and the diaphragm on top of it. The reduced pressure is sensed through the deflection of the diaphragm. The response time constant τ represents the time the sensor takes to respond to a step change of the outside vapor water potential. (d) An enlarged view of the Wheatstone Bridge (BR) and a PRT. The mechanical deflection of the diaphragm is transduced into electronic signal through the piezoresistors in the Wheatstone Bridge. The red resistors on the blue cavity are piezoresistors. The electronic signals are transferred to the outside by wiring the six pads to the outside datalogging system. A PRT (platinum resistor thermocouple) is placed on top of the porous silicon membrane to measure the accurate sample temperature.

II.D.1. MEMS (Micro-Electric-Mechanical-Systems)

The micro-scale pressure sensing system of the micro-tensiometer is based on the well-developed piezoresistive-MEMS-diaphragm pressure sensing technique.[44] MEMS is a technology that builds micro-scale devices with a system of electrical and mechanical components. The MEMS devices are manufactured based on the micro-fabrication technologies. A piezoresistive pressure sensor translates the mechanical stress to electrical signal through a diaphragm with piezoresistors attached. The mechanical stress on a diaphragm is measured through the resistance change of the resistors in response to the stress. The piezoresistive technique has been developed for macro-scale pressure sensing since the 1950's.[45] Combined with MEMS technology, piezoresistive pressures sensors can be manufactured and applied in micro-scale.

Figure II-5 shows the working mechanism of the μTM. Figure II-5-a is the most recent version of μTM. The cavity in Figure II-5-a is first filled with water under high pressure. The internal water connects to the outside through PoSi with nano-scale pores (Figure II-5-b). When measuring the sample water potential, the internal liquid pressure is reduced. The reduced pressure is measured through diaphragm deflection (Figure II-5-c). The deflection will be sensed through the electronics on top of the diaphragm (Figure II-5-d). In a μTM, four piezoresistors were integrated into a Wheatstone bridge (BR) to eliminate the offset and to minimize the temperature effects of the resistors.[46] Two resistors are placed at the top and bottom of the diaphragm to sense the maximum compressive stress (σ_{max}) of the diaphragm. Two resistors are placed at the center of the diaphragm to sense the maximum tensile stress due to the maximum deflection. The signal from piezoresistors are maximized by using heavily boron-doped polycrystalline silicon ($6 \times 10^{19}/cm^3$), and by using a high resistance of 2000 Ω.[47]

II.D.2. Nanoporous Silicon Membrane (PoSi)

The PoSi was etched through anodization: silicon is an anode in the electrochemical etching set-up, and is etched by running current through an electrolyte made of hydrofluoric acid (HF), ethanol and water. [48] The anodization usually has platinum (Pt) as cathode. The etched pore size and structure depends on the crystal orientation of the silicon (<111> in this case), the doping type of the silicon wafer (p-type), silicon resistivity (1-10 Ω-cm), electrolyte concentration, current density, and etching duration. The details of anodization are presented in the Chapter III.

II.D.3. Sensitivity

The sensitivity (*S*) of the sensor depends on the size of the diaphragm, the mechanical properties of the diaphragm material, and the piezo-resistive coefficients of the polysilicon (i.e. the fractional change in resistance per unit stress).

The change in resistance (ΔR) of one polysilicon resistor can be expressed as:

$$\frac{\Delta R}{R_0} = \pi_l \sigma_l + \pi_t \sigma_t \qquad (11)$$

Where R_0 is the reference resistance of the resistor, π_l is the longitudinal piezoresistive coefficient of the polysilicon; σ_l is the longtitudinal stress experienced by the resistor; π_t is the transverse piezoresistive coefficient; σ_t is the transverse stress.[46]

The resistors are designed and placed on the diaphragm such that their transverse stress is negligible, and longitudinal stress dominates. Therefore, for resistors at the edges of the diaphragm and experiencing the maximum compressive stress, their resistance change (ΔR_{edge}) is:

$$\frac{\Delta R_{edge}}{R_0} \cong \pi_l \sigma_{max} \qquad (12)$$

Similarly, for the resistors at the center of the diaphragm and experience maximum tensile stress, their resistance change (ΔR_{center}) is:

$$\frac{\Delta R_{center}}{R_0} \cong \pi_l \sigma_{center} \quad (13)$$

The output voltage from the full Wheatstone bridge is:

$$V_{out} = \frac{V_{in}}{2R_0} \times (\Delta R_{edge} - \Delta R_{center}) = \frac{V_{in}}{2} \times (\pi_l \sigma_{max} - \pi_l \sigma_{center}) \quad (14)$$

The maximum tensile stress and the maximum compressive stress of a rectangular diaphragm have been well studied and their values depends on the diaphragm structure and mechanical properties, proportional to the applied pressure on the diaphragm (ΔP_d) for small deflections. For a rectangle with half-width "a" and half-length "b" (b ≥ a). The internal geometry coefficients are α, β_1 and β_2, which are function of some geoparameters that can be found from literatures.[49]

$$\sigma_{max} = \frac{\beta_1 \Delta P_d b^2}{h^2} \quad (15)$$

$$\sigma_{center} = \frac{\beta_2 \Delta P_d b^2}{h^2} \quad (16)$$

Where h is the diaphragm thickness ($\approx 300\ \mu m$)

The differential output signal ($\frac{V_{out}}{V_{in}}$) and the theoretical sensitivity of the sensor are then

$$S = \frac{\pi_l b^2}{2 h^2} (\beta_1 - \beta_2) \quad (17)$$

$$\frac{V_{out}}{V_{in}} = S \times \Delta P_d + (\frac{V_{out}}{V_{in}})_{os} \quad (18)$$

Where $(\frac{V_{out}}{V_{in}})_{os}$ is the offset of the bridge, which is un-avoidable because the micro-fabrication processes are not ideal.

For accurate measurements, each micro-tensiometer needs to be calibrated to get its experimental sensitivity and offset.

II.D.4. Stability

The stability of the micro-tensiometer are determined by the maximum capillary force the nanoporous silicon can hold, or by homogeneous nucleation or heterogeneous nucleation due to impurities inside the liquid.

The maximum capillary pressure depends on the pore size of the porous silicon membrane, based on equation (1). The pores we have range from *2 nm* to *4 nm* in radius. The typical contact angle between the liquid water surface and the oxidized hydrophilic silicon surface is about *25°*.[50] The surface tension of water is about *72.4 mN/m* at standard temperature and pressure.[51] Theoretically, this pore size range allows a meniscus to hold *-70 MPa* to *-130 MPa* of tension, which is much less negative than the theoretical prediction of the tension (*-140 MPa*) to create a vapor bubble nucleation in pure liquid water.[52] For individual sensors, the stability limit may be less negative than the prediction due to the impurities in the liquid water, or the random defects in the porous silicon.[53]

II.D.5. Response Time

The response time represents the time scale for the sensor to respond to a step change in the outside water potential, which is similar to the charging and discharging time constant of a *RC* circuit. If we treat the internal liquid and diaphragm together as the controlled system, and assume that the water transport inside the porous silicon membrane has reached steady state much faster than the internal liquid, we can get the following governing equation for the mass balance of the liquid

$$\frac{dV}{dt} = -U_D \qquad (19)$$

Where V $[m^3]$ is the total liquid volume; U_D $[\frac{m^3}{s}]$ is the volumetric flow rate of water through the porous membrane based on Darcy's law:

$$U_D = \kappa_{eff}\ (\Psi_l - \Psi_v) \quad (20)$$

Where $\kappa_{eff}\ [\frac{m^3}{Pa-s}]$ is the effective hydraulic conductance of the porous silicon membrane.

The effective bulk modulus ($B_{eff}\ [Pa]$) of the diaphragm-liquid system is

$$B_{eff} = V_{vo}\frac{d\Psi_l}{dV} \quad (21)$$

Where $V_{vo}$is the initial volume of the liquid reservoir.

The governing equation can be translated into a pressure diffusion equation:

$$\frac{V_{vo}}{B_{eff}}\frac{d\Psi_l}{dt} = -\kappa_{eff}\ (\Psi_l - \Psi_v) \quad (22)$$

The hydraulic capacitance of the sensor ($C_{eff}\ [\frac{m^3}{Pa}]$) is

$$C_{eff} = \frac{V_{vo}}{B_{eff}} \quad (23)$$

The hydraulic resistance of the sensor is

$$R_{eff} = \frac{1}{\kappa_{eff}} \quad (24)$$

The response of the sensor is

$$\Psi_l = \Psi_v + (\ \Psi_{l,0} - \Psi_v)\ exp\left(\frac{-t}{R_{eff}C_{eff}}\right) \quad (25)$$

Where $\Psi_{l,0}$ is the initial liquid water potential.

The response of the sensor can be treated as a RC circuit with a time constant ($\tau\ [s]$) of

$$\tau = R_{eff}C_{eff} \quad (26)$$

i. Hydraulic Capacitance of the Rectangular Diaphragm

If we treat the effective bulk modulus of the diaphragm-liquid system as springs-in-series [54], we have

$$\frac{1}{B_{eff}} = \frac{1}{B_d} + \frac{1}{B_w} \quad (27)$$

Where B_d is the bulk modulus of the diaphragm; $B_w = 2.2 \times 10^3\ MPa$ is the bulk modulus of liquid water.

The bulk modulus of the rectangular diaphragm is calculated from the energy of deflection (E_{def}):

$$E_{def} = C_{def} ab \frac{(\Delta P_d)^2 a^4}{D} \quad (28)$$

$$D = \frac{Eh^3}{12(1-v^2)} \quad (29)$$

Where C_{def} is the coefficient associated with energy of deflection; $D\ [N \cdot m]$ is the stiffness of the diaphragm; $E\ [Pa]$ is the Young's modulus of the diaphragm; $v = 0.27$ is the Poisson's ratio for the silicon diaphragm used in the micro-tensiometer.

C_{def} for different diaphragm shapes can be found in Taylor and Govindjee 2004[55] through simulation using numerical methods.

By definition, the bulk modulus of the diaphragm

$$B_d = V_{vo} \frac{dP}{dV} \quad (30)$$

We can get the capacity (K) of the diaphragm:

$$K = \frac{dP}{dV_d} = \frac{B_d}{V_{vo}} \quad (31)$$

$$\Delta P_d = K V_d \quad (32)$$

Where ΔP_d is the pressure on the diaphragm; V_d is the deflected volume due to the pressure

Based on the fundamental definition of work done by an external force on a system in thermodynamics, the amount of work (energy) required from no deflection to a deflected volume of V_d can be expressed as:

$$E = \int_0^{V_{d,f}} \Delta P_d dV_d \quad (33)$$

Where $V_{d,f}$ is the final deflected volume due to ΔP_d.

Combining eq. (32) and (33), we have:

$$E = \frac{1}{2}\Delta P_d V_{d,f} \quad (34)$$

The volumetric deflection of the diaphragm (V_d) can be obtained by modifying eq. (34):

$$V_d = 2\frac{E_{def}}{\Delta P_d} = 2C_{def}\frac{a^5 b}{D} \times \Delta P_d \quad (35)$$

Therefore, based on equation (31) and (36)

$$B_d = \frac{V_{vo}\, D}{2\, C_{def}\, a^5 b} \quad (36)$$

Combining equations (37) and (28)

$$B_{eff} = \frac{1}{\frac{2C_{def}\, a^5 b}{D\, V_{vo}} + \frac{1}{B_w}} \quad (37)$$

ii. Hydraulic resistance of the Synthetic Xylem

The hydraulic resistance of the sensor has been significantly reduced by introducing the synthetic xylem veins structure. The design of the synthetic xylem veins was based on the idea of the how the cavitation was prevented from spreading in the xylem tissue of woody plants which is under negative pressure (Figure II-6).

The hydraulic path defined by this structured membrane can be represented by the circuit diagram in Figure II-6-b. The hydraulic resistance of each element in the circuit can be calculated using the following equation:

$$R_x = \frac{1}{\frac{H_x W_x\, \kappa}{L_x\ \ \phi\mu}} \quad (38)$$

Where x represents 1 to 3; $H_x = 5\ \mu m$ is the thickness of the porous silicon membrane; $W_x\ [m]$ is the width of the cross-sectional area for the water transport; $L_x\ [m]$ is the active length of the porous silicon membrane separating adjacent veins; $\kappa\ [m^2]$ is the permeability of the porous silicon membrane; $\mu\ [Pa \cdot s]$ is the viscosity of water; $\phi = 0.45$ is the porosity of the porous membrane. Since R_1 and R_2 have the same values, R_2 is replaced by R_1 in the following calculations.

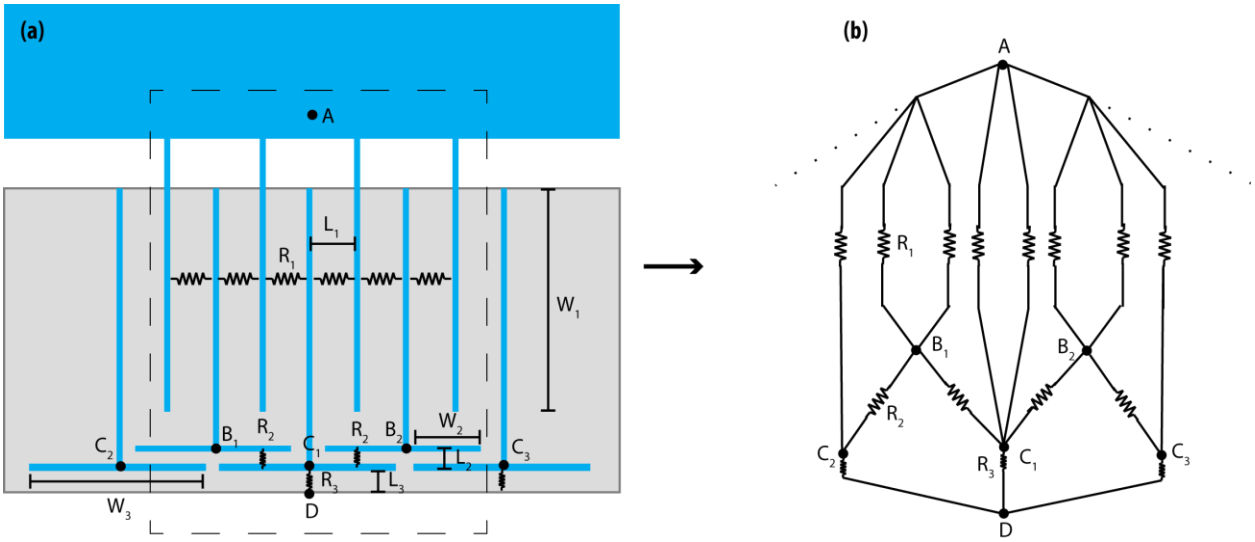

Figure II-6 The Hydraulic Resistivity of the Synthetic Xylem on Membrane

(a) The hydraulic resistivity diagram of the repeated paths connecting the internal cavity to the evaporative surface. The water flow from point A to point B through a porous silicon membrane with a depth of 5 μm, a width of W_1,and a length of L_1. The water flow from B to C through a membrane with a 5 μm thickness, W_2 width and L_2 in length. The water flow from C to D through a membrane with a 5 μm thickness, W_3 width and L_3 in length
(b) Simplified diagram for the study of hydraulic resistivity.

The hydraulic resistance of the synthetic xylem membrane system is

$$R_{eff} = R_{AD} = \frac{1}{n} \times \left(\frac{1}{\frac{2}{R_1} + \frac{2}{\frac{1}{2} \cdot R_1 + R_2}} + R_3 \right) = \frac{1}{n} \times \left(\frac{3}{10} R_1 + R_3 \right) \quad (39)$$

Where n is the number of the repeated of the motif of veins. The theoretical and experimental comparison of the response time and sensitivity are shown in Table III-1.

II.E. Vapor and Tissue Psychrometric Effect during Measurements

The water potential of a sample depends on its temperature. The temperature difference between the sensor and the sample creates an error in measured water potential due to the difference in their reference state of zero water potential. As discussed in Section II.B.1, the water potential measures the energy deviation of a sample from that of pure liquid water at the temperature and pressure of the sample of interest. We call this error is psychrometric effect.

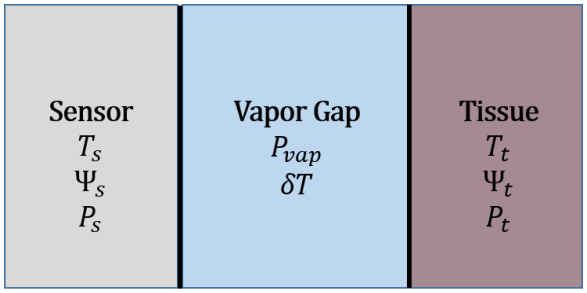

Figure II-7 Illustration of Vapor Psychrometric Effect

We assume isothermal conditions most of the time. However, in situ applications are always non-isothermal. When measuring a plant tissue, for example, a vapor gap exists between the sensor and the tissue due to the non-uniform contact surface as illustrated in Figure II-7. The temperature, vapor pressure and water potential of the sensor are T_s, P_s and Ψ_s, while those for the tissue are T_t, P_t and Ψ_t. The vapor gap in between has a vapor pressure of P_{vap}. We assume

$$T_s = \delta T + T_t \quad (40)$$

$$p_{vap} = p_t = p_s \quad (41)$$

Where δT is the small temperature difference between the tissue and the sensor.

Based on MVLE,

$$\Psi_s = \frac{RT_s}{v_w} ln(\frac{p_{vap}}{p_{sat}(T_s)}) \quad (42)$$

Where

$$\frac{p_{vap}}{p_{sat}(T_s)} = \frac{p_{vap}}{p_{sat}(\delta T + T_t)} \cong \frac{p_{vap}}{p_{sat}(T_t) + \delta T \ \frac{dp_{sat}(T_t)}{dT}} = \frac{p_{vap}}{p_{sat}(T_t)} \cdot \frac{1}{1 + \delta T \ \frac{dp_{sat}(T_t)}{dT} \frac{1}{p_{sat}(T_t)}}$$

$$= \frac{p_{vap}}{p_{sat}(T_t)} \left[1 - \delta T \ \frac{dp_{sat}(T_t)}{dT} \frac{1}{p_{sat}(T_t)}\right] \quad (43)$$

Therefore,

$$\Psi_s = \frac{RT_s}{v_w} ln\left(\frac{p_{vap}}{p_{sat}(T_s)}\right)$$

$$= \frac{RT_s}{v_w} ln\left(\frac{p_{vap}}{p_{sat}(T_t)}\right) + \frac{RT_s}{v_w} ln\left(1 - \delta T \ \frac{dp_{sat}(T_t)}{dT}\frac{1}{p_{sat}(T_t)}\right)$$

$$= \frac{RT_s}{v_w} ln\left(\frac{p_{vap}}{p_{sat}(T_t)}\right) + e_p \quad (44)$$

$$e_p = \frac{RT_s}{v_w} ln\left(1 - \delta T \ \frac{dp_{sat}(T_t)}{dT}\frac{1}{p_{sat}(T_t)}\right) \quad (45)$$

Where e_p is the error due to psychrometric effect. This error is about 7.77 MPa/°C around 25 °C.[56] When the tissue has lower temperature than the sensor, the sensor will read a more negative water potential than the real value. When the tissue has higher temperature, the vapor will condense on the PoSi and make the sensor read zero. Managing the source of error represents an important challenge for the application of the micro-tensiometer, as discussed further in Chapter III.B.

III. MATERIALS and METHODS

III.A. Micro-Tensiometer Preparation

III.A.1. Substrates

Silicon wafers were p-type double side polished wafers with 100 mm diameter and $350 \pm 25\ \mu m$ thickness (Addison addisonengineering.com). They had <111> crystal orientation and $1 - 10\ \Omega \cdot cm$ resistivity; and were selected for porous silicon membrane etching with desired pore size and structure (interconnected structure with pore radius range from 2 nm to 4 nm). Double-side polished Borofloat 33 glass wafer with 100 mm diameter and $500\ \mu m$ thickness, were used to bond with the backside silicon wafer through anodic bonding (University Wafer universitywafer.com) The bonding in the CNF (Cornell NanoScale Science and Technology Facility) clean room created an enclosed reservoir for liquid water with reduced impurities; after bonding, the internal cavity was only connected to the outside through the porous silicon membrane.

III.A.2. Fabrication

A micro-tensiometer requires double side fabrication on a silicon wafer. The backside has etched cavities for the water reservoir and etched nanoporous silicon membrane, and is bonded with a glass wafer. The frontside has a platinum resistance thermometer (PRT) and a Wheatstone bridge (BR). A BR is composed of polysilicon resistors, platinum wires and pads. The whole bonded wafer needs to be diced into 5 mm x 5 mm chips accurately at designated positions to get micro-tensiometers. The fabrication processes below were presented in a chronological order. The steps presented below are labeled in Figure III-1-a.

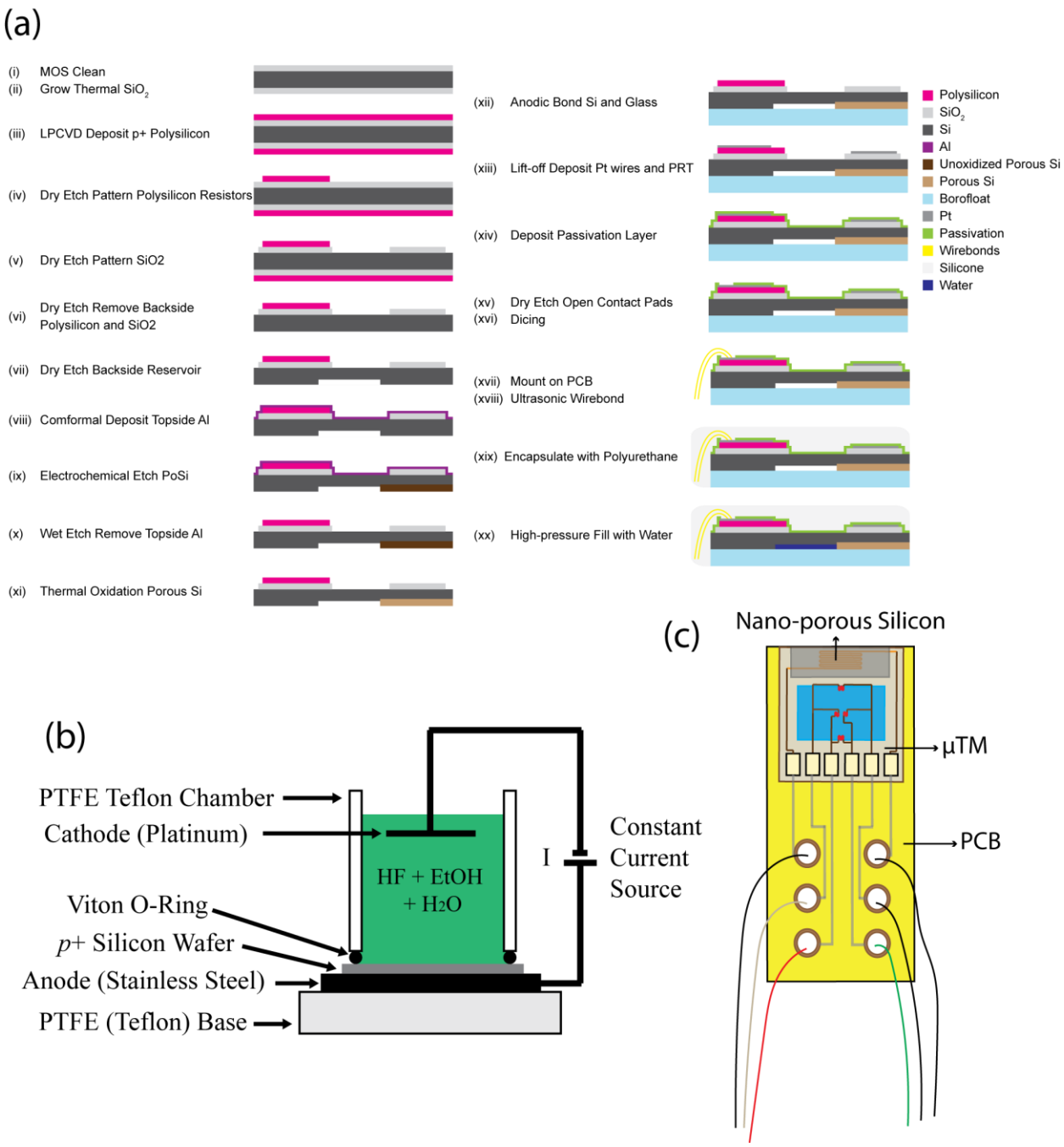

Figure III-1 Preparation of a Micro-tensiometer.

(a) An Illustration Micro-Fabrication Processes. (Courtesy of Michael Santiago)
(b) A Diagram of The nano-scale porous silicon membrane etching bath.[61]
(c) A Diagram showing A µTM mounted to the PCB board with external wires for datalogging. The pads are connected to the PCB board through wire-bonds. The internal cavity connects to the outside vapor through nano-porous silicon.

Steps i and ii: Growth of SiO2 Insulation Layer

After MOS clean for the silicon wafers, the 800 nm SiO2 insulation layer was grown into silicon wafer by using the MRL Thermal Oxide Furnace through oxidation. The SiO2 insulation is important because the silicon wafer is conductive to electronics, and would disturb the operation of the polysilicon resistors. The oxidation was a batch process, and 25 to 50 wafers were able to be processed at the same time. The resistivity of the silicon wafers was checked before the oxidation process using CDE ResMap 4-pt Probe. The wafers were first MOS cleaned and then oxidized in the furnace using wet oxygen and nitrogen flow mixed with hydrogen chloric acid at 1000 °C for 200 min. To ensure the uniformity of the grown SiO2, baffle wafers were used at the first and the last position of the series of wafers, hydrogen chloric acid was added to the oxygen flow to ensure good oxide quality at a high growth rate, and to help prevent defects in the oxidation layer.

Step iii: Deposition of Polysilicon Layer Deposition

A 800 nm thick polycrystalline silicon layer with a boron doping level of $6 \times 10^{19}/cm^3$ was deposited on top of the SiO2 insulation layer in MRL LPCVD Polysilicon furnace. This high doping level was chosen to optimize the signal and minimize the temperature effects. The deposition was done with a feeding rate of 270 sccm of 1.5% B2H6 and 90 sccm of 30% SiH4 at 620 °C for 130 minutes. The polysilicon layer was then annealed in MRL MOS Clean Anneal with Inert gas (Ar) at 900 °C for 30 min. The polysilicon-SiO2 layer were checked in Filmmetrics for their thickness, and in CDE ResMap 4-pt Probe for their resistivity.

Step iv: Patterning of Polysilicon Resistors

The polysilicon resistors were fabricated using photolithography with S1827 photoresist and dry etching. The pattern of the resistors was generated using the general photolithography

process with the mask for resistors. The patterned wafers were etched using Oxford 81 Plasma Etcher with SiF6/O2 (125 mTorr, 45 SCCM SF_6, 15 SCCM O_2, 100W). The RF plasma dissociated SiF6 into fluorine (F*) and other fragments. F* and Si reacted to form SiF4 or SiF2 products because Si-F has stronger bond than Si-Si. Oxygen kept fluorine concentration high, prevented them from recombination their dissociated fragments, and led to stable end products of plasma etching. The etching depth was checked using P10 Profilometer (P10). The etching was stopped when the color of SiO2 layer appeared blue/purple/green, because SiO2 with different thickness shows different color. (BYU clean room, http://www.cleanroom.byu.edu/color_chart.parts/sio2_chart.jpg)

Step v: Patterning of SiO2

The SiO2 insulation layer was fabricated using photolithography (S1827) and dry etching. After the wafers were patterned with the mask for SiO2 patterning, the patterned wafer was dry etched in Oxford 81 using CHF3/O2 (50 mTorr, 50 SCCM CHF_3, 2 SCCM O_2, 200W) for 20 min, which depends on the etch rate measured by P10. CHF3/O2 has higher selectivity against silicon, which is favored in this case. The end products were SiF4 and CO2, which had stronger bonds than Si-O bond. The etching was stopped when the color of the Silicon wafer appeared. The fabricated resistors had a typical resistance of 2000 Ω. Figure II-5-e shows the shapes of the resistors.

Steps vi and vii: Patterning of Backside Cavity

The backside cavity was created by dry etching 3 μm into the silicon wafer. The SiO2 and polysilicon layers on the backside were removed using the same dry etching method for their fabrication. The residues were removed using a dip in BOE 6:1 (butter HF etch). The backside

cavity was patterned using the designated mask with S1827. The etching was done in Oxford 81 using SF6/O2 mentioned above. The etching rate was controlled using P10.

Steps viii to xi: Backside Patterning and Etching of Porous Silicon

The porous silicon membrane was patterned through general photolithography using the AZ P4903 thick photoresist ($6\ \mu m$). This photoresist protected the un-exposed area from etching in electrochemical bath during Anodization. The porous silicon etching was done in an electrochemical etching bath shown in Figure III-1-b. The electrolyte was a mixture of concentrated HF (49% HF Aqueous solution, Sigma Aldrich). and Non-Denatured Ethanol (Sigma Aldrich). (Safety Warning: HF is corrosive and contact poisonous; Working with HF requires personal protection equipment) The cathode was a platinum pad. The aluminum was deposited conformally on the frontside of the silicon wafer to make electrical contact with the aluminum anode by using the CHA Mark50 Evaporator of NBTC (Cornell Nano-biotechnology Center) in the clean room. To prevent electrolyte corrosion of the aluminum, a cylindrical PTFE (poly-tetra-fluoro-ethylene) Chamber with 76 mm diameter was used on top of the wafer for the electrolyte. The leakage was prevented by using a Viton O-ring between the chamber and the wafer, and by enhancing the contact using screws. The current density was set to 20 mA/cm^2 with Hewlett Packard DC power supply (Model 6634B). The etching duration was 5 min at 1 µm/min, which resulted in an expected membrane thickness of 5 µm. After etching, the wafers were washed using deionized water (DI) and dried in a desiccator to allow the evaporation of HF from the porous silicon, and prevent corrosion. The aluminum on the frontside was removed using AZ 300 MIF developer to prepare for further fabrication of electronics.

The pores of the etched membrane were then oxidized using Rapid Thermal Anneal (RTA, AG Associates Model 610) at 700 °C in pure oxygen for 30 s with 10 °C/s ramping. The

oxidation of the porous silicon creates Si-O bonds on the silicon surface, and made the pores more hydrophilic, which resulted in higher sensor stability.

Step xii: Backside Silicon Wafer Anodic Bonding with Glass Wafer

The bonding was done in vacuum at 400 °C using 1500 V DC in SUSS SB8e Substrate Bonder (SUSS). Both glass wafers and silicon wafers were thoroughly cleaned before bonding to minimize the organic residues on wafers, which is crucial for sensor stability. The glass wafers were cleaned in nanostrip (90% sulfuric acid, 5% peroxymonosulfuric acid and <1% hydrogen peroxide). The silicon wafers were cleaned using organic solvents acetone and IPA, followed by DI water rinse and drying. The silicon wafers were not washed using nanostrip because the nanostrip could damage the etched PoSi. The wafers were then descumed in Anatech using oxygen plasma before bonding. The vacuum environment in the bonder prevented wafer contamination. The 400 °C bonding temperature softened the glass, and made it conform on the silicon for irregularities, which improved contact. The high temperature also dissociates the sodium oxide (Na2O) in glass into sodium ions (Na^{2+}) and oxygen ions (O^{2-}). The positive voltage on the silicon drove the O^{2-} migration towards the bonding surface and created Si-O bonds at the surface, which enhanced the bonding strength. [48]

Step xiii: Fabrication of Frontside Electronics

The wafers were deposited with Ti (15 nm)/Pt (200 nm) /Ti (15 nm) metal layers through lift-off in CVC E-gun Evaporation System (CVC, model SC4500). The electronics were patterned using the mask for electronics with LOR 5A and S1827 photoresists. The exposed area on the wafer (SiO2 insulation layer) were descumed using Anatech to ensure better contact with the metal. The Titanium layers at the bottom and the top of Pt enhanced the adhesion of metal

with the SiO2 insulation layer at the bottom, and with the passivation layer at the top (discussed below). The rate and thickness of deposition were monitored through CVC directly.

The lift-off was done using the LOR remover, 1-methyl-2-pyrrolidinone (1165, provided by CNF), in 60 °C while sonicating for 30 min. Another 30 min of sonication was done to ensure clean removal of all photoresists. The wafers were then rinsed using DI water and dried.

The resistances of the Wheatstone bridge and the PRT were checked using the IV probe station in the CNF clean room, with expected values to be 2000 Ω and 1500 Ω respectively. The contact resistance and linearity between the electronic wires and the polysilicon resistors were checked as well.

Steps xiv and xv: Deposition of Frontside Passivation Layer

The passivation layer was deposited to protect the electronic on the wafer. The wafers were cleaned in organic solvents acetone and IPA and descumed in Anatech to better adhesion. The passivation layer was composed of 400 nm SiO2, 300 nm silicon nitride (SiNx), 200 nm of oxynitride (SiON), and 100 nm of SiO2 in order at 200 °C in Oxford PECVD. The duration for each component was calculated based on the deposition rate set in the PECVD.

The contact pads for external wiring were opened through photolithography (S1827) using the mask for contact pads opening, and dry etching using CHF3/O2 in Oxford 81. The possible residues of SiO2 and Ti on the opened pads were cleaned using brief dip in BOE 30:1.

The resistances and linearity of the electronics were checked again in the IV probe station. The photoresists were cleaned using organic solvents followed with DI rinse and drying.

Step xvi: Dicing and Labeling of Sensor

The wafers were diced using DISCO Dicing Saw with an all-purpose blade that cuts the glass-silicon bonded wafer. The dicing was done accurately based on the dimensions of the

sensors (5 mm x 5 mm) and the position of the porous silicon membrane. The sensors were labeled from 1 to 230 on a single wafer. The wafers were labeled alphabetically based on the order they were fabricated. For example, the P187 device used below was the number 187 device from P wafer.

Steps xvii to xix: External Wiring and Packaging

The sensor chips need to be wired up to send signals outside. The external wiring for the sensor is composed of the wire-bonding between the chips and the printed circuit board (PCB, oshpark.com), and the wires soldered to the PCB for external data acquisition (Figure III-1-c).

Since the wirebonds were the weakest part of a packaged μTM, the copper contact pads on the PCB board were designed so that minimum number of wirebonds were needed and the shortest wirebond length was needed between the pads on μTM and the copper pads on the PCB. The copper pads were connected to the outside by soldering external wires to the holes designed on the PCB board, as illustrated in Figure III-1-c.

To add external wires, the chips were first glued onto the PCB boards using the 5min set epoxy (LOCTITE). The Wire-bonding connected 32 μm-thick aluminum wires between the contact pads and the PCB board, and was done using the WESTBOND 7400A ultrasonic wire bonder from the CNF. The PCB board were soldered with external wires, which could be connected to an external datalogger (CR6 from Campbell Scientific).

The packaging is important to protect the sensors from external corrosion and possible damage during use. The wire-bonds, which were the most fragile part due to the thin wires and delicate bonding to pads, were potted with a material designed for wire-bonding (9001-E-v3.1, DYMAX). This material had features of fast curing and small stress on wire-bonds. After applying the material on the wire-bonds, the 9001 was cured for 35 min using 365 nm

wavelength and 3000 μW/cm^2 intensity UV light (SPECTROLINE, Model BIB-150P), followed by 15 min heat cure in 150 °C. The whole sensor-PCB system were packaged using polyurethane resin UR5041 (ELECTROLUBE) with high tear resistance and osmotic solution resistance to protect the sensors from external stress during applications and the electronics from external corrosion by osmotic solution. The resin and the hardener of UR 5041 were mixed in a weight ratio of 3.64:1 before use. The curing was 24 hours at room temperature. To facilitate handling and insertion, the encapsulation was done by potting the sensor-PCB in a proper size garolite tube (McMaster-Carr). This tube material has as high of a tensile strength as metal tubes, but much lighter. The encapsulation strategy may vary due to the experiment purposes, as shown in Section III.B.3.i.

III.A.3. Bridge Calibration and Stability

The electronic signal needs to be translated into mechanical signal through calibration. Each sensor needs to be calibrated before being put into use. The calibration was done against a precise pressure gauge (Honeywell, TJE model, 34 MPa). The sensors were first filled with water using a high pressure chamber (HIP High Pressure Equipment Company, Model 37-6-30) at about 3.45 MPa for 6 hours (Figure III-2-a.). Once filled, the sensors were connected to the CR6 datalogger, while letting the sensor cavitate. The maximum output from the sensor before cavitation was taken to be the stability limit of the sensor, and could be translated into pressure data after calibration. After cavitation, with the cavity empty but the PoSi was still wet, the μTM was put into a high-pressure chamber immediately. This chamber was connected to a compressed pure nitrogen gas cylinder (Airgas) through a regulator valve. After the compressed nitrogen gas was fed into the cylinder, the cylinder gas pressure was sensed by the Honeywell pressure gauge (Figure III-2-b & d). The PoSi was kept wet during the entire calibration process because the

menisci block entry of gas into the cavity; the capillary pressure of the menisci held the pressure difference between inside cavity and outside as the outside gas was pressurized. This pressure difference was sensed by the μTM through the deflection of the diaphragm, as presented in Section II.D.2. The sensor reading was then calibrated against Honeywell output for each step-change of gas pressure. Since gas temperature went up every time more gas was filled into the pressure chamber, and relaxed back to room temperature after about several minutes, both PRT and bridge output were recorded during the bridge calibration, and the duration for each pressure step was long enough for temperature relaxation.

The pressure bomb calibration data analysis was done using the following equation

$$V_{out}(P,T) = m_{P+T} * P_{hw} + b_{P+T} \quad (46)$$

Where $V_{out}(P,T)$ was the bridge output from sensor, and was a function of both temperature and pressure inside the chamber; P_{hw} was the honeywelll reading; m_{P+T} was the experimental calibration coefficient, which, in general, was a function of temperature; b_{P+T} was the offset of the bridge, which was also a function of temperature. These two parameters could be obtained from fits as in Figure III-2-d.

Based on the discussion above, we had a theoretical calibration for the sensor output

$$V_{out}(P,T) = V_{out}(P) + V_{out,0}(T) \quad (47)$$

$$V_{out}(P) = m_{BP} * P_{hw} + b_{BP} \quad (48)$$

$$V_{out,0}(T) = m_{BT} * T + b_{BT} \quad (49)$$

Where m_{BP} and b_{BP} are calibration coefficients only for the pressure-dependent term ($V_{out}(P)$), and m_{BT} and b_{BT} are calibration coefficients only for the temperature dependent term ($V_{out}(T)$).

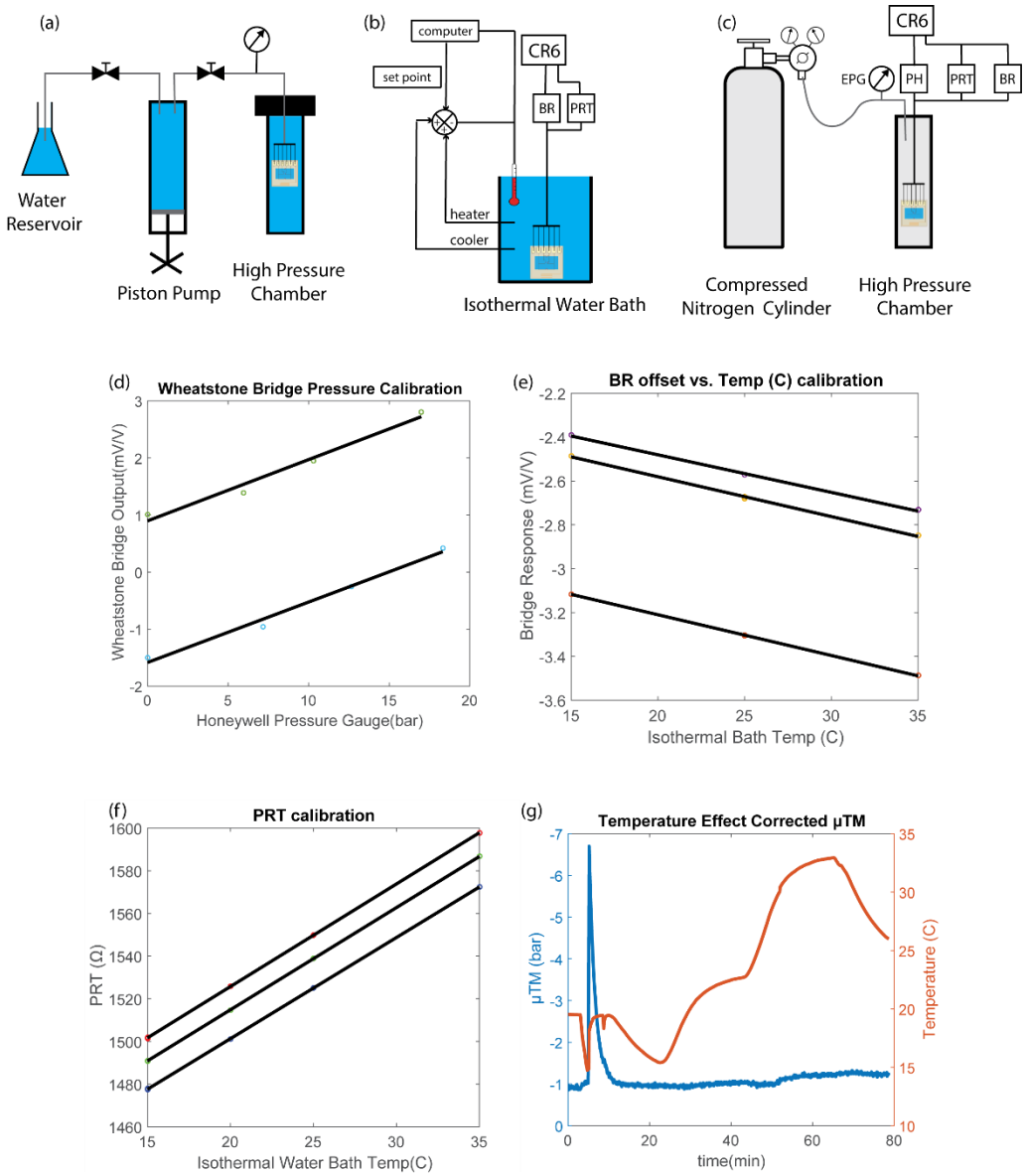

Figure III-2 Sensor Filling, Bridge and PRT Calibrations Illustrations.

(a) Sensor filling system. Sensors are filled using high pressure water (~3.45 MPa) for > 6 hours.[64] *(b) Sensor calibration set-up. The sensors are calibrated using step-change of gas pressure from a compressed nitrogen cylinder monitored using a Honeywell pressure gauge (PH). The response of the Wheatstone Bridge (BR) and PRT is monitored through CR6 datalogger. (Modified from Pagay 2014*[64] *) (c) Temperature control water bath for BR offset and PRT calibration: The sensor response is calibrated against a step-change of the water bath temperature. (d) Pressure calibration curves for two sensors labeled with difference colors. The slope of the line regression is the sensitivity of the sensor. The intercept with the y-axis was the offset (e) BR offset calibration curve for three sensors labeled with three different colors. The slope of a curve was the BR temperature sensitivity. The intercept was the offset of the BR at 15ºC. (f) PRT calibration curve for three sensors labeled by three different colors. The slope and intercept were calibration parameters for a PRT. Different calibration coefficients specified for each diaphragm size is shown in table III.1. (g) Temperature Corrected Sensor Response. The temperature corrected response from the µTM due to a 15ºC temperature change was -0.35 bar. The peak at the beginning proved a functioning µTM by responding to air water potential.*

To correct for the temperature effect on the bridge output, the bridge offset was calibrated against temperature for m_{BT} and b_{BT}. The calculation of m_{BP} and b_{BP} is presented in the following section.

III.A.4. The Bridge and PRT temperature calibration

Since material properties change with temperature, the bridge offset and PRT response were calibrated against temperature using a temperature-controlled water bath (Fisher Scientific). The calibration set-up was shown in Figure III-2-c.

Based on the temperature calibration data, we got the PRT calibration curve ($PRT(T)$), as well as the bridge offset dependence on temperature ($V_{out,0}(T)$, Eqn. (49)).:

$$PRT(T) = m_T * T + b_T \quad (50)$$

Where m_T and b_T were PRT calibration coefficients. The calibration parameters for Eqn. (49) and (50) could be obtained from Figure III-2-e and f.

The $V_{out}(P)$ term can be calculated as below:

$$V_{out}(P) = V_{out}(P,T) - V_{out,0}(T) = V_{out}(P,T) - \left(m_{BT} * \frac{PRT(T)-b_T}{m_T} + b_{BT}\right) \quad (51)$$

The experimental m_{BP} and b_{BP} could now be obtained by plotting $V_{out}(P)$ against P_{hw} where the temperature dependence of the Honeywell was ignored (5×10^{-4} MPa/°C). In other words, the m_{BP} and b_{BP} may have some dependence on temperature, but this effect has been neglected in current studies.

During the use of the sensor, we measured the $V_{out}(P,T)$ and $PRT(T)$ output directly from the sensor. The temperature and pressure can be easily calculated from the two equations below:

$$T(PRT) = \frac{PRT}{m_T} - \frac{b_T}{m_T} \quad (52)$$

$$P_{measured} = \frac{V_{out}(P)-b_{BP}}{m_{BP}} \quad (53)$$

Combining with equation (53)

$$P_{measured} = \frac{V_{out}(P,T)}{m_{BP}} - \frac{(m_{BT}*T+b_{BT})+b_{BP}}{m_{BP}} \quad (54)$$

The output from the CR6 could be converted directly to pressure reading corrected for temperature effects by using $1/(m_{BP})$ as the input multiplier, and $-\frac{(m_{BT}*T+b_{BT})+b_{BP}}{m_{BP}}$ as the input offset (Appendix VIII.C). An example of a temperature corrected sensor was shown in Figure III-2-g. A 0.35 –bar difference in offset was observed while the temperature was changing from 15 °C to 32 °C.

III.A.5. Response Time Testing Through Osmotic Potential Measurement

As discussed before, the response time is the time constant for a sensor to respond to a step change in the sample water potential (Eqn. 26 and 27). To test the response time, a µTM was calibrated using the positive pressure gas cylinder method shown in Figure III-2-a. The measuring tip of the µTM was protected using an expanded PTFE membrane (ePTFE, Porex, PMV10). The PTFE membrane only allowed vapor, not liquid water, to diffuse through. Figure III-3-b showed the plot of the sensor response to a -19.1 osmotic solution through the ePTFE

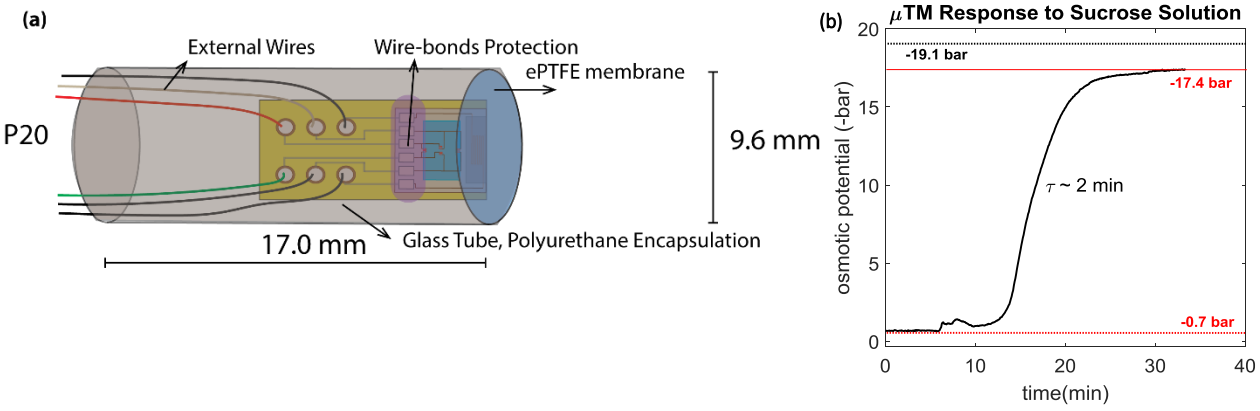

Figure III-3 Measurements in Osmotic Solutions: µTM Response Time Scale and Accuracy.

(a) Diagram of the packaged sensor tested for the osmotic response. (b) Plot of the sensor response to a step change from pure liquid water to a -19.1 bar sucrose solution in isothermal water bath (25 °C). The dashed red line represents the offset of the sensor reading was -0.7 bar. The solid red line represents the final reading by the µTM. The dashed black line represents the osmotic potential (-19.1 bar) measured by the chilled mirror hygrometer. The time constant (τ) for this response was about 2 min.

membrane. The μTM was kept in pure water at the beginning, and was then removed from the pure water, briefly held in the air, and submerged in the sucrose solution (Sigma-Aldrich). The activity of the solution was checked using a Chilled-Mirror hygrometer (Decagon WP4C). The tensiometric measurement was done in an isothermal water bath to prevent psychrometric effect in the ePTFE membrane, as discussed in Section II.E.

In Figure III-3-b, after removing the offset, the μTM showed a 0.2 MPa lower water potential than the WP4C. This difference was larger than the error range of WP4C (± *0.05 MPa* for *0* to *-5 MPa* range). The possible reasons are: 1) the error comes from the Honeywell Pressure sensor, against which the BR was calibrated; 2) the water adsorbed onto the sensor was brought into the solution and diluted the osmotic solution. Further testing needs to be done to clarify the reason for the difference.

Table III-1 shows typical response times, pressure sensitivities, and temperature sensitivities, and stability for different diaphragm sizes measured through experiments, and predicted based on the theory discussed in Section II.D. The measured transient time if about two orders of magnitude larger than the predicted transient time. Since the transient time was measured experimentally using an osmotic solution with known water potential, the solutes might have accumulated in the PoSi and increased the hydraulic resistance of the porous silicon

Table III-1 Transient, Sensitivity and Temperature Sensitivity of the Micro-Tensiometers

Diaphragm Size	τ (response time constant)		S (Sensitivity)		Bridge Temperature Sensitivity	Stability (P_{cav})
mm x mm	seconds		(mV/V/bar)		(bar/C)	(bar)
	Predicted	Measured	Predicted	Measured	Measured	Measured
1 x 2	0.37	40	0.08	0.033	0.70	162
1.5 x 3	1.14	150	0.19	0.085	0.26	130
2 x 3.5	2.74	250 to 600	0.32	0.143	0.15	90

layer. Another possibility is that a boundary layer exists due to the loss of water from the porous silicon membrane to the neighboring solution and diluted the solution locally. The characteristics of the porous silicon membrane might also be changed due to the storage environment or the solution and resulted in change in its hydraulic resistance. Among the three major diaphragm sizes, the 1x2 device has the fastest response time, but smallest sensitivity and the largest temperature sensitivity, while the 2x3.5 device has the slowest response but the best sensitivity and minimum temperature sensitivity. The properties of the 1.5x3 devices lie in between those of the 1x2 and 2x3.5 devices. Although, 1x2 devices typically had the highest stability, and 2x3.5 devices had the lowest stability, the stability limits varied significantly from device to device and should be confirmed before application.

III.B. Greenhouse Experiments

III.B.1. Apple Trees Growth Information

The apple trees (Malus Domestica) were grown in the Yellow Greenhouses on Cornell Campus. They were 2.5 to 3.0 m in height, with trunks 3 cm to 4 cm in diameter. They were moved from the Cornell Orchard in pots on Feb. 10th, 2016. There were three trees in a row, separated by about 1 m from each other. The distance between rows were about 3 m, and we had three rows in total. Experiments were done from the beginning of April 2016 to the end of June 2016. Greenhouse experiments GH1 and GH3 were trial experiments, whose data are not presented in this thesis. The second greenhouse experiment (GH2) was from April 8th, 2016 to May 6th, 2016. The fourth greenhouse experiment (GH4) was from May 26th, 2016 to June 26th, 2016. The trees were well-watered before experiments. They had apples growing during the two experiment periods. (We acknowledge Dr. Lailiang Cheng for the apple trees)

III.B.2. Greenhouse Experiment 2 (GH2)

i. Devices and Data Acquisition

One µTM (M45) was used in GH2. A Scholander pressure chamber (SOILMOISTURE Equipment Co.) was used to measure the stem water potential as a benchmark for the sensors. (We acknowledge Dr. Alan Lakso for the pressure chamber.) The packaging strategies of the µTM are shown in Figure III-4. The GH2 data were logged with a CR6 powered by a sealed rechargeable battery BP7 (12 V, 7 Ah) from Campbell Scientific. A program was written using CRBasic (datalogging programmer by Campbell Scentific) to excite the bridges by 200 mV, and the PRTs by 200 mA, every 30 seconds. The program is shown in Appendix (VIII.B). Related weather data including solar intensity were gathered from NEWA from Ithaca Cornell Orchard weather station (http://newa.nrcc.cornell.edu/newaLister/rawdat).

ii. Sensor Installation and Insulation

For round packages, the µTM was installed into the trees by drilling 1 cm deep holes perpendicularly into the tissue below the bark (Figure III-5-i). The packaged sensors were 9.6 mm in diameter. A large guide hole was made by using a 10 mm Jobber's Drill Bit (McMaster), followed by a grinded-down flat tip 9.5 mm Jobber's Drill Bit, to create a flat bottom for better contact between the sensor tip and the tissue. The holes were wetted using tap water after drilling. Since wet wood shrinks after drilling, the size of the drill bits were selected to fit the size of the packaged devices without large gaps. The sensors were pressed into the hole gently. After the sensors were embedded, they were sealed with caulk (McMaster 3008K13) to prevent water loss. The thermal insulation was done by using 3.18 mm-thick neoprene foam sheets (McMaster 8647K81) tightly wrapped around the sensors, followed by wrapping the sensor and the tree together using 1.27 cm-thick Ultra-Flexible Foam Rubber (McMaster 9349K2).

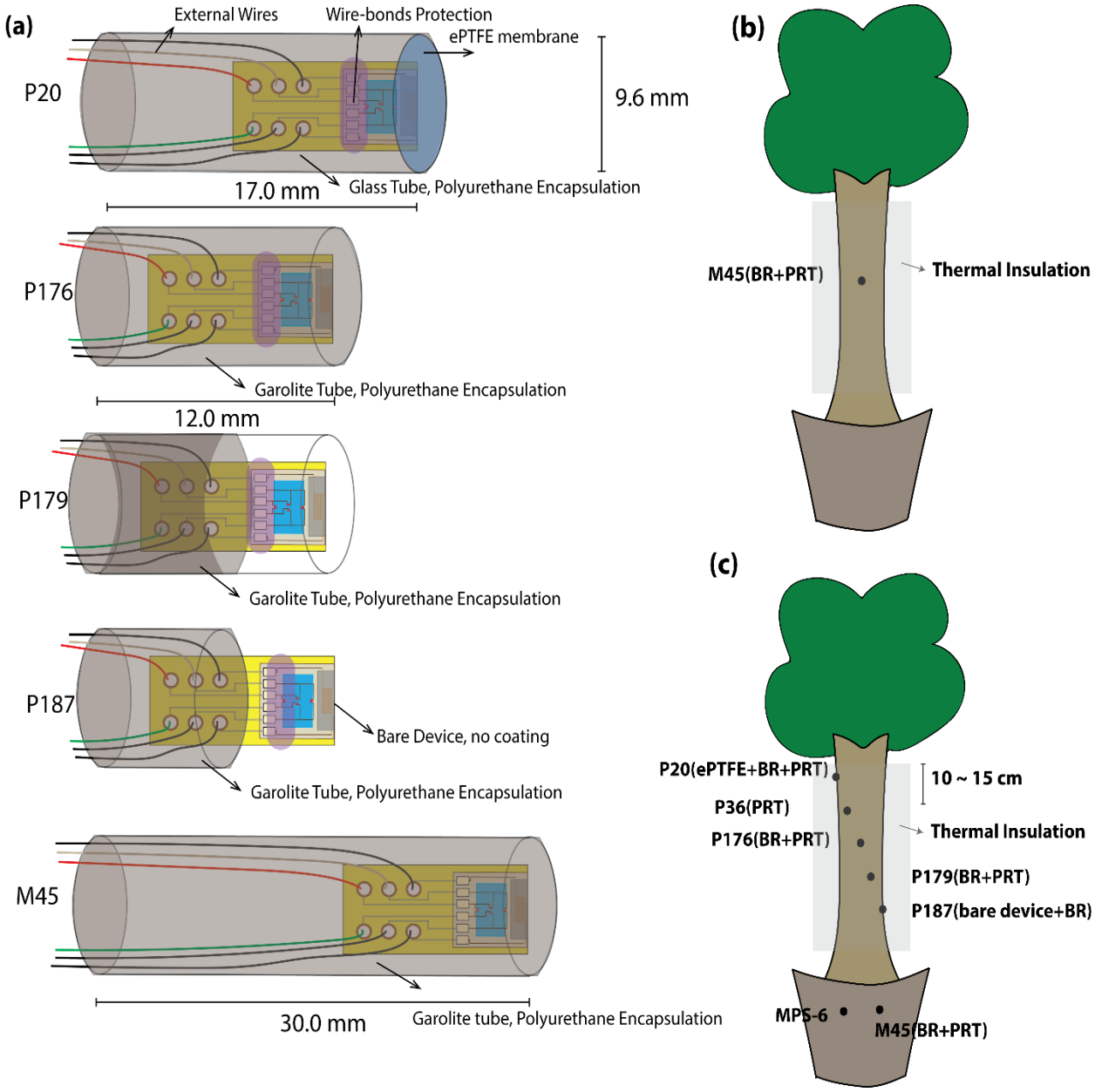

Figure III-4 Set-up Illustration for Greenhouse Experiments

(a) Diagram showing the µTMs used for the greenhouse experiments. The encapsulation material for all sensors was polyurethane. All wire-bonds were protected by 9001 modified polyurethane material designed for wire-bonds. P20 was fully encapsulated in a glass tube, with a ePTFE membrane as a vapor gap between the sample and the sensor. P176 was only fully encapsulated in a garolite tube. P179 was potted up to the wire-bonds, but the garolite tube covered up to the membrane. P187 was encapsulated up to the wire-bonds. M45 was packaged in a longer tube due to a longer PCB board (the length was not shown here). (b) Diagram showing that GH2 had M45 installed. (c) Diagram showing that GH4 had six µTMs. P36 did not have a working bridge, so it only sensed temperature. The sensors on the stem were installed 10 to 15 cm separated from each other, and rotated around the stem. The MPS-6 and M45 were installed in the soil to monitor soil water potential.

Large plastic bags were used to cover the foam as a waterproof layer, and was tightly sealed using zip-ties against the trees. The whole thermal insulation (about 10 cm-thick) was covered by aluminum foil as a reflective insulation to prevent sunlight from heating up the sensor and the insulation system.

iii. Pressure Chamber Measurements

The leaves were wrapped in aluminum foil covered with plastic bags for at least 20 min before they were cut and pressurized (Figure III-5-viii). This method gave us stem water potential measurements.

The pressurization on the leaves were stopped when bubbling started to come out of the cut stem. The bubbles would usually form a liquid droplet after a couple of seconds. The pressurization would be continued if the bubbling stopped and no liquid droplet formed. A pressure bomb measurement was done on a single leaf for each time point.

III.B.3. Greenhouse Experiment 4 (GH4)

i. Devices and Data Acquisition

Seven devices were used in GH4, including five micro-tensiometers (P20, P36, P176, P179 and P187) in the tree, and one micro-tensiometer (M45) and one MPS-6 (Decagon) in the soil. The packaging strategy for the six micro-tensiometers are shown in Figure III-4. The size of packaged sensors was 9.6 mm in diameter. Some of the PRTs on the sensors were broken during the embedding because the sensor edge was chipped when the sensor was pressed against the tree. The installation strategy and packaging will be improved to avoid damaging PRTs in future experiments. The same Scholander pressure chamber was used to measure the stem water potential as a benchmark for the sensors.

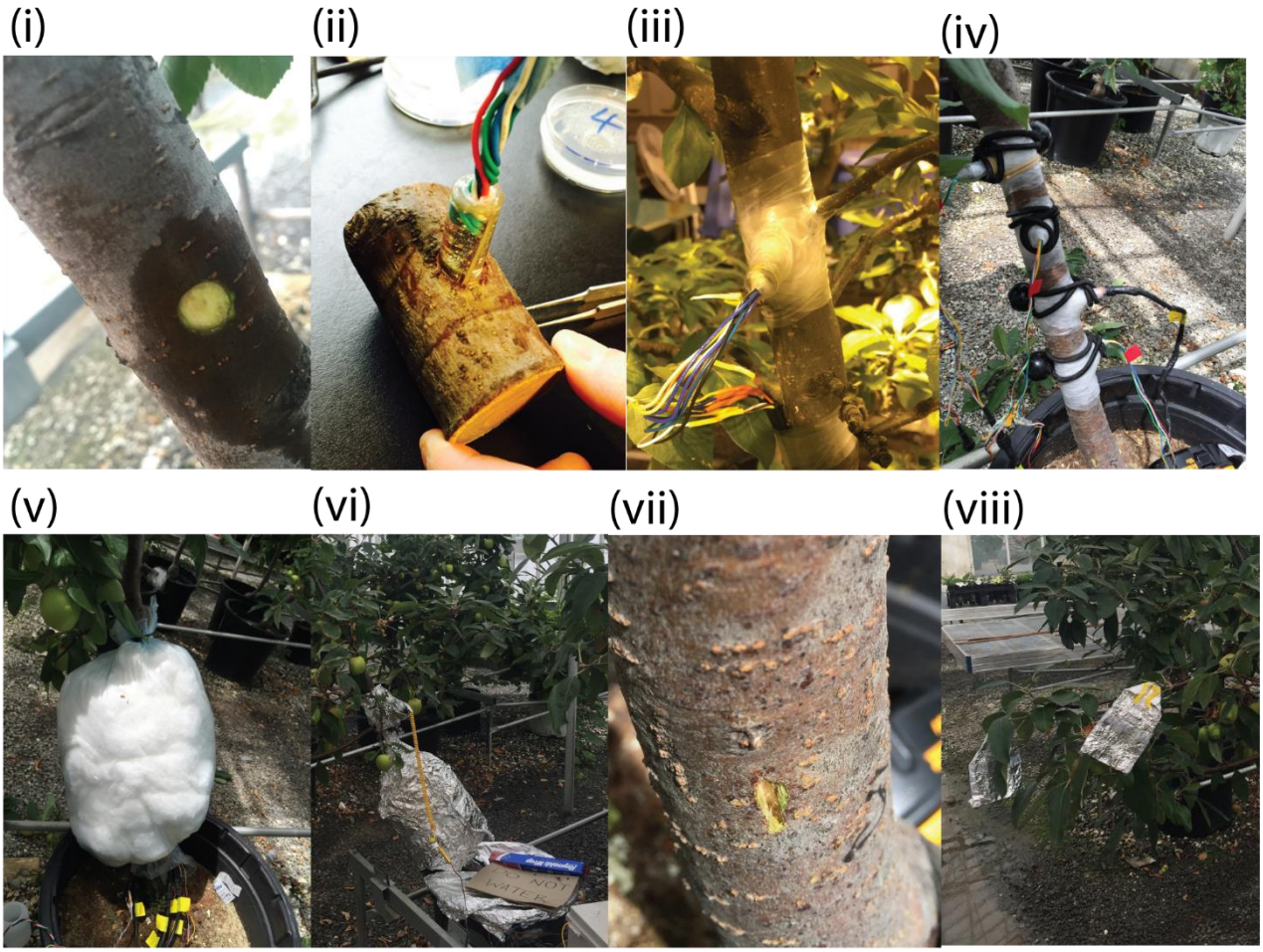

Figure III-5 Photos Showing Micro-Tensiometer Installation and Insulation (GH4)

(i) A drilled hole in a living tree; (ii) Installation of sensor in a cut branch (a picture of installed sensor in a living tree was not taken to prevent sensor cavitation due to water loss); (iii) Stabilization of sensors using plumber's putty and Parafilm; (iv) Reinforcing sensor-tissue contact using an elastic band; (v) Thermal insulation using polystyrene foam and polyester fiber wrapped into a large plastic bag; (vi) Reflective insulation using aluminum foil; (vii) Opening of a slit using a chisel and a knife for the bare device P187; (viii) Bagging a leaf with aluminum foil covered bags for stem water potential measurements using the Scholander pressure chamber.

The data from the sensors were gathered through CR6 connected with a AM16/32B Relay Multiplexer (AM) powered by a BP7 battery. One CR6-AM system was able to operate as many as eight sensors (including one Wheatstone bridge and one PRT per sensor). The MPS-6 was powered using the switched 12V power supply on CR6. The thermocouple was connected directly to CR6 to prevent errors due to extra wiring between the and CR6 and the AM. A program was written in CRBasic to run the devices at the same time, and was shown in

Appendix (VIII.C). The data of the µTMs were taken every 10 seconds as a main program, while the MPS-6 data were taken every 30 s as a minor program in parallel. The bridge was excited using 50 mV, and the PRT was excited using 20 µA. Related weather data including solar intensity were gathered from NEWA as in GH2.

ii. Sensor Installation

The µTMs were filled with water at 3.4 MPa for ≥6 hours using the HiP high pressure chamber (Figure III-2), and brought to the greenhouse submerged in water. The sensors were connected to the CR6-AM in the greenhouse. Data was taken during the entire installation period. For each sensor, a hole of 5 mm depth was drilled using a 9.6 mm diameter Forstner Bits (McMaster 3216A21). The holes were made in the radial direction with respect to the trunk, and were then wetted using tap water to prevent drying of the tissue around the hole (Figure III-5-i). The P187 device was a bare device with no polyurethane packaging on top of the diaphragm. Therefore, this device was installed by using a chisel and a blade to open a slit vertically below the bark (Figure III-5-vii). This method resulted in less damage to the tissue relative to that induced by the drill. The µTMs were then inserted into the holes gently (Figure III-5-ii). After installation, the sensors were stabilized using Plumber's Putty sealing cord (McMaster 9408T14), which helped prevent water loss from the hole (Figure III-5-iii). Compared to caulk, the sealing cord provided better mechanical stabilization for the sensors. The sealing cord layer was then wrapped with PARAFILM (Bemis) against the stem as a further stabilization and waterproofing. The contact between the tubular sensors were improved by wrapping an elastic band around the sensor and the tree to hold them together (Figure III-5-iv). The sensors were separated about 10 to 15 cm from each other axially along the trunk, and rotated around the stem to make sure they were not directly on top of one another and blocking the water flow (Figure III-4). Thermal

insulation was done using 3.18 mm-thick neoprene foam sheets (McMaster 8647K81), followed by a thick layer of polyester fiberfill (Air Lite 580/6). The polyester fiber was then used as the second layer of insulation instead of thick foam sheets in GH1 (Figure III-5-v), because the polyester fiber could be easily shaped to provide more intact insulation for the complex geometry of the sensors on the stem. The polyester fiberfill was wrapped in a large plastic bag as in GH4 to prevent water loss from the opened plant tissue. The insulation (about 12 cm-thick) was finished with a layer of aluminum foil, which was also applied to cover the soil as the last step (Figure III-5-vi). The soil sensors (M45 and MPS-6) were installed in a 45° angle against the soil surface, to minimize the disturbance on the soil matrix (Figure III-4-c).[34] The soil sensors were installed at the end of the first drought period, as shown in Figure IV-2. Re-watering after the soil sensors installation improved the soil integrity around the sensors.[34]

iii. Scholander Pressure Chamber Measurements

The measurement methods were the same as in GH2 except that three pressure bomb repetitions were taken to get a range of stem water potential at one-time point.

III.B.4. Data Analysis Methods

The data were analyzed and plotted using MATLAB (MATHWORKS License 554896). The offset of the μTMs were calculated and subtracted from the entire data set based on the night water potential upon two days of watering after the first drought period. The appropriateness of this correction will be assessed in future experiments.

III.B.5. Simulation -- Heat Conduction Between the Tissue and the μTM

To study the temperature difference between the tissue and the sensor discussed in Chapter IV, a 2D-heat conduction model without internal heat generation was built using Finite Difference Methods. In this model, sensors packaged with air or polyurethane (packaged

dimension 10 mm diameter x 12 mm length) were taken to be in direct contact with the tissue with complete embedding (i.e. the whole sensor tube was inside the tree). The heat flux from plants to the outside air was calculated using a well-studied 1D cylindrical heat transfer model. The heat conduction between the tissue and the sensor was simulated using a 2D heat conduction model with top, left and right, three boundary conditions as fixed tissue temperature (T_p), and the bottom boundary condition as fixed heat flux to the outside, as calculated using the 1-D heat transfer model in a cylinder before. I assumed fixed temperature difference between the plant tissue and the outside air (T_{out}), therefore $\theta_{cavity} = \frac{T_{cavity} - T_{out}}{T_p - T_{out}}$ represents how close the cavity temperature is to the measured tissue temperature at steady state. The time scale for to reach steady state heat conduction was also recorded.

The program of this simulation is provided in Appendix VIII.E.

IV. RESULTS AND DISCUSSION

IV.A. GH2

The purpose of GH2 was to explore installation and insulation strategies, and to compare the µTM readings with those of the Scholander pressure chamber.

The insulation method was developed in GH2 to prevent water loss from the drilled holes by using large plastic bags, to minimize the disturbance from the outside temperature variations by adding thick polystyrene foam around the µTMs, and to prevent sunlight from heating up the sensors by using aluminum foil as reflective insulation. The optimum insulation method was explained in Section III.B.3.ii. Even though the greenhouse temperature was controlled, there was still an air temperature variation of ± 3 °C during the day.

In Figure IV-1, the Scholander reached a peak value at about 11:00 in the morning, while the µTM reached its peak value at about 16:00 in the afternoon, when the sensor temperature was increasing at the highest rate. Comparing the midday water potential measured by these two difference methods, the M45-µTM reported a 15 bar more negative water potential than the Scholander (Figure IV-1-a). The reason for the mentioned differences might be the vapor psychrometric effect discussed in Section II.E due to the vapor gap and the temperature difference between the µTM and the tissue. Notice that in GH2, the sensor-tissue contact was not reinforced using the elastic bands (Figure III-5-iv), a small vapor gap between the µTM and the tissue could cause significant error (~ 8 MPa/ºC) (Section II.E).

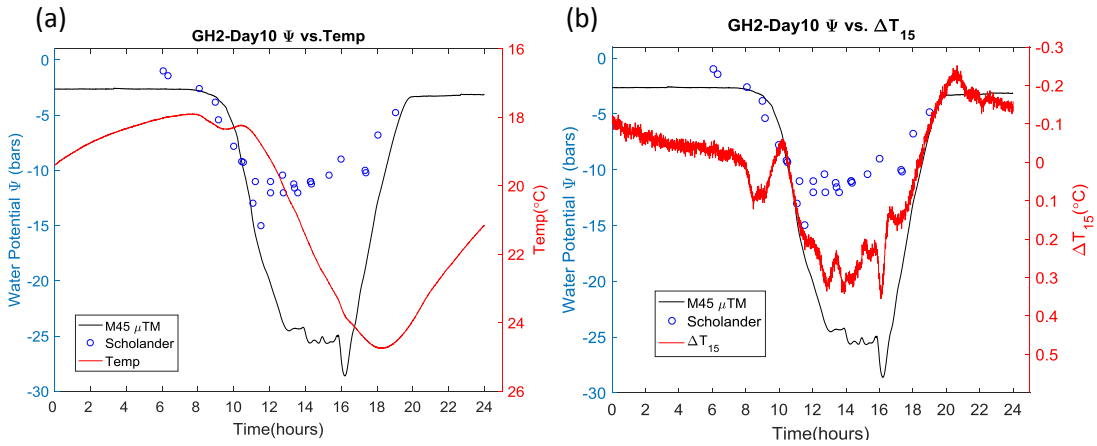

Figure IV-1 GH2--Comparison between the Scholander pressure chamber and the μTM

(a) Plot of M45-μTM measured water potential, scholander pressure chamber measured potential and temperature measured by M45-PRT during one diurnal. The left y-axis represents measured negative water potential (-bar). The right y-axis represents the temperature measured by the sensor M45 and has its positive direction pointing downwards. The x-axis is the time-scale during the day in hours. The black line represents the data from M45. The blue dots are Scholander data. The red line is the temperature measured by the M45-PRT. The stem water potential decreased during the day, and increased at night. (b) Plot of the measured water potential and the "temperature gradient". The right y axis is the $\Delta T(-15min) = T - T(-15min)$*, which was expected to represent the temperature difference between the μTM and the tissue in direct contact. It has its positive direction pointing downward.*

To study the effect of the vapor psychrometric effect, the possible temperature difference (ΔT) between the measured sample and the μTM was estimated by subtracting from the current temperature of the sensor (T) measured by the M45-PRT, the temperature at an earlier time point. The rational is that when temperature increases at the site of the sensor, we expect that there is a radial gradient of temperature along which heat flows from outside in. We take the rate of change in temperature as the radial gradient. The best correlation between the ΔT and the μTM happened at a 15 min time difference, as shown in Figure IV-1-b, after comparing with the temperature 5 min, 15 min, 25 min and 45 min earlier. The temperature dependence of the μTM was observed in Figure IV-1-b: the stem water potential measured by the μTM varied similarly as the $\Delta T(-15min)$.

Based on the simulation explained in Section III.B.5 (code displayed in Appendix VIII.E), for a fixed temperature difference between the plant tissue and the outside air ($T_p - T_{out}$), under steady state heat conduction, θ_{cavity}~0.52 for a sensor packaged in both polyurethane and air. The higher the θ_{cavity}, the closer the cavity temperature to the tissue temperature. We expect a low value of θ_{cavity}, if the sensor was not in good contact with the tissue. This result indicates that a fixed fraction of temperature difference between the sensor and the tissue, which may have resulted in the 15 bar difference as well as the water potential difference at other times of the day, always exists. The simulation also indicated that the time scale for the cavity temperature to reach steady state in polyurethane was one order of magnitude longer than that for a sensor packaged with air. Therefore, to make the μTM measurements more accurate, improving the thermal contact between the sensor and the tissue is crucial. Low profile packaging strategies with minimum polyurethane were tested below in GH4.

IV.B. GH4

Previous results in GH2 motivated the use of multiple packaging strategies in GH4, as described in Section III.B.3, and shown in Figure III-4.

Figure IV-2 shows the chronological record of the entire experimental period. During the day, the stem water potential recorded by the sensors decreased. At night, the sensors reported a higher water potential. The transpiration stopped at night, and the stem water potential increased to values near those of the soil. The tree went through two drought periods (days 1 - 7; days 8 – 22). Each drought period could be recognized by the decrease in predawn stem water potential measured by the sensors. After rewatering (day 7 around 3 pm, and day 22 around 11 am), the predawn stem water potential of the sensors went back to their offset value. Figure IV-3 shows the pictures of the tree before (Day 22) and after rewatering (Day 24). Figure IV-3-a shows the

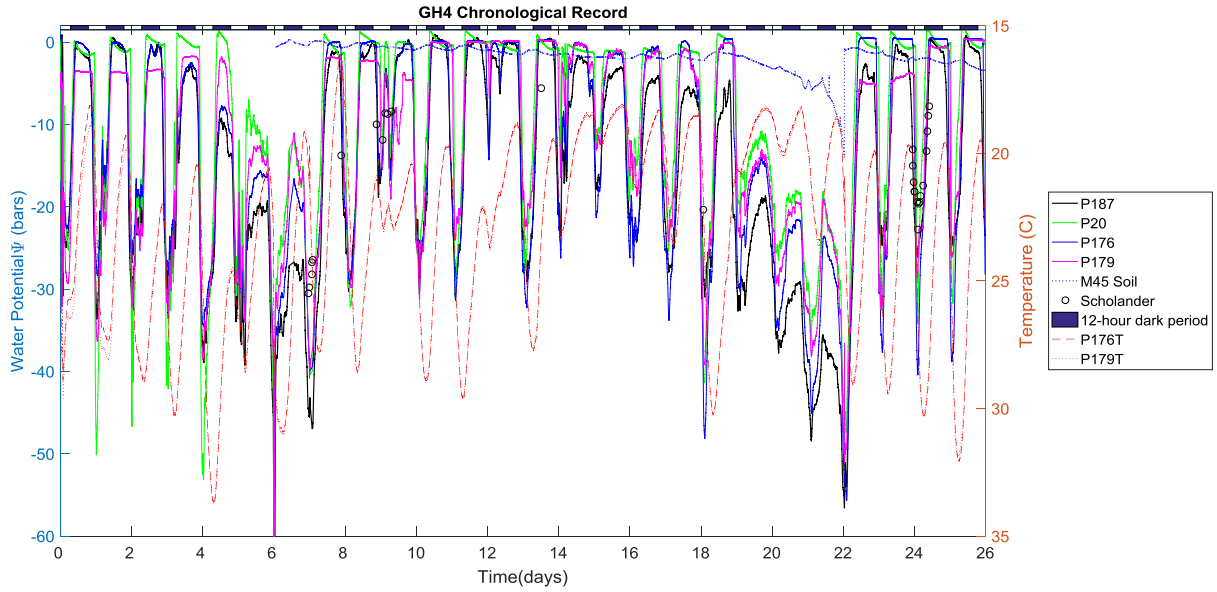

Figure IV-2 GH4 Chronological Record of the Entire Experiment Period

This plot includes the entire data for GH4 experiment. The left y-axis represents the measured stem water potential. The right y-axis represents the measured sensor temperature with its positive direction pointing downward. The x-axis is the time-scale based on days after the sensor installation. The red lines represent the temperature measured by sensors P176 and P179. The black, green, blue, magenta solid lines represent the µTM data from P187, P20, P176 and P179 respectively. P20 had a layer of ePTFE membrane between the plant tissue and the sensor. The black dashed line represents the soil water potential measured by M45. The blue circles with error bars represent the stem water potential measured by the Scholander pressure chamber. The two drought periods were days 1-7 and days 8-22. The dark bars represent the 12-hour dark period from 6pm to 6am. All stem sensors (µTM and Scholander) show that the stem water potential decreased (more negative) during the day, and increased at night. The PRTs measured increased temperature during the day and decrease temperature at night. The first drought period was from day 1 to day 7. On day 7, several Scholander pressure chamber measurements were done. Rewatering was at 2 pm on day 7. The soil µTM and MPS-6 were installed on day 7 as well. The second drought period was from day 8 to day 22. Rewatering was done at 11 am on day 22. More Scholander pressure chamber measurements were done on day 24.

status of the tree when its turgor pressure was significantly reduced due to lack of water. Figure IV-3-b shows the status of the tree after its recovery from rewatering. The data from the sensors were offset corrected based on the predawn water potential measured after three nights upon rewatering, when the tree recovered from drought responses. The M45 soil sensor was installed after the first drought period, showed the decrease in soil water potential for the second drought period progressively, and returned to offset after second rewatering. As expected, the stem

Figure IV-3 The Pictures of the Apple Tree Before and After Re-watering.

(a) Apple tree on Day 22 right before rewatering
(b) Apple tree on Day 24, two days after rewatering.

temperature measured by the sensors increased during the day, and decreased at night. The following discussion covers detailed results from the GH4 data.

Figure IV-4 shows the three days when the Scholander pressure chamber data was taken together with that of the µTMs.

Day 7 (Figure IV-4-a) was during the first drought period before rewatering. The plant was experiencing large water stress. The Scholander measured a water potential of down to -30 bars, while the typical range observed in apple trees is -15 to -20 bars.[57] Therefore, the apple tree was experiencing large stress. The sensors were showing larger tensions than the Scholander (up to -40 bars). There are two possible reasons for this: 1) the µTM was measuring real tension which was much higher than the coverage of the pressure chamber (0 to -40 bar); 2) during the

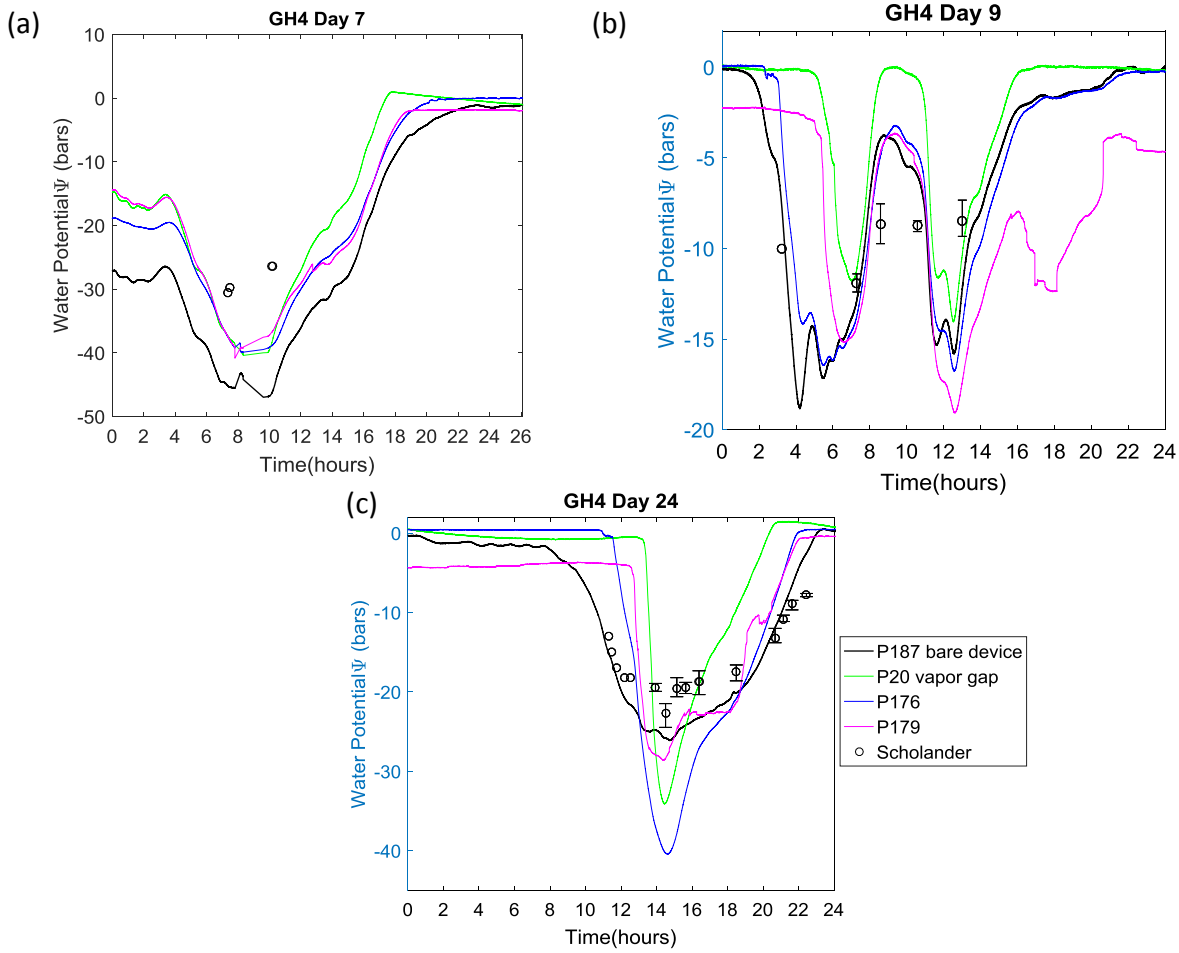

Figure IV-4 Comparison between Scholander Chamber and the Micro-Tensiometer

The black line represents P187. The green line represents P20. The blue line represents P176. The magenta line represents P179. The line colors are the same for all three subplots.
(a) Day 7(a sunny day), the Scholander data were measured before rewatering.
(b) Day 9 (a rainy day), two days after rewatering for the first drought period.
(c) Day 24 (a sunny day), two days after the rewatering for the second drought period on a sunny day.
imposed drought, the sensors and tissue were separated by a larger vapor gap, and resulted in larger vapor psychrometric effect discussed above.

Day 9 (Figure IV-4-b) was two days after rewatering for the first drought period, the P20, with ePTFE membrane, showed delayed response when the temperature was increasing, and advanced response when the temperature was dropping. These observations were expected if the P20 was measuring the vapor psychrometric effect across the ePTFE membrane: when the

temperature increases, the sharp decrease in measured water potential was observed. This observation can be explained by the "positive" psychrometric effect. It happens when the sensor has a slightly higher temperature than the tissue. The delayed response could be explained due to the time scale for heat conduction from the outside environment to the sensor. When the temperature decreases at night, the sensor is expected to have a slightly lower temperature than the tissue, the vapor condensates on the PoSi membrane, and results in the sharp increase in measured water potential ("negative" psychrometric effect). P179 delayed its response in a similar way as P20. However, we expected the other sensors (P187, black curve, and P176, blue curve), which responded faster than P20, to measure the real stem water potential. Therefore, we hypothesize that the P179 was not in good contact with the tissue. Since the day 9 was rainy, we expected that the plant did not have a full transpiration. Nevertheless, the plant should still respond to solar intensity and VPD. These expectations could explain varying stem water potential measured during the day. P187 and P176 had the closest correlation with the Scholander pressure chamber, but were usually delayed for about 0.5 to 1 hour. These differences observed for P187 and P176 might be due to the systematic difference between the leaf stem water potential measured by the pressure chamber and the trunk stem water potential measured by the μTMs, the vapor psychrometric effect, or the psychrometric effect specifically due to the xylem tissue in direct contact with the sensors; we favor the hypothesis of a psychrometric effect since the sensors were proved to be able to measure the osmotic potential of the sucrose solution within ± 2 bars of accuracy (Figure III-3).

Day 24 (Figure IV-4-c) was on a sunny day without clouds, and was two days after rewatering for the second drought period. P176 started to read large tensions, about 20 bars more negative than the Scholander response; this observation suggests that P176 lost contact with the

plant tissue. P187, on the other hand, showed good correlation with the Scholander resposne, in distinction from all the other sensors. However, when the day was approaching night, P187 returned more quickly toward zero than the Scholander Pressure Chamber. The reason might be the accumulation of osmolites in leaves, which resulted in high osmotic potential.[58] We expected the predawn water potential measured by the Scholander Pressure chamber may be the high osmotic potential discussed. Since the sensors were in direct contact with the tissue, the small molecules dissolved in xylem sap could get into the sensors, resulting in the insensitivity of the sensor to osmotic potential. At night, the osmolites inside the μTM might cause the sensors to read positive pressure due to the opposite direction of diaphragm deflection.

When comparing the behavior of P187 across the three figures in Figure IV-4, the behavior of P187 appeared to improve progressively during the month, when compared with the Scholander pressure chamber. The possible reasons for this improvement in P187 could include: 1) the wound response of the plant resulted in new tissue growing around the sensor, and improved the liquid and thermal contact between the sensor and the tissue; 2) The embolized xylem elements around the sensor recovered from cavitation, and improved the sensor-tissue contact; and using a chisel to open a slit for sensor installation may have caused less damage to the plant than drilling a hole, because the other sensors installed in drilled holes appeared to progressively lose their contact with the tissue. However, it was still worth keeping the sensors inside the plant for a longer time to see how their behavior evolves over longer periods.

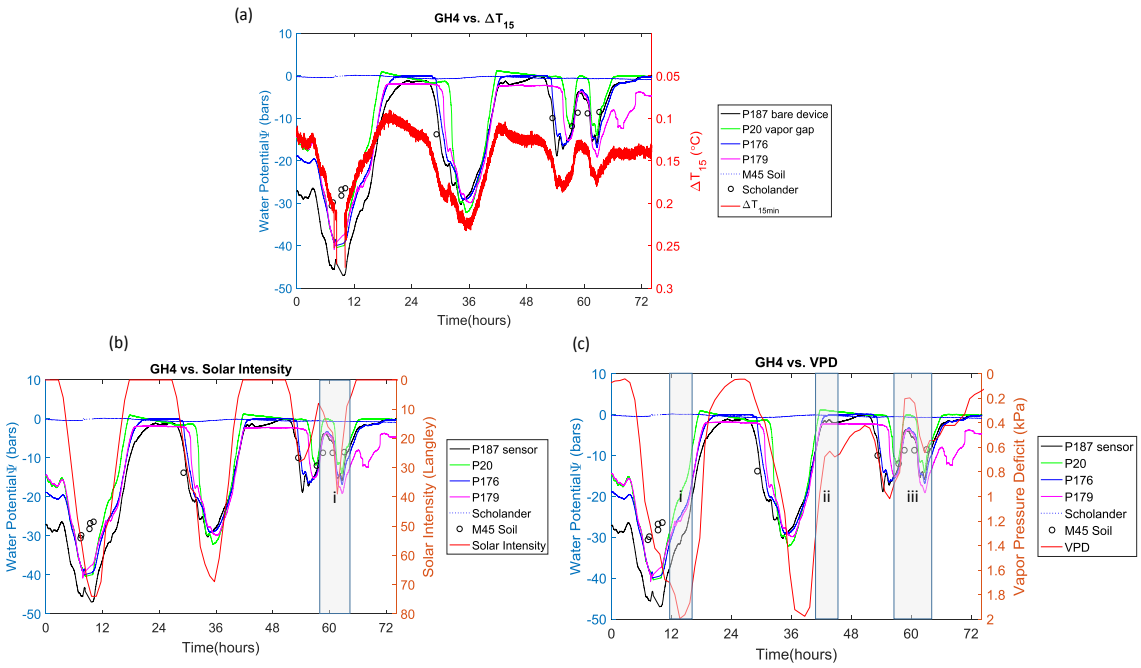

Figure IV-5 Comparison of the μTMs with ΔT(-15min), Solar Radiation and Vapor Pressure Deficit

(a) Comparison of the μTMs with $\Delta T_{-15\,min}$.
(b) the μTMs vs. Solar Radiation
(c) the μTMs vs. VPD

Figure IV-5 shows the dependence of plant water potential on the delayed temperature difference (Figure IV-5-a), solar intensity (Figure IV-5-b) and vapor pressure deficit (VPD) (Figure IV-5-c) on the same rainy day showed in Figure IV-4-b. We selected this rainy day because the VPD and solar intensity varied more significantly than on a normal sunny day, and was helpful for the observation of the sensor response. It is worth noting that $\Delta T_{-15\,min}$, VPD, solar intensity, and water potential measured by the sensors varied in a similar manner. It is hard to determine which one of the three major factors dominate on the variations of water potential.

Figure IV-5-a compared the sensor response to the "temperature difference", the 15min temperature difference estimation ($\Delta T_{-15\,min}$) mentioned above. The temperature data were calculated from P176, due to its position in the center of the sensors installed on the tree.

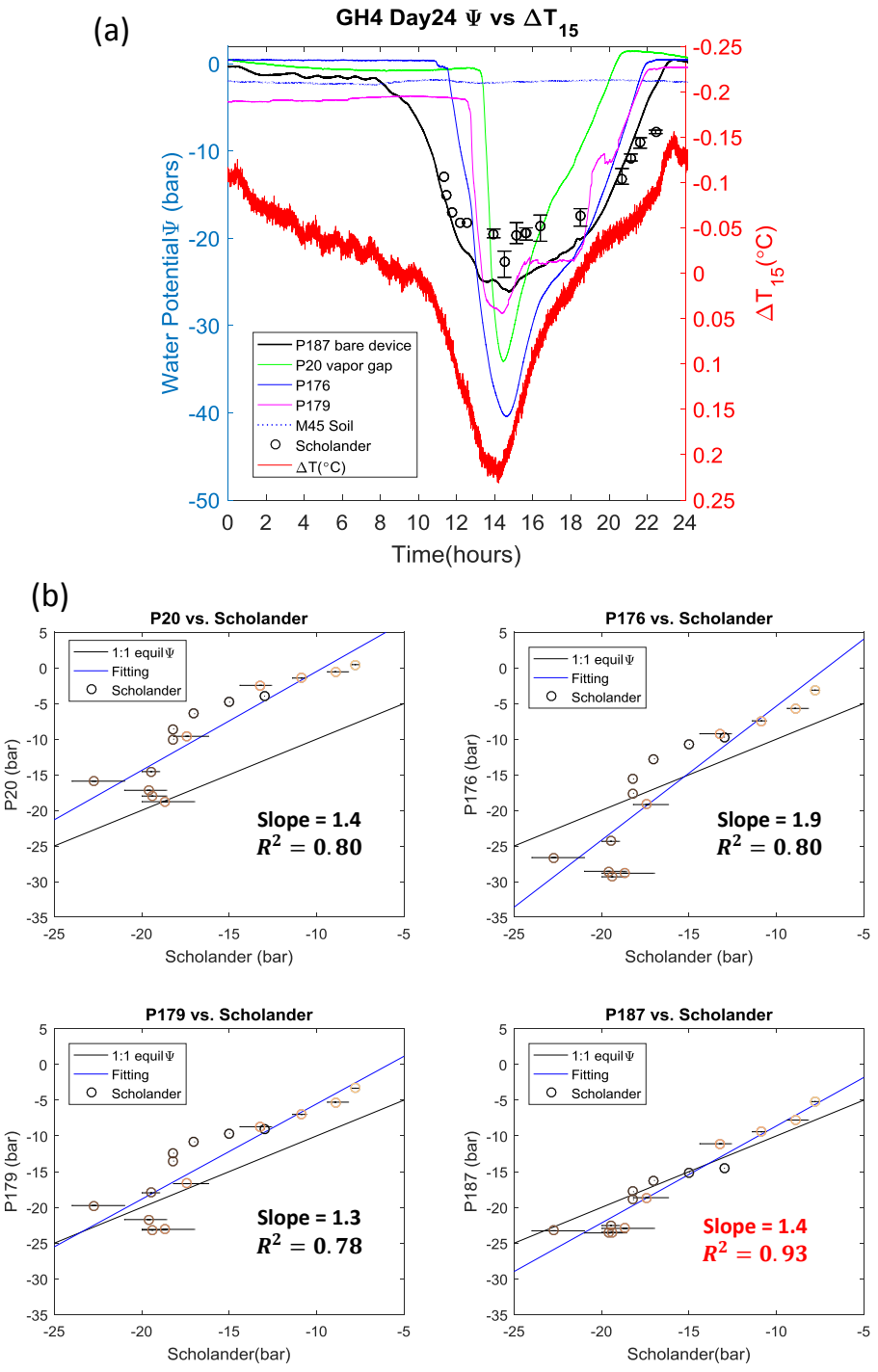

Figure IV-6 Linear comparison between the Scholander data and the sensors.

(a) Chronological Record on Day 24 with $\Delta T_{-15\,min}$;
(b) µTMs vs. Scholander Pressure Chamber. The sensor data were plotted against the Scholander data. The slopes and the quality of the correlation were shown for each sensor.

The sensor still showed a strong correlation with $\Delta T_{-15\,min}$, as in the GH2 results. This observation suggests that a psychrometric effect may have affected these measurements as well.

Figure IV-5-b compares µTMs' response to solar intensity. The sensors had a better correspondence on the variations of solar intensity than the Scholander pressure chamber. In particular, in the region labelled by "i", we see a midday drop in the response of the sensors as the solar intensity dropped. We note though that $\Delta T_{-15\,min}$ also dropped during this period.

Figure IV-5-c shows the µTMs' relationship to VPD. The VPD data were calculated based on the relative humidity and the temperature data from the Cornell Orchard Weather Station by assuming near-saturation vapor pressure inside the leaves. The labelled regions (i, ii and iii) in the plots showed that the midday water potential correlated better with the intensity of solar radiation, while the variations of the midday water potential correlated with VPD. For example, circle (ii) in Figure IV-5-c shows a correlation between the response of P187 and the VPD variation.

Figure IV-6-a compares the responses of the tensiometers to the delayed temperature difference (ΔT)on day 24 when numerous bomb measurements were performed. The responses from P20, P176 and P179 were similar, and may follow on the temperature difference, while P187 had a similar trend as the Scholander pressure chamber data, even though the values were not exactly matched. P20 read close to zero when the Scholander measured -10 to -15 bars of water potential. The Scholander responses reached plateau while the P20 kept reading more and more negative water potential. Both P176 and P179 had similar response as P20, but not as extreme. Therefore, we expected a linear regression if plot P187 against the Scholander data.

Figure IV-6-b presents the correlation between the µTMs and the Scholander pressure chamber on day 24. The sensor responses of the four µTMs was plotted against the Scholander

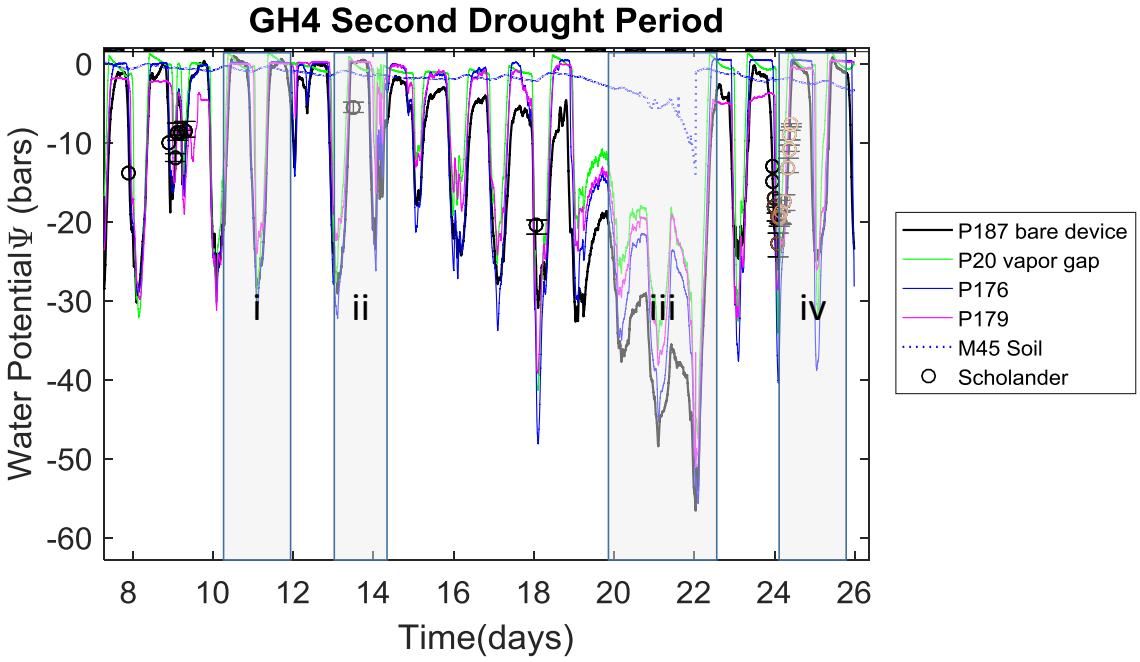

Figure IV-7 GH4--Second Drought Period

The sensors were labeled in the same color as in previous plots.

data. P187 had an almost linear correspondence with the Scholander data, and the best fitting quality ($R^2 = 0.93$), compared to $R^2 \sim 0.80$ of the other sensors.

Figure IV-7 showed the complete data over the second drought period. The soil and stem water potential during a drought period was theoretically sketched in Figure II-3-a [16], and was tested experimentally by Gardner and Nieman in 1964 using a pepper plant (Figure II-3-b). Compared to the literature, the data from my experiment indicated close soil and stem water potential at night when the soil was not under stress. During the drought period, the soil water potential was much less negative than the stem water potential at night, while the literature showed almost identical soil and leaf (stem) water potential when the pepper plant was under tension. The possible reasons were that the soil sensors were not installed deep enough to read the soil sample in direct contact with the roots. Another possibility was that the pathway from the soil to the sensor generated high hydraulic resistance during drought period [59]. The high

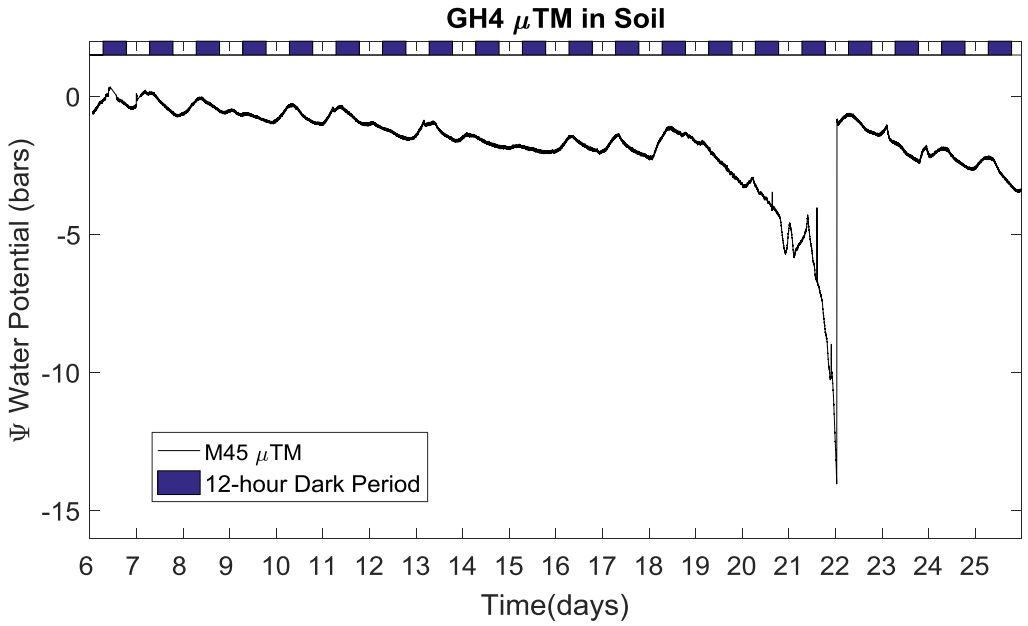

Figure IV-8 The Micro-Tensiometer in Soil

resistance could be in the soil, the soil-root interface, or anywhere in the xylem upstream of the sensor. The generation of high hydraulic resistance requires further investigation. In addition, the root system of apples has very low density and are inconsistent in distribution.[60] Therefore, the soil sensors may not have measured the soil water potential that is effective for the apple tree. The predawn Scholander pressure chamber measured a -5 bar water potential in region (ii), which was much more negative than the sensor data. Comparing regions (i) and (iv) for well-watered conditions, we note that the offset change of the sensors was not significant after 12 days. This observation tends to support our decision to shift the sensor data to zero these pre-dawn responses.

Figure IV-8 shows the μTM measurements in the soil. The μTM reported diurnal variations of the soil water potential. However, we cannot completely exclude the temperature effects on the diurnal variations. These temperature effects include both the psychrometric effect and the temperature effect on the sensor signaling. Additionally, the μTM showed a -14 bar

negative water potential at the end of the second drought period (day 22). This tension was shown relaxed after the second rewatering on day 22.

Combining the above results, the water potential measured by the μTM showed strong dependence on the "temperature difference", solar intensity and VPD. It has also been shown that, several weeks after embedding, the P187 had linear correlation with the Scholander pressure chamber. These observations led to the hypothesis that the sensor P187 was measuring real tissue water potential. Further studies need to be done to test this hypothesis.

The P187, which was the bare device and should have had the best contact with the plant tissue, showed a linear correlation with the Scholander data after being embedded for almost one month inside an apple tree. P20 had an ePTFE membrane between the plant tissue and the sensor. Therefore, P20 has known vapor gap and works as an indicator for the psychrometric effect. If a μTM behaved in a similar way as the P20, it suggests it has lost contact with the tissue.

The results of GH4 give us preliminary evidence that the packaging strategy of P187 worked better than other packaging strategies. Nevertheless, some observations were still able to guide us to further studies and hypotheses. Considering the sensors were placed at different heights on the tree, a gradient of water potential in the direction from lower positioned sensor to the higher positioned sensor was expected (Figure IV-7-iii). However, no direction observation of this gradient existed based on our current data. Therefore, a hypothesis is that the radial water potential gradient dominates when the water stress level is low, due to the small difference in drilled depth for the sensors. Previous studies have shown radial and axial water potential gradient through a sap flow meter and measured radial hydraulic resistance in a cut wood stem in laboratory[9], but no direct measurements have been reported that tested for its existence.

V. FUTURE WORK

V.A. The Radial and Axial Water Potential Gradient in a Stem

As discussed in Section IV.B, one hypothesis is that differences between the μTM readings and the bomb results from a radial gradient of tissue water potential within the stem. To test this hypothesis, we will choose a healthy apple tree in the Cornell Orchard with 7 cm diameter (expecting 5 mm to 20 mm of active xylem).

Figure V-1-a presents the experiment set-up for the above hypothesis. Six sensors will be divided into two groups. These two groups will be separated by 30 cm to 40 cm from each other axially. For each group, three 1.5 mm x 3 mm diaphragm size μTMs will be installed at three different depths (5 mm, 10 mm and 15 mm). For each axial position, an additional sensor with ePTFE membrane will be installed at 5 mm depth to indicate vapor psychrometric effect, but was not shown in Figure V-1-a. This diaphragm size balances the high sensitivity and short response time among all three types of sensors, as shown in Table III-1. All sensors used will be packaged in the same way as P187, which means they will have wire-bonds protected and external wiring protection from external mechanical stress and corrosion. Identical sensors with similar characteristics will allow for easier comparison. All sensors will be installed at least 1 m above the soil. This distance from the ground minimizes temperature effects from the ground. The sensors will not be installed near branches due to their complex xylem structure in these regions. After installation, thermal insulation and reflective insulation will be added, as done in the greenhouse experiments.

Two 1.5 x 3 sensors will be installed deeply (about 50 cm) into the soil. This depth will help prevent the temperature variations in the air from affecting the soil water potential measurements, and help us get a near-root soil water potential as well.

The Scholander pressure chamber will still be used as the benchmark of the μTM testing. The stem water potential will be measured in the same method as described in Section III.B.2.ii. One pyranometer will be positioned 4 m above the canopy of the tree to monitor the solar intensity. The VPD data will be obtained from the Cornell Orchard Weather Station. We will also add a relative humidity meter next to the tree for higher time-resolution monitoring.

Additionally, we will use a CIRUS-3 to measure the photosynthetic rate of the tree through gas exchange analysis.

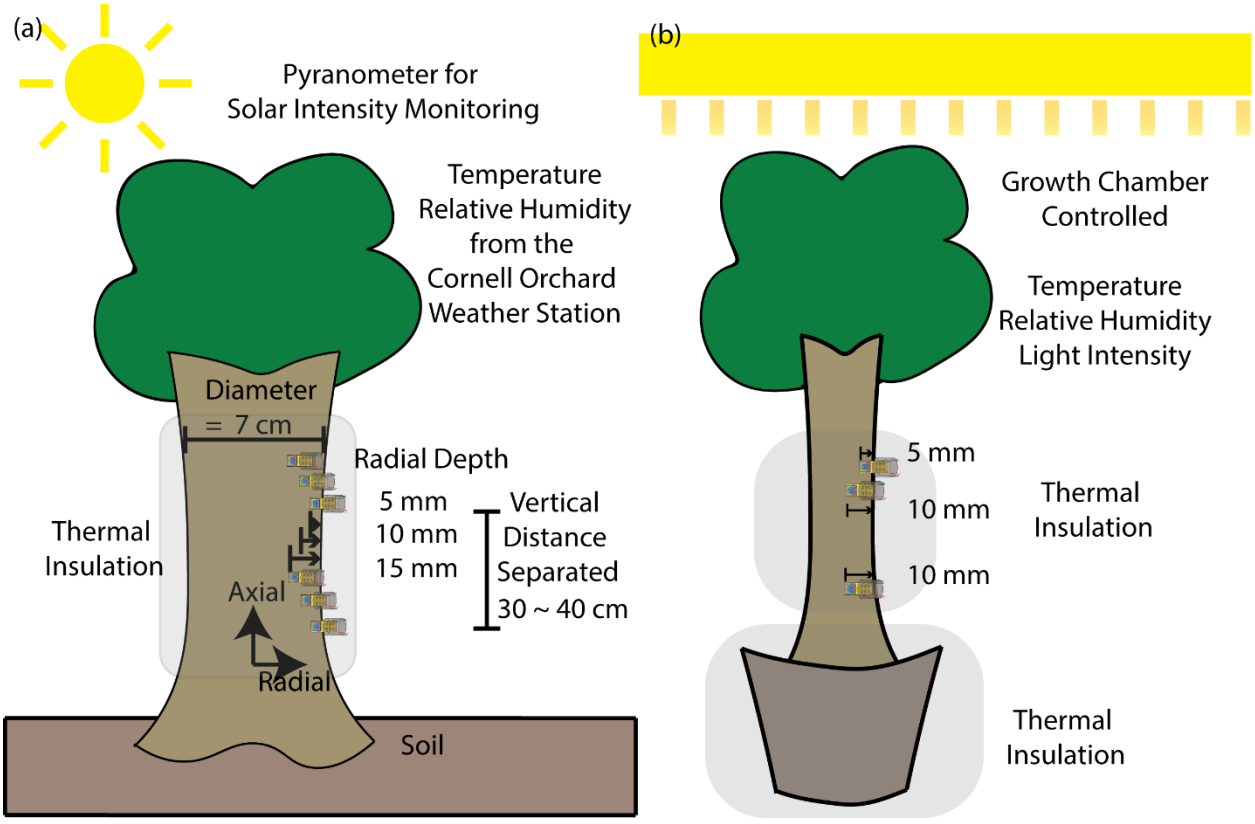

Figure V-1 Orchard and Growth Chamber Experiment Set-up Plan

(a) The Schematic Diagram of the Orchard Experiment Plan for Radial and Axial Water Potential Gradient Testing. The sensors will be inserted into different radial depths and axial heights. The solar intensity will be monitored using a pyranometer. The soil sensors are not shown here.
(b) The Schematic Diagram of the Growth Chamber Plan for the study of vapor and tissue psychrometric effect, as well as the relationship between the stem water potential and the rate of transpiration. The soil sensors are not shown here.

We expect that all sensors will respond linearly with the Scholander pressure chamber, as shown for P187-μTM in Figure IV-6. For radial water potential, the expected result is a positive water potential gradient from outer xylem to inner xylem, which means outer xylem has more negative water potential than the inner part. Vertically, the sensors at a lower position should sense less negative water potential than the higher positioned sensors. When it comes to the rate of transpiration, a linear correlation is expected between the stem water potential and the rate of transpiration. We also expect the transpiration rate to be proportional to the solar intensity and the VPD.

V.B. Vapor and Tissue Psychrometric Effects Testing and the Study on Stomata Regulation

Stomata opening and closing controls the rate of transpiration at a given VPD and solar intensity. With the high time-resolution μTM, the factors affecting the stomata regulation could be studied. A growth chamber will be used to monitor the factors that affect the rate of transpiration accurately. Two healthy apple trees with 3 to 4 cm in diameter will be used for this experiment. Two sensors with the same diaphragm sizes (1.5 mm x 3 mm) will be installed into each tree at 5-mm-deep and 10-mm-deep, separated by less than 10 cm, and at least 1 m above the soil. The third sensor will be installed right above the soil with 10-mm-deep. The sensors will be insulated with the standard method. The Scholander pressure chamber will be used to check whether the sensors have good thermal and tissue contact with the plant. Four factors will be controlled and monitored during the experiment: light intensity, relative humidity, temperature of the growth chamber, and the soil water content. Only one factor will be varied each time to test the correlation between the stem water potential and the varied factor and the response time of the plant. The light will be turned on and off diurnally for the normal growth of the plants, except

when the light intensity is the variable. One μTM (1.5 mm x 3 mm) will be installed inside the soil for each plant for soil water potential monitoring.

The light intensity will first be varied by turning it on and off for two hour intervals alternatively, and then varied in a step change way, while keep the other factors constant and the soil saturated. The response of the plants will be monitored through the μTMs. The expected response is that the stem water potential decreases (more negative) when the light is on, and increases back to soil water potential when the light is off. The correlation between the step-change light intensity and the stem water potential should be linear.

To prevent possible vapor psychrometric effects on the sensors, the temperature will be kept constant while changing the relative humidity inside the growth chamber. The increased VPD will drive the evaporation from leaves to the atmosphere and generate more negative water potential. A linear regression between the VPD and the sensor reading is also expected.

The effects of soil water potential effects on the stomata regulation will be tested by controlling constant VPD and light intensity diurnally in the growth chamber while drying the soil progressively. Since the light intensity will be kept constant during the day, the change in the stem water potential due to the stomata opening and closing will be easily identified. After several days of drying, the soil will be re-watered and the response of the plants will be monitored.

The psychrometric effect on sensor will be studied by water the soil with 10 ºC water and insulate the soil with appropriate thermal insulation, while maintaining 25 ºC growth chamber temperature. If the increase in water potential happens simultaneously for the three sensors on each tree, it means the lower sap temperature in the xylem results in a psychrometric effect. If the increase in water potential happens non-simultaneously, and the response happens in the

order from 5-cm-deep sensor, 10-cm-deep near root sensor and the 10-cm-deep stem sensor, that means the insulation is nearly ideal and tissue water potential is measured. An apple tree transpires water from the active xylem. Therefore, 5-cm sensor is expected to be the first to experience tissue psychrometric effect, and the 10-cm stem sensor is expected to be the last.

VI. CONCLUSION

The development, installation and the in-plant testing of the second generation μTM were presented in this thesis. The μTM has been shown to be able to measure the plant stem water potential with high time-resolution, and was able to achieve a linear regression with the widely accepted Scholander pressure chamber data when being tested in plants.

The μTM was built based on the MVLE theory by connecting the internal liquid to the outside vapor through a nano-scale porous silicon; this design combined the techniques of MEMS and piezoresistive pressure sensing to transduce the energy signal to mechanical signal, and eventually to electronic signal.

Greenhouse experiment 2 (GH2) was conducted to develop the thermal insulation methods to minimize the thermal noise from the outside environment. From the GH2 results, the sensors showed much more negative water potential than the pressure chamber measurements (about -15 bar). The hypothesis about the existence of the vapor psychrometric effect due to the sensor-tissue vapor gap was proposed (7.77 MPa/°C) and was tested in the GH4 experiment by trying different packaging strategies to improve the sensor-tissue thermal contact.

The GH4 experiment showed one device P187 with linear correlation with the Scholander pressure chamber. This device was a bare device, which has direct thermal contact with the tissue, and was installed with a minimal damage to the plant tissue. The gradual improvement in its measurement might be due to the growing of the wound tissue, or the reconnecting of the cavitated xylem elements around the sensor. The GH4 also showed strong stem water potential dependence on solar intensity and vapor pressure deficit (VPD). Based on the GH4 results, a new hypothesis about the axial and radial gradient of stem water potential will be tested in next step experiments.

The radial and axial stem water potential will be tested by inserting μTMs at different depths of the stem to test whether there is a gradient of water potential exist. The psychrometric effect and the stem water potential dependence on VPD and solar intensity will be further studied in growth chamber experiments. Further work will be done to generate a well-developed sensor application strategy for both research and commercial applications.

Current results proved that a μTM could be used to monitor water potential in real-time with high accuracy. The μTMs can be integrated into water monitoring systems of agriculture to improve water use efficiency and water use productivity. They can also be used to conduct plant drought response studies, and to screen for drought tolerant phenotypes of genetic modified plants. Furthermore, monitoring the water stress using the μTMs in forests can help predict the global climate change.

VII. REFERENCES

1. Hatfield JL, Boote KJ, Kimball BA, et al. Climate impacts on agriculture: Implications for crop production. *Agron J*. 2011;103(2):351-370. doi:10.2134/agronj2010.0303.
2. NCA 2014. http://nca2014.globalchange.gov/highlights/report-findings/water-supply#intro-section-2.
3. D. Schaible G, P. Aillery M. Water Conservation in Irrigated Agriculture: Trends and Challenges in the Face of Emerging Demands. *Econ Res Serv*. 2012;(99):1-60. http://www.ers.usda.gov/media/884158/eib99.pdf.
4. Roderick ML, Rotstayn LD, Farquhar GD, Hobbins MT. On the attribution of changing pan evaporation. *Geophys Res Lett*. 2007;34(17):1-6. doi:10.1029/2007GL031166.
5. Chaves M, Davies B. Drought effects and water use efficiency: Improving crop production in dry environments. Functional Plant Biology. doi:10.1071/FPv37n2_FO.
6. Richards RA, Rebetzke GJ, Watt M, Condon AG, Spielmeyer W, Dolferus R. Breeding for improved water productivity in temperate cereals: Phenotyping, quantitative trait loci, markers and the selection environment. *Funct Plant Biol*. 2010;37(2):85-97. doi:10.1071/FP09219.
7. Wheeler JK, Huggett B a., Tofte AN, Rockwell FE, Holbrook NM. Cutting xylem under tension or supersaturated with gas can generate PLC and the appearance of rapid recovery from embolism. *Plant, Cell Environ*. 2013;36(11):1938-1949. doi:10.1111/pce.12139.
8. van den Honert TH. Water transport in plants as a catenary process. *Discuss Faraday Soc*. 1948;3(146):146. doi:10.1039/df9480300146.
9. Domec J-C, Meinzer FC, Gartner BL, Woodruff D. Transpiration-induced axial and radial tension gradients in trunks of Douglas-fir trees. *Tree Physiol*. 2006;26(3):275-284.

doi:10.1093/treephys/26.3.275.

10. Gollan, T. & Turner NC. The responses of stomata and leaf gas exchange to vapor pressure deficits and soil water content. 1985:356-362.

11. Turner NC. Further progress in crop water relations. *Adv Agron*. 1997;58(JANUARY 1996):293-338. doi:10.1016/S0065-2113(08)60258-8.

12. Scholander PF, Bradstreet ED, Hemmingsen E a, Hammel HT. Sap Pressure in Vascular Plants: Negative hydrostatic pressure can be measured in plants. *Science*. 1965;148(3668):339-346. doi:10.1126/science.148.3668.339.

13. Vincent O, Sessoms D a., Huber EJ, Guioth J, Stroock AD. Drying by Cavitation and Poroelastic Relaxations in Porous Media with Macroscopic Pores Connected by Nanoscale Throats. *Phys Rev Lett*. 2014;113(13):1-5. doi:10.1103/PhysRevLett.113.134501.

14. Caupin F, Stroock A. The Stability Limit and other Open Questions on Water at Negative Pressure. *Adv Chem Physics, Liq …*. 2013;152:51-80. http://books.google.com/books?hl=en&lr=&id=wRMm0eN3F8gC&oi=fnd&pg=PA51&dq=THE+STABILITY+LIMIT+AND+OTHER+OPEN+QUESTIONS+ON+WATER+AT+NEGATIVE+PRESSURE&ots=vO544o0hk6&sig=_5jONcJ9C-CgLrJoVv6LKCU0vg0.

15. Pagay V, Santiago M, Sessoms D a, et al. A microtensiometer capable of measuring water potentials below -10 MPa. *Lab Chip*. 2014;14(15):2806-2817. doi:10.1039/c4lc00342j.

16. Slatyer RO. *Plant-Water-Relationships*.; 1967.

17. Cowan IR. Transport of water in the soil-plant-atmosphere continuum. *J Appl Ecol*. 1965;2(1):221-239.

18. Taiz L, Zeiger E. *Plant Physiology*.; 2002. http://pdf115.nikubooks.com/plant-physiology-

fifth-edition-PDF-341715.pdf.

19. Fares A, Alva AK. Soil Water Components Based on Capacitance Probes in a Sandy Soil. *Soil Sci Soc Am J*. 2000;64(1):311. doi:10.2136/sssaj2000.641311x.

20. Flory PJ, Krigbaum WR. Thermodynamics of High Polymer Solutions. *Annu Rev Phys Chem*. 1951;2(1):383-402. doi:10.1146/annurev.pc.02.100151.002123.

21. Hinsinger P, Bengough AG, Vetterlein D, Young IM. Rhizosphere: Biophysics, biogeochemistry and ecological relevance. *Plant Soil*. 2009;321(1-2):117-152. doi:10.1007/s11104-008-9885-9.

22. H.H. D. *Transpiration and the Ascent of Sap in Plants*.; 1914.

23. Wheeler TD, Stroock AD. Stability limit of liquid water in metastable equilibrium with subsaturated vapors. *Langmuir*. 2009;25(13):7609-7622. doi:10.1021/la9002725.

24. Stroock AD, Pagay V V., Zwieniecki M a., Michele Holbrook N. The Physicochemical Hydrodynamics of Vascular Plants. *Annu Rev Fluid Mech*. 2014;46(1):615-642. doi:10.1146/annurev-fluid-010313-141411.

25. Rockwell FE, Holbrook NM, Stroock AD. The competition between liquid and vapor transport in transpiring leaves. *Plant Physiol*. 2014;164(4):1741-1758. doi:10.1104/pp.114.236323.

26. Slatyer RO, Taylor SA. Plant- and Soil-water realtions. *Nature*. 1960;187:1048-1049. doi:10.1038/187922a0.

27. Jones HG, Lakso AN, York N, Syvertsen JP, Alfred L. *Physiological Control of Water Status in Temperate and Subtropical Fruit Trees*.; 1985.

28. T.N. B. The control of stomata by water balance. *Tansley Rev*. 2005.

29. Naor a. Midday Stem Water Potential As a Plant Water Stress Indicator for Irrigation

Scheduling in Fruit Trees. *Methods*. 2000;537:447-454. http://www.actahort.org/books/537/537_52.htm.

30. Shock CC, Wang FX. Soil water tension, a powerful measurement for productivity and stewardship. *HortScience*. 2011;46(2):178-185.
31. Klute.A CDK&. Water Potential: Tensiometry. *Am Soc Agron*. 1986.
32. ICT. http://au.ictinternational.com/. Accessed July 30, 2015.
33. Bouyoucos, G.J., & Mick AH. An electrical resistance method for the continuous measurement of soil moisture under field conditions. *Tech Bull Michigan Agric Exp Stn*. 1940.
34. Delta-t. http://www.delta-t.co.uk/product-display.asp?id=SWT-4 Product&div=Soil Science. Accessed August 3, 2015.
35. SoilMoisture Pressure Chamber. http://www.soilmoisture.com/search.php?mode=search&page=1.
36. Decagon. http://www.decagon.com/. Accessed July 30, 2015.
37. Stenitzer.E. Monitoring soil moisture regimes of field crops with gypsum blocks. *Theor Appl Climatol*. 1993;48(2):159-165.
38. Delta-T. http://www.delta-t.co.uk/.
39. Richards SJ, Marsh AW. Irrigation based on soil suction measurements. *Soil Sci Soc Am Proc*. 1961;25(1):65-69.
40. Peck AJ, Rabbidge RM. Design and Performance of an Osmotic Tensiometer for Measuring Capillary Potential. *Soil Sci Soc Am J*. 1969;33(2):196-202.
41. Van Der Ploeg MJ, Gooren HPA, Bakker G, et al. Polymer tensiometers with ceramic cones: Direct observations of matric pressures in drying soils. *Hydrol Earth Syst Sci*.

2010;14(10):1787-1799. doi:10.5194/hess-14-1787-2010.

42. Guan Y, Fredlund DG. Use of the tensile strength of water for the direct measurement of high soil suction. *Can Geotech J*. 1997;34(4):604-614. doi:10.1139/t97-014.

43. Wheeler TD, Stroock AD. The transpiration of water at negative pressures in a synthetic tree. *Nature*. 2008;455(7210):208-212. doi:10.1038/nature07226.

44. Kon S, Oldham KR, Horowitz R. Piezoresistive and piezoelectric MEMS strain sensors for vibration detection. *SPIE_International Soc Opt Eng*. 2007;6529:65292V - 65292V - 11. doi:10.1117/12.715814.

45. Smith CS. Piezoresistance effect in germanium and silicon. *Phys Rev*. 1954;94(1):42-49. doi:10.1103/PhysRev.94.42.

46. Kaajakari V. MEMS Tutorial: Pull-In Voltage in Electrostatic Microactuators. *Pract MEMS*. 2009;(5):1-2.

47. Mosser V, Suski J, Goss J, Obermeier E. Piezoresistive pressure sensors based on polycrystalline silicon. *Sensors Actuators A Phys*. 1991;28(2):113-132. doi:10.1016/0924-4247(91)85020-O.

48. Franssila S. *Introduction to Microfabrication*.; 2010. doi:10.1002/9781119990413.

49. Timoshenko, S. P., & Woinowsky-Krieger S(. *Theory of Plates and Shells*. McGraw-hill; 1959.

50. Kovacs A, Meister D, Mescheder U. Investigation of humidity adsorption in porous silicon layers. *Phys Status Solidi Appl Mater Sci*. 2009;206(6):1343-1347. doi:10.1002/pssa.200881106.

51. Masoodi, R., & Pillai KM. *Wicking in Porous Materials: Traditional and Modern Modeling Approaches*. CRC Press; 2012.

52. Debenedetti PG. *Metastable Liquids Concepts and Principles*.; 1996. doi:10.1088/0953-8984/15/1/308.

53. I-Tzu Chen, David Sessoms, Zachary Sherman, Eugene Choi OV and AS. Stability limit of water by metastable liquid-vapor equilibrium with nanoporous silicon membranes. *Prep*. 2015.

54. Vincent O, Marmottant P, Gonzalez-Avila SR, Ando K, Ohl C-D. The fast dynamics of cavitation bubbles within water confined in elastic solids. *Soft Matter*. 2014;10(10):1455. doi:10.1039/c3sm52697f.

55. Taylor RL, Govindjee S. Solution of clamped rectangular plate problems. *Commun Numer Methods Eng*. 2004;20(10):757-765. doi:10.1002/cnm.652.

56. Dixon MA, Tyree MT. A new stem hygrometer, corrected for temperature gradients and calibrated against the pressure bomb. *Plant, Cell Environ*. 1984;7(9):693-697. doi:10.1111/1365-3040.ep11572454.

57. LaksoAplRevwChap1994.pdf.

58. Lakso, A. N., & Geyer, A.S.,& Carpenter SG. Seasonal Osmotic Relations in Apple Leaves of Different Ages. *J Amer Soc Hort*. 1984;109(4):544-547.

59. Lo Gullo MA, Nardini A, Salleo S, Tyree MT. Changes in root hydraulic conductance (K(R)) of Olea oleaster seedlings following drought stress and irrigation. *New Phytol*. 1998;140(1):25-31. doi:10.1046/j.1469-8137.1998.00258.x.

60. Lakso AN. Water Relations of Apples. In: *Apples: Botany, Production and Uses*. CAB International; 2003.

61. Fereres E, Soriano MA. Deficit irrigation for reducing agricultural water use. *J Exp Bot*. 2007;58(2):147-159. doi:10.1093/jxb/erl165.

62. Buckingham E. Studies On The Movement of Soil Moisture. *Statew Agric L Use Baseline 2015*. 1907;1. doi:10.1017/CBO9781107415324.004.

63. Gardner WR, Nieman RH. Lower Limit of Water Availability to Plants. *Science (80-).* 1964;143(3613):1460-1462. doi:10.1126/science.143.3613.1460.

64. Pagay V, Santiago M, Sessoms D a, et al. A microtensiometer capable of measuring water potentials below -10 MPa. *Lab Chip*. 2014;14(15):2806-2817. doi:10.1039/c4lc00342j.

VIII. APPENDIX

VIII.A. Masks Designed for Micro-Tensiometer Fabrication

Tensiometer CAD.

Changed 3 masks:

1. Cavity – more conservative vein pattern (pitch = 110 microns), added numbers, removed rulers.
2. Polysilicon – longer & narrower piezoresistors, polysilicon goes under all bridge wires/pads (not PRT wires). R = 2,500 ohm for better fit in current mask.
3. Platinum – changed configuration in piezoresistors to fit longer resistors and improve 'zero'.

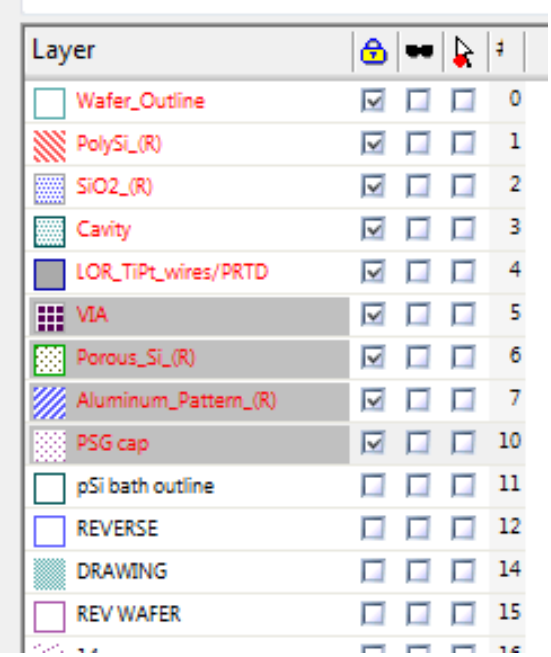

New piezoresistors are longer, sligthly narrower (previous: 20 micron, new: 15 micron), and have lower resistance (R=2,500 ohm)

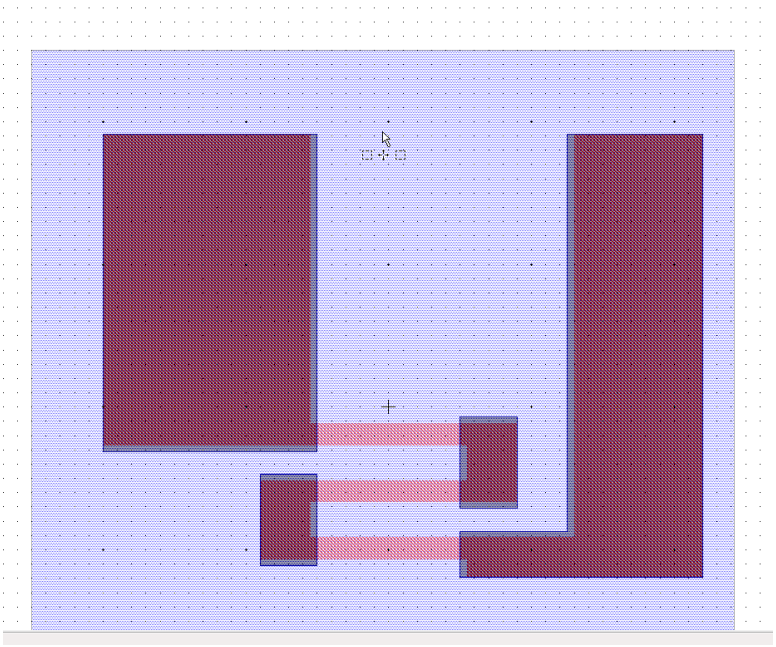

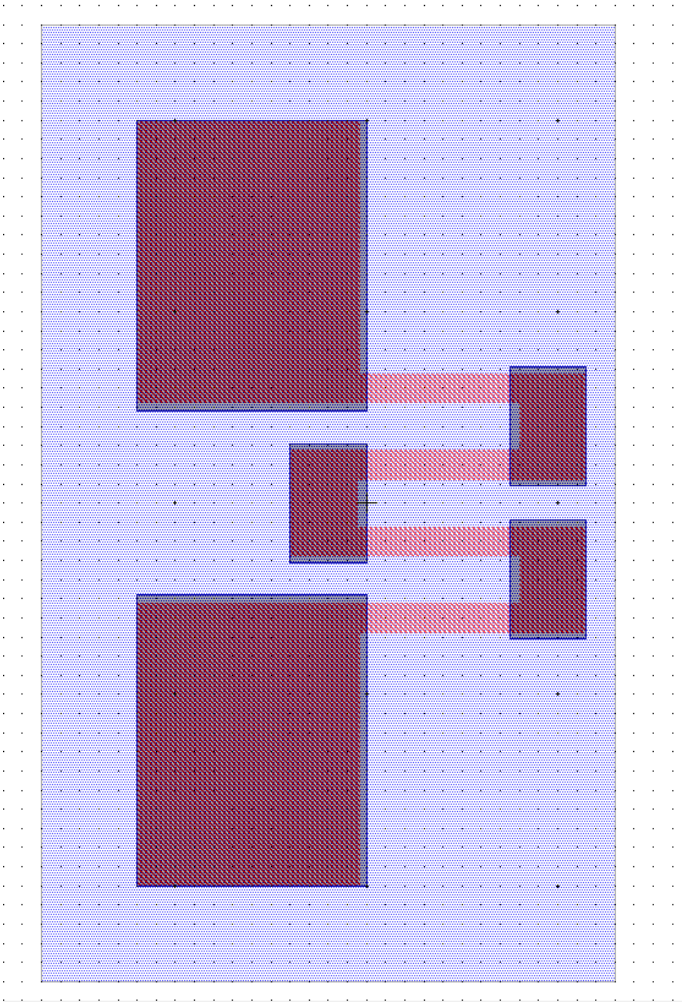

1 mm

Notice polysilicon goes under all bridge-connected metal.

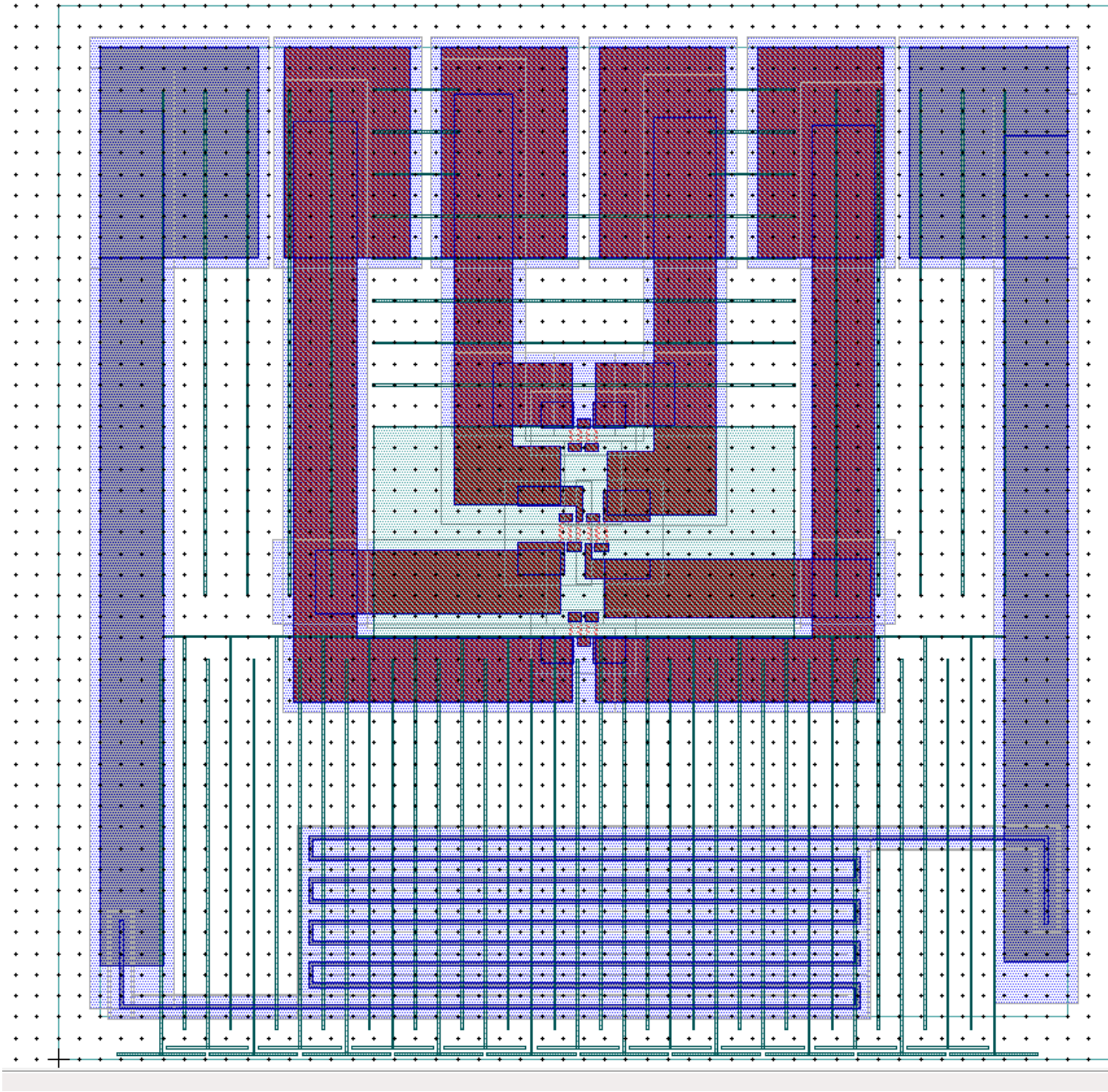

1.5 mm

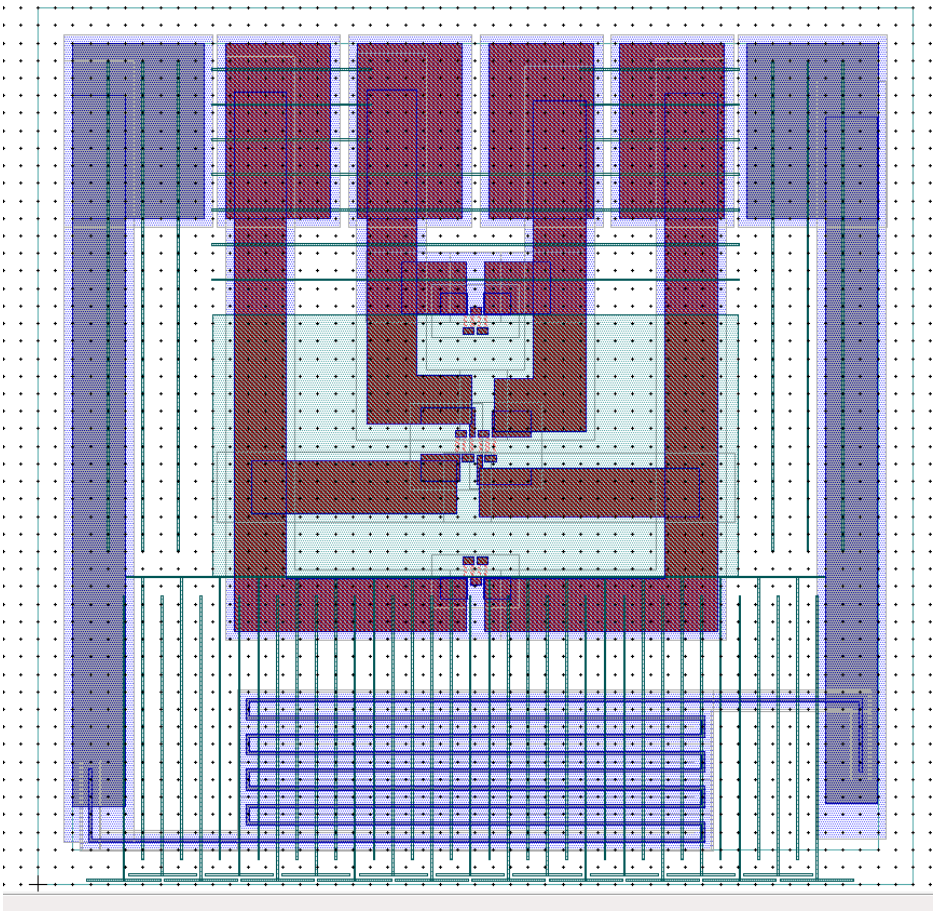

2 mm

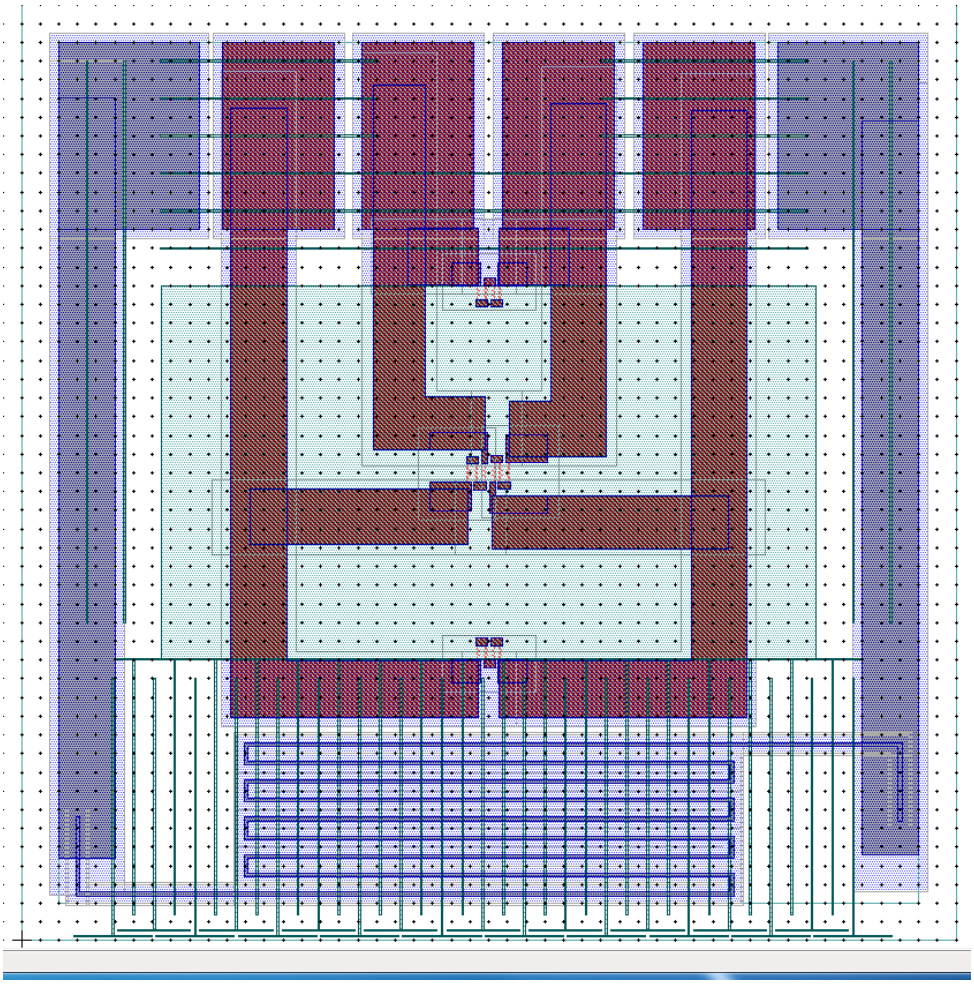

3.5 mm

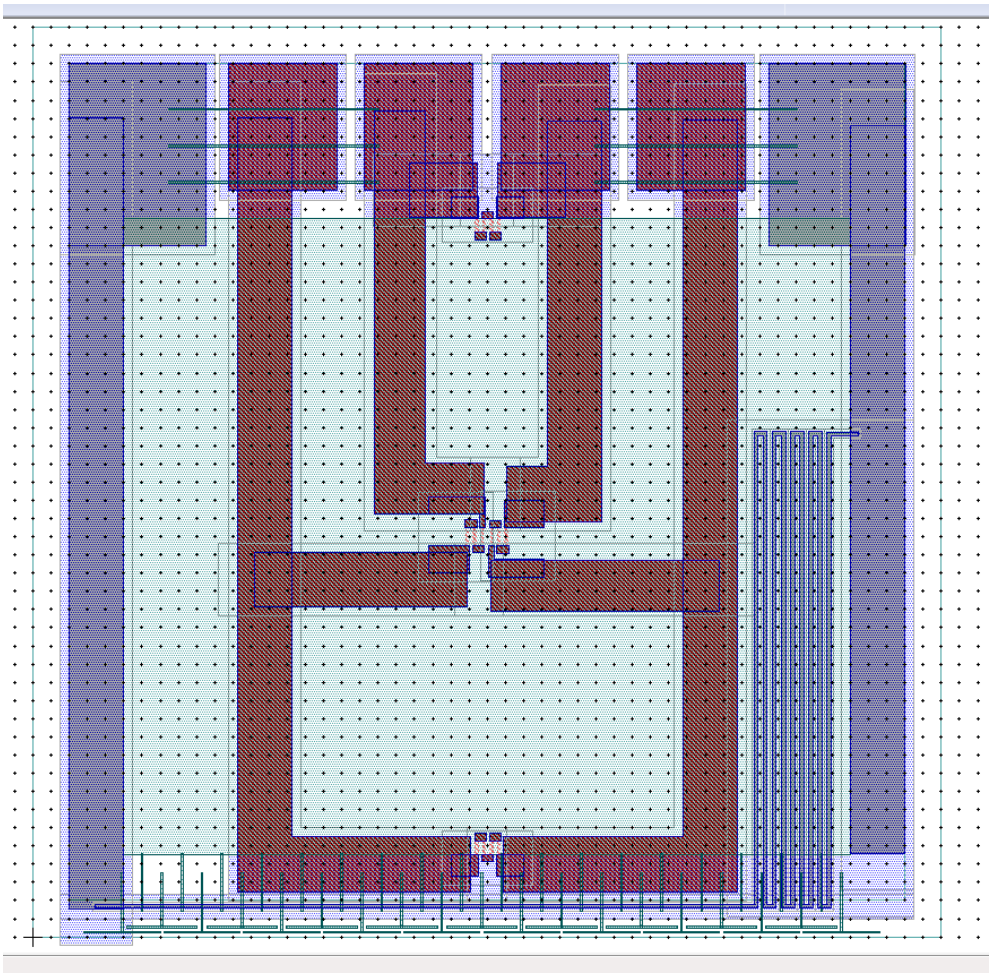

2mm 2WB

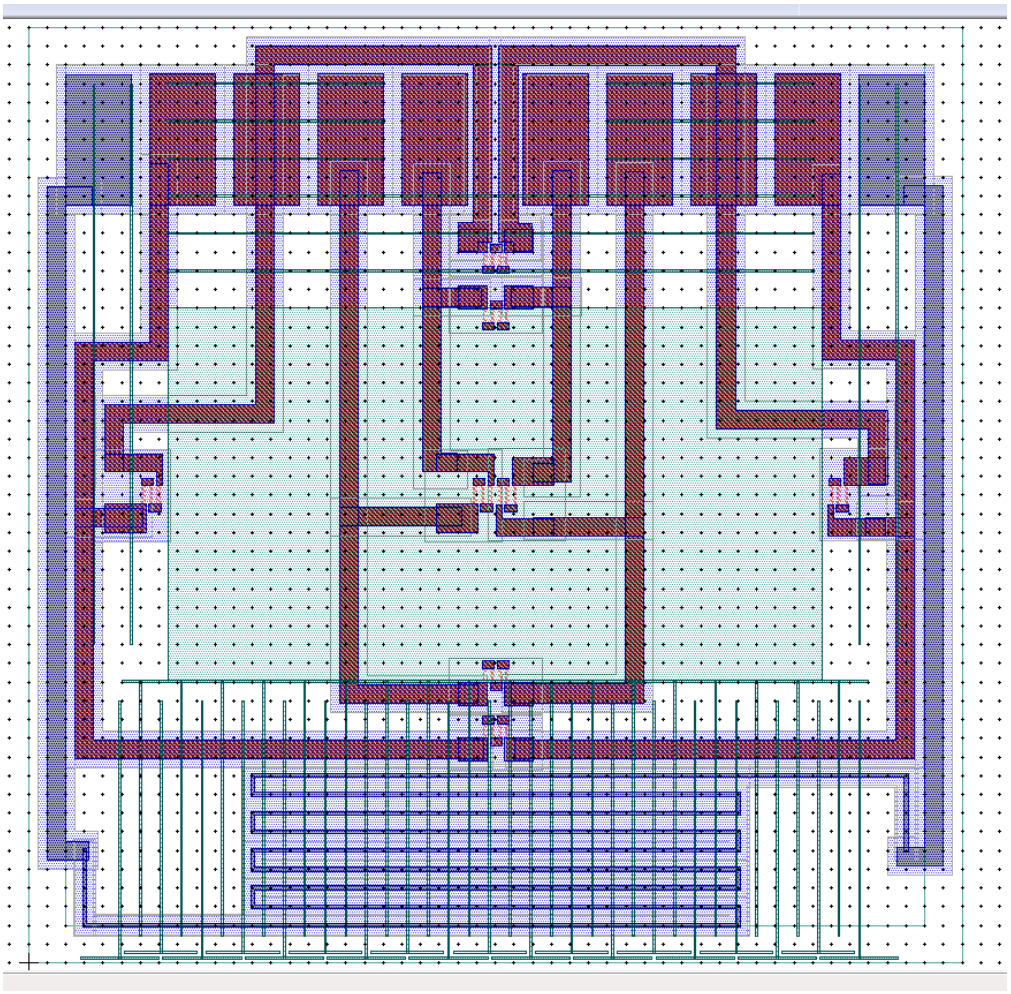

VIII.B. GH2 DATALOGGING PROGRAM

```
'CR6 Series

'Created by Short Cut (3.2)


'Declare Variables and Units

Public BattV

Public PTemp_C

Public SDI12(2)
```

```
Public StemPotential(2)
Public StemTemperature_1
Public StemTemperature_2
Public Mult(2)={13.2908,8.42744}
Public Offs(2)={13.6,-49.53}

Alias SDI12(1)=SoilPotential
Alias SDI12(2)=SoilTemperature

Units BattV=Volts
Units PTemp_C=Deg C
Units StemPotential=bar
Units StemTemperature_1=C
Units StemTemperature_2=C
Units SoilPotential=kPa
Units SoilTemperature=C

'Define Data Tables
DataTable(Table1,True,-1)
    DataInterval(0,30,Sec,10)
    CardOut(0,-1)
    Average(1,StemPotential(1),IEEE4,False)
```

```
        Average(1,StemPotential(2),IEEE4,False)
        Average(1,SoilPotential,IEEE4,False)
        Average(1,SoilTemperature,IEEE4,False)
        Average(1,StemTemperature_1,IEEE4,False)
        Average(1,StemTemperature_2,IEEE4,False)
EndTable

DataTable(Table2,True,-1)
        DataInterval(0,1440,Min,10)
        Minimum(1,BattV,FP2,False,False)
EndTable

'Main Program
BeginProg
        'Main Scan
        Scan(30,Sec,1,0)
                'Default CR6 Datalogger Battery Voltage measurement 'BattV'
                Battery(BattV)
                'Default CR6 Datalogger Wiring Panel Temperature measurement 'PTemp_C'
                PanelTemp(PTemp_C,60)
                'Generic SDI-12 Sensor measurements 'SoilPotential', and 'SoilTemperature'
                SDI12Recorder(SDI12(),C1,"0","M!",1,0)
```

```
        'Reset all Generic SDI-12 Sensor measurements if NaN is returned to SDI12(1)
        If SDI12(1)=NaN Then Move(SDI12(),2,NaN,1)
        'Generic Full Bridge measurements 'StemPotential()'
        BrFull(StemPotential(),2,mV200,U1,U5,2,50,True,True,5000,60,Mult(),Offs())
        'Generic Resistance measurements 'StemTemperature_1'

    Resistance(StemTemperature_1,1,mV200,U7,U6,1,20,True,True,5000,60,0.144456,-
307.852)
        'Generic Resistance measurements 'StemTemperature_2'

    Resistance(StemTemperature_2,1,mV1000,U9,U11,1,20,True,True,5000,60,0.150353,-
316.904)
        'Call Data Tables and Store Data
        CallTable Table1
        CallTable Table2
    NextScan
EndProg
```

VIII.C. GH4 DATALOGGING PROGRAM

```
'CR6 Series
'Created by Short Cut (3.1)
'Date: 05_31_2016
```

```
'Author: Siyu Zhu
'Sensors pipeline + MPS6 sequential

'Declare Variables and Units
Public BattV
Public PTemp_C
Public LCount
Public FullBR(6)
Public Resist(6)
Public Temp_C

Public MPS(2);'MPS6 Decagon Soil Potential Meter
Alias MPS(1) = S_tension
Alias MPS(2) = S_Temp

Public MultB(6) = {0.082784,0.043834,0.123542,0.129638,0.095201,0.0752}; 'm_B corrected
Bridge bomb calibration term
Public OffsB(6) = {-1.200957,0.232887,-0.262945,-0.068569,-1.6273, -0.855};'b_B
Public MultT(6) = {0,4.46813,4.46263,4.49755,0,6.922523};'m_T
Public OffsT(6) = {0,1396.52900,1424.93910,1409.16360,0, 2131.113};'b_T PRT calibration
term
Public MultBT(6) = {0,-0.01861,-0.01828,-0.02197,0,0};'m_BT
```

```
Public OffsBT(6) = {0,-2.83835,-2.21196,1.19877,0,0};'b_BT  temperature effects on bridge



Units BattV=Volts

Units PTemp_C=Deg C

Units FullBR=bar

Units Resist = C

Units Temp_C = Deg C

Units S_tension = kPa

Units S_Temp = C


'Define Data Tables

DataTable(G4_060716,True,-1)

        DataInterval(0,10,Sec,10)

        Average(1,FullBR(1),IEEE4,False)

        Average(1,FullBR(2),IEEE4,False)

        Average(1,FullBR(3),IEEE4,False)

        Average(1,FullBR(4),IEEE4,False)

        Average(1,FullBR(5),IEEE4,False)

        Average(1,FullBR(6),IEEE4,False)


  Average(1,Resist(1),IEEE4,False)
```

```
  Average(1,Resist(2),IEEE4,False)
  Average(1,Resist(3),IEEE4,False)
  Average(1,Resist(4),IEEE4,False)
  Average(1,Resist(5),IEEE4,False)
  Average(1,Resist(6),IEEE4,False)
  Average(1,Temp_C,IEEE4,False)
  Average(1,PTemp_C,FP2,False)
        Minimum(1,BattV,FP2,False,False)
EndTable

DataTable(Soil_060716,1,-1)
  Average(1,S_tension,IEEE4,False)
  Average(1,S_Temp,IEEE4,False)
EndTable

'Main Program
BeginProg
        'Main Scan
        Scan(10,Sec,0,0)
                'Default Datalogger Battery Voltage measurement 'BattV'
                Battery(BattV)
                'Default Wiring Panel Temperature measurement 'PTemp_C'
```

```
        PanelTemp(PTemp_C,60)

        'Measure temperature of sensors
        MuxSelect(U1,U2,5,8,1)
        LCount=1
        SubScan(0,uSec,6)
            'Switch to next AM16/32 Multiplexer channel
            PulsePort(U1,10000)
            'Generic Resistance measurements 'FullBR()' on the AM16/32 Multiplexer

    Resistance(Resist(LCount),1,mV5000,U5,U3,1,200,1,1,10000,60,1/MultT(LCount),-
OffsT(LCount)/MultT(LCount))
            LCount=LCount+1
        NextSubScan
        'Turn AM16/32 Multiplexer Off
        PortSet(U2,0)
        Delay(0,150,mSec)

  'Measure micro-T water potential
        LCount = 1
        PortSet(U2,1)
        Delay(0,150,mSec)
```

```
                LCount = 1
  SubScan(0,uSec,6)
                  PulsePort(U1,10000)
                  Resist(1) = 0
                  Resist(5) = 0

BrFull(FullBR(LCount),1,mV5000,U5,U3,1,500,1,1,10000,60,1/MultB(LCount),-
(MultBT(LCount)*Resist(LCount)+OffsBT(LCount)+OffsB(LCount))/MultB(LCount))
                  LCount = LCount + 1
                NextSubScan
                LCount = 1
                PortSet(U2,0)
                Delay(0,150,mSec)

                TCDiff(Temp_C,1,mv200C,U7,TypeK,PTemp_C,True,0,60,1,0)
                'Call Data Tables and Store Data
                CallTable G4_060716
          NextScan

'Program to scan MPS-6 using sequential mode
  SlowSequence
    Scan(15,Sec,0,0)
```

SW12(1,1)

'Delay for at least 250 mSec for sensor to enter SDI-12 mode

Delay(1,300,mSec)

'Reset Generic SDI-12 sensor measurements'

'Query sensor for 3 SDI-12 outputs. Default address for all Decagon Digital sensors is 0

SDI12Recorder(MPS(),C1,"0","M!",1,0)

SW12(1,0)

Delay(0,250,mSec)

CallTable Soil_060716

NextScan

EndProg

VIII.D. GH4 Data Analysis Program

```
clear
clc
close all
plotoption = 1; % plot temperatures % plotoption = 2; % plot
solar intensity %plotoption = 3; % plot VPD
startT = 11.25; % hour
%uiimport
load('data.mat')
% record number
RN = RECORD(5:end)*10/3600;
RN_PB = RECORD_PB(3:end)*10/3600; % bomb measurement record
number
RN_WS = RECORD_WS(3:end)*10/3600;
RN_Cond = RECORD_Porometer(3:end)*10/3600;
RN_MPS = RECORD_MPS(5:end)*10/3600;
% Radiation
```

```
Rad = RadData(3:end);
% VPD
VPD = VPDData(3:end);
% Conductance
Cond = Conductance(3:end);
% tension
P20 = FullBR_Avg1(5:end);
P176 = FullBR_Avg3(5:end);
P179 = FullBR_Avg4(5:end);
P187 = FullBR_Avg5(5:end);
M45_S = FullBR_Avg6(5:end);
S_tension = -MPS_tension(5:end)/100; % MPS tension
PB = PBData(3:end);
e_up = Error_yup(3:end);
e_down = Error_ydown(3:end);
% temp
P36T = Resist_Avg2(5:end);
P176T = Resist_Avg3(5:end);
P179T = Resist_Avg4(5:end);
M45T_S = Resist_Avg6(5:end);
S_temp = MPS_temp(5:end);% MPS temp
P_temp = PTemp_C_Avg(5:end);
Stem_T = Temp_C_Avg(5:end);
% Match Matrix Size of PB and sensors
PB_out = zeros(size(P187));
PB_out = NaN*PB_out;
VPD_out = PB_out;
Rad_out = PB_out;
e_upout = PB_out;
e_downout = PB_out;
S_out = PB_out;

% T15
P179T_15 = zeros(size(P179T));
pts_15 = 15*60/30;
for i  = 1+pts_15:length(P179T)
    P179T_15(i) = P179T(i)-P179T(i-pts_15);
end

% Error bars for PB data
for i = 1:length(RN)
    for j = 1:length(RN_PB)
    if abs(round(RN_PB(j)*3600/10) - round(RN(i)*3600/10))<= 1
        PB_out(i) = PB(j);
        e_upout(i) = e_up(j);
        e_downout(i) = e_down(j);
    end
```

```
    end
end

% offset correction
c1 = length(RN)-12*24*3600/10;
c2 = length(RN)-16*24*3600/10;
P176_avg = P176;
P176_avg(:) = NaN;
P179_avg = P176_avg;
P20_avg = P176_avg;
P187_avg = P176_avg;
lim = 1e-3;

for i = c2:c1
    if P176(i)< 5 && P176(i)>0 && abs(P176(i+1)-P176(i))<lim &&
abs(P176(i)-P176(i-1))<lim
    P176_avg(i) = P176(i);
    end

    if P179(i)< 0 && P179(i)>-5 && abs(P179(i+1)-P179(i))<lim &&
abs(P179(i)-P179(i-1))<lim
    P179_avg(i) = P179(i);
    end

    if P20(i)< 0 && P179(i)>-5 && abs(P20(i+1)-P20(i))<lim &&
abs(P20(i)-P20(i-1))<lim
    P20_avg(i) = P20(i);
    end

    if P187(i)<0 && P187(i)>-5 && abs(P187(i+1)-P187(i))<lim &&
abs(P187(i)-P187(i-1))<lim
    P187_avg(i) = P187(i);
    end

end


P176_v = mean(P176_avg(~isnan(P176_avg)));
P179_v = mean(P179_avg(~isnan(P179_avg)));
P20_v = mean(P20_avg(~isnan(P20_avg)));
P187_v = mean(P187_avg(~isnan(P187_avg)));

for i = 1:length(RN_Cond)
    Ptemp = P187( (RN > (RN_Cond(i)-30/10)) & (RN <
(RN_Cond(i)+30/10)));
    P187_Cond(i) = mean(Ptemp);
end
```

```
% P176_v = 0;
% P179_v = 0;
% P20_v = 0;
% P187_v = 0;

for i = 1:length(RN_PB)
    Ptemp_1 = P20( (RN > (RN_PB(i)-30/10)) & (RN <
(RN_PB(i)+30/10)));
    Ptemp_2 = P176( (RN > (RN_PB(i)-30/10)) & (RN <
(RN_PB(i)+30/10)));
    Ptemp_3 = P179( (RN > (RN_PB(i)-30/10)) & (RN <
(RN_PB(i)+30/10)));
    Ptemp_4 = P187( (RN > (RN_PB(i)-30/10)) & (RN <
(RN_PB(i)+30/10)));
    P20_out(i) = mean(Ptemp_1)-P20_v;
    P176_out(i) = mean(Ptemp_2)-P176_v;
    P179_out(i) = mean(Ptemp_3)-P179_v;
    P187_out(i)=mean(Ptemp_4)-P187_v;

end

% for i = 1:length(RN)
%     for j = 1:length(RN_WS)
%     if abs((RN_WS(j)*3600/10) - round(RN(i)*3600/10)) < 1.5
%         VPD_out(i) = VPD(j);
%         Rad_out(i) = Rad(j);
%      end
%     end
% end


%%
close all
figure(1)
% a = 1;
% b = length(RN);

a = length(RN)-2.4*24*3600/10;
b = length(RN)-1*24*3600/10;
yyaxis left
plot(RN(a:b),P187(a:b)-P187_v,'-k')
hold on
plot(RN(a:b),P20(a:b)-P20_v,'-g')
plot(RN(a:b),P176(a:b)-P176_v,'-b')
plot(RN(a:b),P179(a:b)-P179_v,'-m')
errorbar(RN(a:b),PB_out(a:b),e_downout(a:b),e_upout(a:b),'ob')
```

```
plot(RN(a:b),M45_S(a:b),':k')
%plot(RN_MPS,S_tension,':b')
xlabel('time(hours)')
ylabel('water potential\Psi (-bar)')
ax = gca;
title('Second Drought Period')
ax.YLim = [-5  60];
ax.XLim =[round(a*10/3600) round(b*10/3600)];
ax.XTick = round(a*10/3600):2:round(b*10/3600);
ax.XTickLabel =
{round((a*10/3600+startT)):2:round((b*10/3600+startT))};
%ax.XTickLabel =
{round((a*10/3600+startT)/24):0.5:round((b*10/3600+startT)/24)};
% T =
round((a*10/3600+startT+0.75)):12:round((b*10/3600+startT+0.75))
;
% H = -4*ones(size(T));
% for i = 1:2:length(H)
%     H(i) = -5;
% end
% bar(T,H,1,'basevalue',-5);
hold off
%legend('P187 sensor','P20','P176','P179','Scholander','M45
Soil','Location','EastOutside')


% yyaxis right
% plot(RN(a:b),P179T_15(a:b),'r')
% ax = gca;
% ax.YLim = [-0.2 0.3];
% ylabel('\Delta Temp 15min (C)')
% title('GH2 vs. \Delta Temp')
% legend('P187 sensor','P20','P176','P179','Scholander','M45
Soil','\Delta T 15min','Location','EastOutside')

yyaxis right
if plotoption == 1
plot(RN(a:b),P36T(a:b),'-r')
hold on
plot(RN(a:b),P176T(a:b),'--r')
plot(RN(a:b),P179T(a:b),':r')
%plot(RN(a:b),M45T_S(a:b),'-.r')

hold off
ax = gca;
ax.YLim = [15 35];
ylabel('Temperature (C)')
```

```
title('GH2')
legend('P187 sensor','P20','P176','P179','Scholander','M45
Soil','P36T','P176T','P179T','Location','EastOutside')
else if plotoption ==2
        plot(RN_WS,Rad,'r')
        ylabel('Solar Intensity (Langley)')
        title('GH2 vs. Solar Intensity')
        legend('P187
sensor','P20','P176','P179','Scholander','M45 Soil','Solar
Intensity','Location','EastOutside')
    else
        plot(RN_WS,VPD,'r')
        ylabel('Vapor Pressure Deficit (kPa)')
        title('GH2 vs. VPD')
        legend('P187
sensor','P20','P176','P179','Scholander','M45
Soil','VPD','Location','EastOutside')
    end
end

%%
clc
close all
m = 14;
n = 28;
fitvalues = zeros(4,2);
rsq = zeros(4,1);
figure(2)
title('GH2 \Mu TM vs.Scholander Pressure Chamber')

subplot(2,2,1)
f1 = fit(P20_out(m:n)',PB(m:n),'poly1');
plot([-5 35],[-5 35],'k')
hold on
plot(f1,'b')
errorbar(P20_out(m:n),PB(m:n),e_down(m:n),e_up(m:n),'ob')
hold off
ax = gca;
ax.XLim = [-5 35];
ax.YLim = [5 25];
xlabel('P20 (-bar)')
ylabel('Scholander Pressure Chamber (-bar)')
title('P20 vs. Scholander')
fitvalues(1,:) = coeffvalues(f1);
yfit = polyval(fitvalues(1,:),P20_out(m:n)');
yresid = PB(m:n)-yfit;
SSresid = sum(yresid.^2);
```

```
SStotal = (length(PB(m:n))-1)*var(PB(m:n));
rsq(1) = 1-SSresid/SStotal;

subplot(2,2,2)
f2 = fit(P176_out(m:n)',PB(m:n),'poly1');
plot([-5 35],[-5 35],'k')
hold on
plot(f2,'b')
errorbar(P176_out(m:n)',PB(m:n),e_down(m:n),e_up(m:n),'ob')
hold off
xlabel('P176 (-bar)')
ylabel('Scholander Pressure Chamber (-bar)')
title('P176 vs. Scholander')
ax = gca;
ax.XLim = [-5 35];
ax.YLim = [5 25];
fitvalues(2,:) = coeffvalues(f2);
yfit = polyval(fitvalues(2,:),P176_out(m:n)');
yresid = PB(m:n)-yfit;
SSresid = sum(yresid.^2);
SStotal = (length(PB(m:n))-1)*var(PB(m:n));
rsq(2) = 1-SSresid/SStotal;

subplot(2,2,3)
f3 = fit(P179_out(m:n)',PB(m:n),'poly1');
plot([-5 35],[-5 35],'k')
hold on
plot(f3,'b')
errorbar(P179_out(m:n)',PB(m:n),e_down(m:n),e_up(m:n),'ob')
hold off
xlabel('P179 (-bar)')
ylabel('Scholander Pressure Chamber (-bar)')
title('P179 vs. Scholander')
ax = gca;
ax.XLim = [-5 35];
ax.YLim = [5 25];
fitvalues(3,:) = coeffvalues(f3);
yfit = polyval(fitvalues(3,:),P179_out(m:n)');
yresid = PB(m:n)-yfit;
SSresid = sum(yresid.^2);
SStotal = (length(PB(m:n))-1)*var(PB(m:n));
rsq(3) = 1-SSresid/SStotal;

subplot(2,2,4)
f4 = fit(P187_out(m:n)',PB(m:n),'poly1');
plot([-5 35],[-5 35],'k')
hold on
```

```
plot(f4,'b')
errorbar(P187_out(m:n)',PB(m:n),e_down(m:n),e_up(m:n),'ob')
title('P187 vs. Scholander')
hold off
xlabel('P187 (-bar)')
ylabel('Scholander Pressure Chamber (-bar)')
ax = gca;
ax.XLim = [-5 35];
ax.YLim = [5 25];
fitvalues(4,:) = coeffvalues(f4);
yfit = polyval(fitvalues(4,:),P187_out(m:n)');
yresid = PB(m:n)-yfit;
SSresid = sum(yresid.^2);
SStotal = (length(PB(m:n))-1)*var(PB(m:n));
rsq(4) = 1-SSresid/SStotal;
%% Soil Comparison
figure(3)
plot(RN(a:b),M45_S(a:b),'k')
hold on
plot(RN_MPS,S_tension,'b')
ax = gca;
ax.YLim = [-1 15];
title('\muTM vs. MPS-6')
xlabel('time(hour)')
ylabel('\Psi water potential (-bar)')
legend('M45 \muTM','MPS-6','Location','EastOutside')
%%
print('day3.pdf','-dpdf','-bestfit','-r1000')
```

VIII.E. 2D HEAT TRANFER SIMULATION PROGRAM

```
% 2D finite difference model for heat transfer simulation
% Complete embedding of sensor filled completely with urethane
% a + chip only embedding
tic
clear
close all
clc

change_to_air = 1; % 0 means the material around the chip is
polyurethane; 1 means it is air
T_ind = 0.1;
tube_length = 12e-3;     % [m]  length of the tube
tube_diameter = 10e-3;   % [m]  diameter of the sensor+tubing

% materials information
```

```
% silicon
k_si = 130; % thermal conductivity W/m-K
d_si = 2330; % density kg/m^3
C_si = 0.81*1000;% specific heat capacity J/kg-K
alpha_si = k_si/(d_si*C_si);% thermal diffusivity m^2/s

% UR5041 packaging material
k_u = 0.25;
d_u = 1180;
C_u = 1800;
alpha_u = k_u/(d_u*C_u);

% air
k_a = 0.026;
d_a = 1.1839;
C_a = 1010;
alpha_a = k_a/(d_a*C_a);

%overall heat transfer coefficient
r_1 = 1.5e-2; %[m]
r_2 = 10e-2; %[m]
h_air = 10; % W/m^2-K forced convection, low speed of flow over
a surface
U_overall = 1/(r_1/k_u*log(r_2/r_1)+r_1/r_2*1/h_air);% (W/m^2-K)

if change_to_air == 1
    k_u = k_a;
    d_u = d_a;
    C_u = C_a;
    alpha_u = alpha_a;
end


% Inputs
s_length= 5e-3;      % [m]  depth of the drilled hole in meter

s_thickness = 0.8e-3;   % [m] thickness of the sensor
alpha = tube_length/tube_diameter;  % alpha = L/W of tube L = 15
cm; W = 10 cm
beta = s_length/tube_length;      % beta = sL/L = sensor length
/ Length of tube
lamda = s_thickness/tube_diameter;
minnodes_x = 3;                      % minimum number of nodes
for the device
minnodes_y = 5;
% m = number of ndx across the sensor
```

```
% ndx is the distance between nodes in x direction ( cross-
section of the
% sensor)
% n = number of ndx on both sides of the sensor
m = minnodes_x;
n_is_an_integar = 0; % 0 means no, 1 means yes
while n_is_an_integar == 0
if abs(((1-lamda)/2)/(lamda/m)-round(((1-
lamda)/2)/(lamda/m)))<1e-15
    n_is_an_integar = 1;
    n = round(((1-lamda)/2)/(lamda/m));
else
    m = m + 1;
end
end

ndx = lamda/m;

a = minnodes_y;
b_is_an_integar = 0;
while b_is_an_integar == 0
if abs((1-beta)/(beta/a)-round((1-beta)/(beta/a)))<1e-15
    b_is_an_integar = 1;
    b = round((1-beta)/(beta/a));
else
    a = a + 1;
end
end

ndy = beta/a;

%% Create T Matrix and Indexes
X = (-(n+m/2)*ndx:ndx:(n+m/2)*ndx)*tube_diameter;
Y = (0:ndy:(a+b)*ndy)*tube_length;
T = zeros(a+b+1,m+2*n+1);
T(2:a+1,n+1:n+m+1) = 1;
g = ndx/ndy;
x = size(T,2);
y = size(T,1);
%%
if g>1
    dt = (ndy)^2/(alpha_si*5);
else if g<=1
    dt = (ndx)^2/(alpha_si*5);
    end
end
```

```
% create index matrix
row = 0;
s_row = 0;
sl_row = 0;
sr_row = 0;
sb_row = 0;
st_row = 0;
for i = 2:y-1
    for j = 2:x-1
        if T(i,j) == 0
        row = row + 1;
        u_ind(row)=i+(j-1)*size(T,1);
        end
        % top side of silicon
        if T(i,j) ==1 && T(i,j-1) == 1 && T(i,j+1) == 1 &&
T(i+1,j) == 1 && T(i-1,j) == 0
            st_row = st_row + 1;
            s_ind_t(st_row) = i + (j-1)*size(T,1);
        end
        % top left corner
        if T(i,j) ==1 && T(i,j-1) == 0 && T(i,j+1) == 1 &&
T(i+1,j) == 1 && T(i-1,j) == 0
            s_ind_tlc = i + (j-1)*size(T,1);
        end
        % top right corner
        if T(i,j) ==1 && T(i,j-1) == 1 && T(i,j+1) == 0 &&
T(i+1,j) == 1 && T(i-1,j) == 0
            s_ind_trc = i + (j-1)*size(T,1);
        end
        % internal silicon
        if T(i,j) ==1 && T(i,j-1) == 1 && T(i,j+1) == 1 &&
T(i+1,j) == 1 && T(i-1,j) == 1
            s_row = s_row + 1;
            s_ind(s_row) = i + (j-1)*size(T,1);
        end
        % left side of silicon
        if T(i,j) == 1 && T(i,j-1) == 0 && T(i,j+1) == 1 &&
T(i+1,j) == 1 && T(i-1,j) == 1
            sl_row = sl_row + 1;
            s_ind_l(sl_row) = i+(j-1)*size(T,1);
        end
        % right side of silicon
        if T(i,j) == 1 && T(i,j-1) == 1 && T(i,j+1) == 0 &&
T(i+1,j) == 1 && T(i-1,j) == 1
            sr_row = sr_row + 1;
            s_ind_r(sr_row) = i+(j-1)*size(T,1);
        end
```

```
        % bottom side of silicon
        if T(i,j) == 1 && T(i,j-1) == 1 && T(i,j+1) == 1 &&
T(i+1,j) == 0 && T(i-1,j) == 1
            sb_row = sb_row + 1;
            s_ind_b(sb_row) = i+(j-1)*size(T,1);
        end
        % bottom left corner
        if T(i,j) == 1 && T(i,j-1) == 0 && T(i,j+1) == 1 &&
T(i+1,j) == 0 && T(i-1,j) == 1
            s_ind_blc = i+(j-1)*size(T,1);
        end
        % bottom right corner
        if T(i,j) == 1 && T(i,j-1) == 1 && T(i,j+1) == 0 &&
T(i+1,j) == 0 && T(i-1,j) == 1
            s_ind_brc = i+(j-1)*size(T,1);
        end
    end
end
% bottom boundary condition of the system
bound_b = 0;
for j = 2:size(T,2)-1
    bound_b = bound_b+1;
    b_ind(bound_b) = a+b+1+(j-1)*size(T,1);
end
% top and sides boundary conditions
bound_t = 0;
for j = 2:x-1
    bound_t = bound_t+1;
    t_ind(bound_t) = 1+(j-1)*y;
end
bound_r = 0;
bound_l = 0;
for i = 2:y-1
    bound_l = bound_l+1;
    bound_r = bound_r+1;
    l_ind(bound_l) = i;
    r_ind(bound_r) = i+(x-1)*y;
end
tlc_ind = 1;
blc_ind = y;
trc_ind = 1+(x-1)*y;
brc_ind = x*y;

%% Dimensionless Conditions
% dimensionless initial and boundary conditions
T_p = 1;
T_inf = 0;
```

```
T(:,:) = T_inf;         %[C] Define Initial Conditions
T(1,:) = T_p;         %[C] Define Boundary Conditions
T(:,1) = T_p;       %[C] left top
T(:,end) = T_p;     %[C] Right top

%% RUN
t = 0;
stop_sim = 0;
ind = 1;
T_diff(ind) = 0;
g = ndx/ndy;
Fo_u = alpha_u*dt/(ndx^2);
Fo_si = alpha_si*dt/(ndx^2);
Bi = U_overall*ndx/k_u;

while stop_sim ==0
    t = t + dt;
    ind = ind+1;
     % top boundary condition
    %T(t_ind) = T(t_ind)+Fo_u*(T(t_ind+y)+T(t_ind-y)-
2*T(t_ind))+2*Fo_u*g^2*(T(t_ind+1)-T(t_ind));
    %left side boundary condition
    %T(l_ind) = T(l_ind)+Fo_u*g^2*(T(l_ind+1)+T(l_ind-1)-
2*T(l_ind))+2*Fo_u*(T(l_ind+y)-T(l_ind));
    %right side boundary condition
    %T(r_ind) = T(r_ind)+Fo_u*g^2*(T(r_ind+1)+T(r_ind-1)-
2*T(r_ind))+2*Fo_u*(T(r_ind-y)-T(r_ind));
    % top left corner
    %T(tlc_ind) = T(tlc_ind)+2*Fo_u*(T(tlc_ind+y)-
T(tlc_ind))+2*g^2*Fo_u*(T(tlc_ind+1)-T(tlc_ind));
    %bottom left corner
    %T(blc_ind) = T(blc_ind)+2*Fo_u*(T(blc_ind+y)-
T(blc_ind))+2*g^2*Fo_u*(T(blc_ind-1)-T(blc_ind));
     % top right corner
    %T(trc_ind) = T(trc_ind)+2*Fo_u*(T(trc_ind-y)-
T(trc_ind))+2*g^2*Fo_u*(T(trc_ind+1)-T(trc_ind));
    % bottom right corner
    %T(brc_ind) = T(brc_ind)+2*Fo_u*(T(brc_ind-y)-
T(brc_ind))+2*g^2*Fo_u*(T(brc_ind-1)-T(brc_ind));
    % bottom boundary condition
    T(b_ind) = Fo_u*(T(b_ind-y)-
2*T(b_ind)+T(b_ind+y))+2*g^2*Fo_u*(T(b_ind-1)-
T(b_ind))+2*g*Bi*Fo_u*(-T(b_ind))+T(b_ind);% changed T-p to
T(u_bound)
    % urethane part
```

```
    T(u_ind) = Fo_u*(T(u_ind-y)-
2*T(u_ind)+T(u_ind+y))+Fo_u*g^2*(T(u_ind-1)-
2*T(u_ind)+T(u_ind+1))+T(u_ind);
    %T(u_ind) = Fo_u*(T(u_ind)+T(u_ind-y)+g^2*T(u_ind-
1)+g^2*T(u_ind+1))-((2+2*g^2)*Fo_u-1)*T(u_ind);
    % silicon part
    T(s_ind) = Fo_si*(T(s_ind-y)-
2*T(s_ind)+T(s_ind+y))+Fo_si*g^2*(T(s_ind-1)-
2*T(s_ind)+T(s_ind+1))+T(s_ind);
    % silicon top side
    T(s_ind_t) = T(s_ind_t)+Fo_si*(T(s_ind_t-y)-
2*T(s_ind_t)+T(s_ind_t+y))+2*k_u/k_si*g^2*Fo_si*(T(s_ind_t-1)-
T(s_ind_t))+2*g^2*Fo_si*(T(s_ind_t+1)-T(s_ind_t));
    % silicon top left corner
    T(s_ind_tlc) = T(s_ind_tlc)+4*Fo_si*k_u/k_si*(T(s_ind_tlc-
y)-T(s_ind_tlc))+2*Fo_si*(T(s_ind_tlc+y)-
T(s_ind_tlc))+4*k_u/k_si*Fo_si*g^2*(T(s_ind_tlc-1)-
T(s_ind_tlc))+2*Fo_si*g^2*(T(s_ind_tlc+1)-T(s_ind_tlc));
    % silicon top right corner
    T(s_ind_trc) =
T(s_ind_trc)+4*Fo_si*k_u/k_si*(T(s_ind_trc+y)-
T(s_ind_trc))+2*Fo_si*(T(s_ind_trc-y)-
T(s_ind_trc))+4*k_u/k_si*Fo_si*g^2*(T(s_ind_trc-1)-
T(s_ind_trc))+2*Fo_si*g^2*(T(s_ind_trc+1)-T(s_ind_trc));
    % silicon left
    T(s_ind_l) = T(s_ind_l)+2*Fo_si*k_u/k_si*(T(s_ind_l-y)-
T(s_ind_l))+2*Fo_si*(T(s_ind_l+y)-
T(s_ind_l))+g^2*Fo_si*(T(s_ind_l-1)-
T(s_ind_l))+g^2*Fo_si*(T(s_ind_l+1)-T(s_ind_l));
    % silicon right
    T(s_ind_r) = T(s_ind_r)+ 2*Fo_si*(T(s_ind_r-y)-
T(s_ind_r))+g^2*Fo_si*(T(s_ind_r-1)-
2*T(s_ind_r)+T(s_ind_r+1))+2*k_u/k_si*Fo_si*(T(s_ind_r+y)-
T(s_ind_r));
    % silicon left bottom corner
    T(s_ind_blc) = T(s_ind_blc)+4*Fo_si*(T(s_ind_blc-y)-
T(s_ind_blc))+4*g^2*k_u/k_si*Fo_si*(T(s_ind_blc+1)-
T(s_ind_blc))+2*g^2*Fo_si*(T(s_ind_blc-1)-
T(s_ind_blc))+2*Fo_si*(T(s_ind_blc+y)-T(s_ind_blc));
    % silicon right bottom corner
    T(s_ind_brc) = T(s_ind_brc)+2*Fo_si*(T(s_ind_brc-y)-
T(s_ind_brc))+2*Fo_si*g^2*(T(s_ind_brc-1)-
T(s_ind_brc))+4*Fo_si*k_u/k_si*(T(s_ind_brc+y)-
T(s_ind_brc))+k_u/k_si*g^2*4*Fo_si*(T(s_ind_brc+1)-
T(s_ind_brc));
    % silicon bottom side
```

```
    T(s_ind_b) = T(s_ind_b)+Fo_si*(T(s_ind_b-y)-
2*T(s_ind_b)+T(s_ind_b+y))+2*Fo_si*g^2*(T(s_ind_b-1)-
T(s_ind_b))+2*Fo_si*g^2*(k_u/k_si)*(T(s_ind_b+1)-T(s_ind_b));

    T_diff(ind) = T(round(a+b/2),round(n+m/2));
%     if ind > 40000 && abs(T_diff(ind)-T_diff(ind-1))<=1e-8 &&
T_diff(ind)>1e-3
%         stop_sim = 1;
%     else
%         stop_sim = 0;
%     end

    if ind > 550000 && abs(T_diff(ind)-T_diff(ind-1))<=1e-20
        stop_sim = 1;
    else
        stop_sim = 0;
    end

    if mod(ind,10000) == 0
    clc
    figure(1)
    plot(t/60,T_diff(ind),'ob')
    hold on
    xlabel('time(min)')
    ylabel('Temp(Cavity)')

    figure(2)
    surf(T)
    drawnow
    fprintf('time passed:\n %8.4f min \n',t/60)
    fprintf('temperature difference between cavity and sample:\n
%8.4f fraction of (T-plant - T-outside) \n',T_diff(ind))
    end

end
%%
figure(3)
surf(X,Y,T)
fprintf('time interval: \n %8.4f s \n',dt)
fprintf('tube length: \n %8.4f mm \n',tube_length*1000)

fprintf('complete time passed:\n %8.4f min \n',t/60)
fprintf('final temperature difference between cavity and
sample:\n %8.4f fraction of (T-plant - T-outside)
\n',T_diff(end))
toc
```